Affine Frequency Division Multiplexing (AFDM) for Wireless Communications

Dissertation

submitted to

Sorbonne Université

in partial fulfillment of the requirements for the degree of
Doctor of Philosophy

Author:

Ali Bemani

Scheduled for defense on the 8th December of 2023 before a committee composed of:

Reviewers		
Prof.	**Giuseppe Caire**	TU-Berlin, Germany
Prof.	**Christos Masouros**	UCL, UK
Examiners		
Prof.	**Lina Mroueh**	ISEP, France
Prof.	**Dirk Slock (president of the jury)**	Eurecom, France
Dr.	**Arman Shojaeifard**	InterDigital, UK
Thesis Advisor		
Prof.	**Marios Kountouris**	EURECOM, France
Invited		
Dr.	**Nassar Ksairi**	Huawei R&D, France

Affine Frequency Division Multiplexing (AFDM) pour Communications sans Fil

Thèse

soumise à

Sorbonne Université

pour l'obtention du Grade de Docteur

présentée par:

Ali Bemani

Soutenance de thèse prévue le 8 Décembre 2023 devant le jury composé de:

Rapporteur

Prof.	**Giuseppe Caire**	TU-Berlin, Allemagne
Prof.	**Christos Masouros**	UCL, Royaume-Uni

Examinateur

Prof.	**Lina Mroueh**	ISEP, France
Prof.	**Dirk Slock (président du jury)**	Eurecom, France
Dr.	**Arman Shojaeifard**	InterDigital, Royaume-Uni

Directeur de Thèse

Prof.	**Marios Kountouris**	EURECOM, France

Invité

Dr.	**Nassar Ksairi**	Huawei R&D, France

Abstract

In the realm of next-generation wireless systems (beyond 5G/6G), the vision is clear: to support a broad range of services and applications. This includes ensuring reliable communications in environments marked by high mobility, such as high-speed railway systems and various vehicular communications. Despite the deployment of various multicarrier techniques like orthogonal frequency division multiplexing (OFDM) and single-carrier frequency division multiple access (SC-FDMA) in standardized communication systems, the challenge persists. These techniques, while effective in time-invariant frequency selective channels, face performance degradation in high mobility scenarios due to the destruction of orthogonality among subcarriers caused by significant Doppler frequency shifts. Addressing this, the search for new, robust modulation techniques is paramount. It stands as a key area of investigation aiming to resolve the reliable communications issue for next-generation wireless networks within doubly-selective wireless channels. In this thesis, a novel solution, affine frequency division multiplexing (AFDM), is proposed. This new chirp-based multicarrier waveform is based on the discrete affine Fourier transform (DAFT), a variant of the discrete Fourier transform characterized with two parameters that can be adapted to better cope with doubly dispersive channels.

This thesis provides a comprehensive investigation into the principles of AFDM within high mobility communications. It provides insight into the explicit input-output relation in the DAFT domain, unveiling the consequential impact of AFDM parameters. The manuscript details the precise setting of DAFT parameters, ensuring a full delay-

Doppler representation of the channel. Through analytical demonstrations, it asserts that AFDM optimally achieves the diversity order in doubly dispersive channels due to its full delay-Doppler representation.

The thesis also proposes two low-complexity detection algorithms for AFDM, taking advantage of its inherent channel sparsity. The first is a low complexity MMSE detector based on LDL factorization. The second is a low complexity iterative decision feedback equalizer (DFE) based on weighted maximal ratio combining (MRC) of the channel impaired input symbols received from different paths. Additionally, the thesis presents an embedded channel estimation strategy for AFDM systems, leveraging AFDM's ability to achieve full delay-Doppler representation of the channel. In this approach, an AFDM frame contains a pilot symbol and data symbols, with zero-padded symbols employed as guard intervals to prevent interference. A practical channel estimation algorithm based on an approximate maximum likelihood (ML) approach and compatible with this pilot scheme is also provided.

The thesis concludes by delving into the expanded applications of AFDM, specifically in integrated sensing and communication (ISAC) and extremely high frequency (EHF) band communications. It is demonstrated that to identify all delay and Doppler components linked with the propagation medium, one can use either the full AFDM signal or only its pilot part consisting of one DAFT domain symbol and its guard interval. Furthermore, the chirp nature of AFDM allows for unique and simple self-interference cancellation with a single pilot, eliminating the need for costly full-duplex methods. The thesis also highlights AFDM's efficient performance in high-frequency bands (with or without mobility), where the maximal spreading of its signal in time and frequency ensures a coverage gain. Unlike other waveforms, AFDM not only provides maximal time-frequency spreading but also ensures robust and efficient detection, characterized by one-tap equalization and resilience to carrier frequency offset (CFO) and phase noise.

Abrégé

Un défi pricipal pour les systèmes de communication sans fil de nouvelle génération (au-delà de la 5G/6G) est de prendre en charge une large gamme de services et d'applications. Cela inclut d'assurer des communications fiables dans des environnements marqués par une haute mobilité, tels que les systèmes ferroviaires à grande vitesse et diverses communications véhiculaires. Malgré le déploiement de diverses techniques de type multiporteuses telles que le *orthogonal frequency division multiplexing* (OFDM) et le *single-carrier frequency division multiple access* (SC-FDMA) dans les systèmes de communication standardisés, ce défi persiste. En effet, ces techniques, bien qu'efficaces pour les communications sur des canaux sans-fil sélectifs seulement en fréquence et invariants dans le temps, font face à une dégradation des performances quand utilisées avec des canaux doublement selectifs (en fréquences et dans le temps) en raison de la destruction de l'orthogonalité entre les sous-porteuses causée par une intensification significative de l'effet Doppler. Face à cela, la recherche de nouvelles formes d'onde robustes, lorsque utilisées sur des canaux doublement selectifs, est primordiale. De telles formes d'onde permettraient donc d'assurer des communications fiables pour les réseaux sans fil de nouvelle génération dans les scénarios de haute mobilité. Dans cette thèse, une nouvelle solution, le *affine frequency division multiplexing* (AFDM), est proposée. Cette nouvelle forme d'onde de type multichirps est basée sur la transformée de Fourier affine discrète (DAFT), une variante de la transformée de Fourier discrète caractérisée par deux paramètres pouvant être adaptés pour mieux faire face aux canaux doublement

dispersifs.

Cette thèse offre une enquête complète sur les principes de l'AFDM au sein des communications à haute mobilité. Elle fournit un aperçu de la relation explicite entrée-sortie dans le domaine DAFT, révélant l'impact conséquent des paramètres de l'AFDM. Le manuscrit détaille le réglage précis des paramètres DAFT qui permette d'assurer une représentation complète délai-Doppler du canal de propagation sans fil. À travers des démonstrations analytiques, il est affirmé que l'AFDM atteint de manière optimale l'ordre de diversité des canaux doublement dispersifs en raison de la représentation complète délai-Doppler du canal qu'il permet d'obtenir.

La thèse propose également deux algorithmes de détection à faible complexité pour l'AFDM, tirant parti de la parcimonie inhérente du canal. Le premier est un détecteur de type *minimum mean squared error* (MMSE) à faible complexité basé sur la factorisation LDL. Le deuxième est un égaliseur de type *decision feedback equalizer* (DFE) à faible complexité basé sur la combinaison cohérente, grace à la méthode *maximum ratio combining* (MRC), de différentes copies des symboles d'entrée du canal ayant été altérés par différents trajets de ce dernier. De plus, la thèse présente une technique de type *embedded* d'estimation de canal pour les systèmes AFDM, exploitant la capacité de l'AFDM à obtenir une représentation complète délai-Doppler du canal. Dans cette approche, un seul symbole pilote est inséré dans le domain DAFT du symbole AFDM, et les interférences que ce pilote pourrait générer pour les symboles de donnée sont évitées par des intervalles de garde. Un algorithme pratique d'estimation de canal, compatible avec ce schéma de transmission de pilote et basé sur une approche de type *approximate maximum likelihood (ML)*, est aussi proposé.

La thèse est conclue en se penchant sur de possibles applications de l'AFDM au delà de celles conçues pour les environnements marqués par une haute mobilité, spécifiquement les applications de type *integrated sensing and communication* (ISAC) et les communications dans les bandes de hautes fréquences. Il est démontré que pour identifier

tous les composants de délai et de Doppler liés au milieu de propagation, on peut utiliser soit le signal AFDM complet, soit seulement sa partie pilote constituée d'un symbole de domaine DAFT et de son intervalle de garde. De plus, la nature chirp de l'AFDM permet une annulation simple de l'auto-interférence, éliminant ainsi le besoin de méthodes coûteuses normalement nécessaires dans les systèmes *full duplex*. La thèse met également en évidence les bonnes performances de l'AFDM pour les communications sans fil dans les bandes de hautes fréquences sans ou avec mobilité, grace à la répartition maximale du signal AFDM en temps et en fréquences, assurant un gain de couverture. Contrairement à d'autres formes d'onde, l'AFDM ne fournit pas seulement une répartition maximale temps-fréquences mais assure également une détection robuste et efficace et une résilience au décalage de fréquence de porteuse et au bruit de phase.

Acknowledgements

Completing this PhD has been a transformative journey, one that could not have been accomplished without the support, guidance, and encouragement of many. First and foremost, I must express my deepest gratitude to my supervisor, Marios Kountouris, whose expertise, understanding, and patience have significantly enhanced my graduate experience. I am also deeply thankful to Nassar Ksairi for his co-advising during my thesis, from whom I have benefited immensely through his mentorship. Additionally, my thanks extend to Giuseppe Caire and Christos Masouros for their careful review of this thesis and the constructive feedback provided.

I wish to thank my fellow PhD students and colleagues at Eurecom for the incredible moments we've shared together over the last few years. Your camaraderie and support have not only made this journey more enjoyable but also truly memorable.

A special debt of gratitude is owed to my family, particularly my parents, for their endless love, support, and sacrifices. Their unwavering belief in me has been a pilar of hope and strength throughout this journey.

Lastly, but most importantly, I wish to extend my profound gratitude to my wife, Fateme. Your love, patience, and steadfast support have been the foundation of my resilience and success. Throughout this journey, your belief in my potential and your selfless love have been my greatest sources of strength. Thank you for being more than a partner; thank you for being my confidante, my anchor in times of uncertainty, and a reason for celebration. This achievement is as much yours as it is mine.

Contents

List of Figures

List of Tables

Acronyms and Abbreviations

The acronyms and abbreviations used throughout the manuscript are specified in the following. They are presented here in their singular form, and their plural forms are constructed by adding and s, e.g. BS (base stations) and BSs (Base stations). The meaning of an acronym is also indicated the first time that it is used.

2D	two-dimensional
ADC	analog-to-digital converter
AF	ambiguity function
AFDM	affine frequency division multiplexing
AFT	affine Fourier transform
AR	auto-regressive
BER	bit error rate
BS	base station
CA	complex additions
CD	complex divisions
CFO	carrier frequency offsets
CM	complex multiplications
CP	cyclic prefix
CPE	common phase error
CPP	chirp-periodic prefix
CSS	chirp spread spectrum
DAFT	discrete affine Fourier transform
DC	direct current
DFE	decision feedback equalizer
DFT-s-OFDM	discrete Fourier transform spread OFDM
DoF	degree-of-freedom

FrFT	fractional Fourier transform
FT	Fourier transform
GFDM	Generalized frequency division multiplexing
ICI	inter-carrier interference
iid	independently and identically distributed
ISAC	integrated sensing and communications
ISI	inter-symbol interference
LCT	Linear Canonical Transform
LEO	low-earth-orbit
LTI	linear time-invariant
LTV	linear time-varying
ML	maximum likelihood
mmWave	millimeter wave
MRC	maximal ratio combining
OCDM	orthogonal chirp division multiplexing
OFDM	orthogonal frequency division multiplexing
OLA	overlap-add
OOBE	out-of-band emission
OTFS	orthogonal time frequency space
PAPR	peak to average power ratio
PEP	pairwise error probability
PN	phase noise
RMS	root mean square
RMSE	Root mean square error
SAFT	special affine Fourier transform
SFFT	symplectic finite Fourier transform
SI	self-interference
SIC	self-interference cancellation
SINR	signal-to-interference-plus-noise ratio
SNR	signal-to-noise ratio
TDMA	time-division multiple access
TF	time-frequency
UAV	unmanned aerial vehicle

WDF	Wigner distribution function

Notations

The next list describes an overview on the notation used throughout this manuscript. We use boldface uppercase letters ($\mathbf{A}$) for matrices, boldface lowercase letters for vectors ($\mathbf{a}$), and regular letters for scalars (a or A). Sets are represented by calligraphic uppercase letters ($\mathcal{A}$).

$\lvert a \rvert$	Absolute value of the variable a
$\lVert \mathbf{a} \rVert$	Euclidian norm of the vector $\mathbf{a}$
$\lvert \mathcal{A} \rvert$	Cardinality of the set $\mathcal{A}$
$\mathbf{A}^{\mathrm{T}}$	Transpose of the matrix $\mathbf{A}$
$\mathbf{A}^{-1}$	Inverse of the matrix $\mathbf{A}$
$\mathbf{A}^{\dagger}$	Adjugate of the matrix $\mathbf{A}$
$\mathrm{tr}(\mathbf{A})$	Trace of the matrix $\mathbf{A}$
$\det(\mathbf{A})$	Determinant of the matrix $\mathbf{A}$
$\mathrm{E}[.]$	Expectation
$\Pr(x)$	The probability of an event x
$\lfloor . \rfloor$	Floor function
$\triangleq$	Used for definition
$\mathcal{N}(0, \sigma^2)$	Zero-mean Gaussian distribution with variance σ^2
$\exp(.)$	Exponential function
$\log_2(a)$	Logarithm base 2 of the positive number a
$\log_{10}(a)$	Logarithm base 10 of the positive number a
$Cov\{\mathbf{a}\}$	Covariance matrix of the random vector $\mathbf{a}$

Chapter 1

Introduction

In the rapidly advancing world of wireless communication, the spotlight is increasingly on high-mobility scenarios, especially with the next generation wireless systems and standards (beyond 5G/6G). These systems are being designed to handle real-world challenges tied to high-mobility contexts, including scenarios like V2X communications, unmanned aerial vehicles (UAVs), high-speed rail systems and low-earth-orbit (LEO) satellites [1, 2]. Currently, orthogonal frequency division multiplexing (OFDM) is the star player in our wireless communication toolkit. It is the backbone of both our 4G and 5G standards, and for a good reason. In typical environments, where the frequency channels do not change quickly, OFDM shines. However, when it comes to the dynamic scenarios mentioned above, OFDM runs into problems. The reason? The Doppler spread, which happens when the sender and receiver are moving relative to each other. In such cases, we deal with channels that change with time, often called ”doubly dispersive” or ”doubly selective.” Here, OFDM's key strength – keeping signals separate and clear from each other – breaks down, leading to signal interference known as inter-carrier interference (ICI). This interference can significantly reduce system performance[3].

Moreover, as the demand for faster Internet and more data keeps growing, there is a push to move to even higher frequency bands, notably the millimeter wave (mmWave)

bands. These bands offer lots of space for data transmission, but using them in high-mobility situations accentuates the Doppler spread challenge. So, while OFDM has served us well in the past and continues to do so in many situations, its limitations in upcoming high-mobility, high-frequency scenarios are evident. There is a clear and urgent need to develop new communication methods that can tackle the unique challenges expected in B5G settings and beyond.

To address the conundrums posed by LTV channels, one prevalent method has been to shorten the duration of the OFDM symbol. By doing so, the aim is to render channel variations during this interval nearly insignificant [4]. Nevertheless, this comes at a cost: the inclusion of a cyclic prefix (CP) reduces the spectral efficiency, making it less than ideal. From a broader perspective, an optimal approach to navigate through various channels is by modulating the information symbols with a set of orthogonal eigenfunctions intrinsic to the channel. Concurrently, at the receiving end, the received signal should be projected over an identical set of eigenfunctions. This method has demonstrated optimal results for linear time-invariant (LTI) channels, particularly because complex exponentials act as their eigenfunctions and can be harnessed using the Fourier transform. Yet, when it comes to general linear time-varying (LTV) channels, establishing an orthonormal basis is not straightforward.

Since this optimal approach presents significant challenges both in terms of conceptual and computational complexity, using chirps, i.e., complex exponentials with linearly varying instantaneous frequencies, appears to be a promising alternative. The use of chirps for communication and sensing purposes has a long history. S. Darlington in 1947 proposed the chirp technique for pulsed radar systems with long-range performance and high-range resolution [5]. The term “chirp” was apparently first employed by B. M Oliver in an internal Bell Laboratories Memorandum “Not with a bang, but a Chirp”. In [6], an experimental communication system employing chirp modulation in the high frequency band for air-ground communication is presented. Since chirped waveforms are of spread-

spectrum, they can also provide security and robustness in several scenarios, including military, underwater and aerospace communications [7, 8, 9]. Chirps are specified in the IEEE 802.15.4a standard as chirp spread spectrum (CSS) to meet the requirement of FCC on the radiation power spectral mask for the unlicensed UWB systems[10].

As mentioned earlier, using a frequency-varying basis for a multicarrier scheme for transmission over time-varying channels is first introduced in [11]. In this work, an orthonormal basis formed by chirps are generated via fractional Fourier transform (FrFT) and the scheme is presented in a continuous-time framework. However, the approximation used for discretizing the continuous-time FrFT leads to imperfect orthogonality among chirp subcarriers and hence to performance degradation. A multicarrier technique based on affine Fourier transform (AFT), a generalization of the Fourier transform (FT) and FrFT, is proposed in [12]. The resulting multicarrier waveform is referred to as DAFT-OFDM in the sequel. It is equivalent to OFDM with reduced ICI on doubly dispersive channels which leads to low diversity order. Moreover, the delays and the Doppler shifts of channel paths are needed at the transmitter to tune the DAFT-OFDM parameters. In [13], the author presents a general interference analysis of the DAFT-OFDM system and the optimal parameters are obtained in the closed-form followed by the analysis of the effects of synchronization errors and the optimal symbol period. Orthogonal chirp division multiplexing (OCDM) [14], which is another scheme based on the discrete Fresnel transform - a special case of DAFT - and proposed for the time-dispersive channels. [15] shows OCDM performs better than uncoded OFDM in LTI and LTV channels. However, it cannot achieve the full diversity of these channels. [15] states in LTI channels, OCDM collects unit diversity for very large SNR. Moreover, OCDM cannot achieve full diversity in general LTV channels, since its diversity order depends on the delay-Doppler profile of the channel.

Apart from the chirp-based schemes, some other waveforms are presented as beyond OFDM waveforms, as OFDM suffers from not only sensitivity to carrier frequency offsets

(CFO), but also high peak to average power ratio (PAPR) and out-of-band emission (OOBE). In order to reduce PAPR, discrete Fourier transform spread OFDM (DFT-s-OFDM) is proposed [16]. The DFT-s-OFDM spread symbol energy equally over all sub-carriers to reduce PAPR by precoding data symbols using a DFT. To reduce the OOBE, Generalized Frequency Division Multiplexing (GFDM) [17, 18] is proposed which is a multi-carrier modulation scheme based on a circular pulse shaping filter. However, DFT-s-OFDM and GFDM are sensitive to CFO due to Doppler spread. To deal with the Doppler spread, recently, orthogonal time frequency space (OTFS) modulation [19, 20] is proposed for high mobility communications. OTFS is a two-dimensional (2D) modulation technique that spreads the information symbols over the delay-Doppler domain. [21] compares the performance of different schemes and shows that OTFS outperforms all other waveforms in both frequency selective and doubly selective channels. Therefore, in this paper, we focus on OTFS and compare it with our waveform in more detail. The literature in the area of OTFS, shows that it achieves the full so-called *effective* diversity order [22], i.e., the diversity order in the finite signal-to-noise ratio (SNR) regime. However, [23] shows that the OTFS diversity order without channel coding is one and with a phase rotation scheme using transcendental numbers can be made to achieve full diversity. The idea of embedding pilots along with the data symbols in the DD plane has been proposed in [24]. Although it does not need a separate transmission for the pilot symbols, it suffers from excessive pilot overhead due to the 2D structure as each pilot symbol should be separated from the data symbols.

1.1 Contribution and Outline of the Thesis

The thesis begins with a thorough overview in Chapter 2, offering essential background knowledge crucial for grasping the contributions of this manuscript. Initially, it delves into a review of wireless channels before shifting its attention to the AFT and its discrete variant, DAFT, which serves as the foundation of affine frequency division multiplexing

(AFDM). Following this, we will underline the main contributions of this research and provide a structured outline of the subsequent chapters, guiding the reader through the progression of this study.

- **Chapter 3: AFDM.** This chapter presents the principles of AFDM by leveraging the fundamentals of the discrete affine Fourier transform (DAFT). Our exposition provides a detailed understanding of the transmitter and receiver mechanisms. Additionally, we conduct an in-depth analysis of the input-output relationship. A special emphasis is placed on the pivotal role of parameter setting in AFDM, highlighting its crucial influence on the communication system's performance.

  This chapter is based on the publications as identified in Table 1.1

- **Chapter 4: AFDM for full diversity on LTV channels.** In this chapter, we examine AFDM to understand how it achieves the full diversity of the LTV channels. In our investigation, we identify the optimal values for AFDM parameters, ensuring that the DAFT domain impulse response captures the entire delay-Doppler profile of the channel. This makes AFDM to attain the optimal diversity order in LTV channels. Furthermore, we delineate both the necessary and sufficient conditions under which AFDM can achieve full diversity. This assertion is reinforced by our analytical proof. In this proof, through the analysis of the error performance of AFDM systems based on the study of pairwise error probability (PEP), we demonstrate that AFDM achieves the full diversity order in LTV channels under these conditions.

  This chapter is based on the publications as identified in Table 1.1

- **Chapter 5: Detection and Channel Estimation.** In this chapter,two AFDM signal detection approaches and an embedded channel estimation strategy are proposed. We introduce two low-complexity detection algorithms for AFDM, both of which capitalize on its inherent channel sparsity. By integrating null symbols, effectively zero-padding the AFDM frame in the DAFT domain, we can approximate the

channel matrix as a band matrix. With this approximation in place, our first contribution is a low-complexity MMSE detector built on LDL factorization. Its complexity is linear in the number of subcarriers and quadratic relative to the band matrix's bandwidth, which is influenced by both the maximum delay and maximum Doppler shift. Our second detection algorithm is an efficient iterative decision feedback equalizer (DFE) based on the weighted maximal ratio combining (MRC) of channel-impaired input symbols received across different paths. Remarkably, the complexity of this second algorithm remains linear with respect to both the number of subcarriers and the number of paths. Our analysis reveals that both detectors offer comparable performance metrics. However, when the channel is sparse in the delay domain, the MRC-based DFE detector emerges as the less complex option.

Moreover, we present an embedded channel estimation strategy for AFDM systems, leveraging AFDM's ability to achieve full delay-Doppler representation of the channel. In our approach, a single AFDM frame contains a pilot symbol and data symbols, with zero-padded symbols employed as guard intervals to prevent interference. Our contribution also encompasses the development of efficient approximated maximum likelihood (ML) algorithms, tailored for estimating channel information like complex gains, delays, and Doppler shifts. Our evaluations reveal that AFDM's performance, when equipped with our proposed channel estimation methods, only experiences a minimal decline compared to its performance under perfectly known channel information.

This chapter is based on the publications as identified in Table 1.1

- **Chapter 6: Further Applications.** This chapter delves into the further applications of AFDM, spotlighting its promising role in two groundbreaking areas: Integrated Sensing and Communication (ISAC) and communication in extremely high frequency bands (EHF).

  First, we illustrate that AFDM can be utilized for ISAC using either the whole

frame or one pilot symbol, a concept inspired by our earlier channel estimation approach in which as few as one DAFT domain symbol used as a pilot can yield, when appended with a sufficient number of zero guard samples, the possibility to identify all the delay and Doppler components associated with the propagation medium. This is evidently relevant for sensing and radar applications since the delay-Doppler representation of the wireless channel associated with the round trip propagation from the wireless transmitter to the targets in its vicinity and back to the transmitter translates into range-velocity information about those targets. We further establish that by sensing with one DAFT domain pilot rather than the whole signal, a low-complexity self-interference cancellation (SIC) can be implemented even when this pilot multiplexed with data and possibly other pilots. we show that SIC in AFDM-based ISAC can be alleviated with simple analog dechirping and filtering which is an advantage over OFDM or OTFS-based ISAC solutions that need costly full-duplex SIC methods.

We also showcase the performance of AFDM in communications at high-frequency bands without mobility. In such bands, AFDM is maximally spread in time and frequency, thus providing a coverage gain. While maximal time-frequency spreading can be offered by other waveforms (e.g., OTFS, CSS), AFDM is distinguished by the fact that the benefits of maximal spreading are achieved while detection is (i) performed using one-tap equalization and (ii) robust to CFO and phase noise (PN).

This chapter is based on the publications [25, 26, 27, 28, 29] as identified in Table 1.1

Table 1.1: Publications and their contributions to the chapters.

Type	Reference	Ch. 3	Ch. 4	Ch. 5	Ch. 6
C	A. Bemani, N. Ksairi, and M. Kountouris, "AFDM: A Full Diversity Next Generation Waveform for High Mobility Communications," in *2021 IEEE International Conference on Communications Workshops (ICC Workshops)*, Montreal, QC, Canada, 2021, pp. 1-6	✓	✓		
C	A. Bemani, G. Cuozzo, N. Ksairi, and M. Kountouris, "Affine Frequency Division Multiplexing for Next-Generation Wireless Networks," in *2021 17th International Symposium on Wireless Communication Systems (ISWCS)*, Berlin, Germany, 2021, pp. 1-6			✓	✓
C	A. Bemani, N. Ksairi, and M. Kountouris, "Low Complexity Equalization for AFDM In Doubly Dispersive Channels," in *ICASSP 2022 - 2022 IEEE International Conference on Acoustics, Speech and Signal Processing (ICASSP)*, Singapore, Singapore, 2022, pp. 5273-5277			✓	
J	A. Bemani, N. Ksairi, and M. Kountouris, "Affine Frequency Division Multiplexing for Next Generation Wireless Communications," in *IEEE Transactions on Wireless Communications (2023)*.	✓	✓	✓	
J	A. Bemani, N. Ksairi, and M. Kountouris, "Integrated Sensing and Communications with Affine Frequency Division Multiplexing," in *IEEE Wireless Communications Letters (2024)*				✓

C = Conference, J = Journal

Chapter 2

Background

In this chapter, we provide a comprehensive overview of the background knowledge essential for understanding the key contributions of this manuscript. The first section delves into the properties of wireless channels, such as path loss and fading effects. Comprehending the nature of the wireless channel is critical for the design and evaluation of wireless communication systems due to its direct impact on system performance.

The second section concentrates on the AFT and its discrete variant, forming the foundation of AFDM. We elucidate the fundamentals of AFT, including its definition and applications. Furthermore, we introduce the discrete counterpart of AFT, known as the DAFT, utilized in AFDM. We discuss how DAFT is employed to construct a multi-carrier signal with inter-carrier orthogonality. By the conclusion of this chapter, readers will possess a comprehensive understanding of the foundational concepts and techniques pertaining to wireless channels and the affine Fourier transform, serving as a critical basis for the subsequent chapters.

2.1 Wireless Channels Background

One of the paramount factors influencing the performance of wireless communication systems is the propagation medium or the wireless channel. Comprehending the properties

of a wireless channel is vital for the development of robust and efficient wireless communication systems. In this section, we offer a background on wireless channels, emphasizing their characteristics and types. Starting with the fundamentals of electromagnetic wave propagation, we provide a detailed overview of various wireless channel types, including flat and frequency selective fading, fast and slow fading, and doubly selective channels. We further underline the influence of channel characteristics on the performance of wireless communication systems and the different techniques used to mitigate the channel impairments. Drawing on concepts and analyses presented in authoritative references on wireless channels, such as [30, 31], this section imparts a comprehensive understanding of wireless channel properties.

2.1.1 Path Loss and Fading

The quality of wireless communications is critically influenced by the received signal power. Nevertheless, various impairments such as path loss, large-scale fading, and small-scale fading can cause fluctuations in this power.

Path loss, the result of signal attenuation due to distance-dependent power decay, is typically modeled by an exponential distribution with a path loss exponent, denoted by α. The path loss in decibels is given by $10\log_{10}(d)$, where d represents the distance traversed by the electromagnetic wave.

In addition to path loss, wireless signals experience fading, which corresponds to fluctuations in received signal power due to the constructive or destructive interference of signal components that reach the receiver via multiple paths. Fading can be divided into two primary categories: large-scale fading and small-scale fading.

Large-scale fading, also referred to as shadowing, encompasses signal attenuation induced by obstructions and environmental factors such as buildings, mountains, and vegetation. Characterized by a slow variation of received power over extensive distances, large-scale fading is typically modeled using a log-normal distribution. This variation

usually depends on the distance between the transmitter and receiver, as well as the obstructions and reflections encountered along the propagation path[32].

Contrarily, small-scale fading represents the rapid fluctuation of received signal power over a short distance or area. Primarily caused by the interference of signal components arriving through different paths, small-scale fading is generally modeled using a stochastic fading model that outlines the statistical distribution of the fluctuations in received signal power, such as the Rayleigh or Rician fading models. Different transmitted signals experience varying types of fading, depending on the relation between signal parameters, such as bandwidth and symbol period, and channel parameters, including coherence time, Doppler spread, coherence bandwidth, and delay spread. Time dispersion and frequency dispersion, resulting from independent propagation mechanisms, lead to distinct types of fading.

The impacts of path loss and fading on the wireless channel can significantly influence the performance of wireless communication systems, affecting aspects such as data rate, error rate, and coverage. Consequently, the precise modeling and characterization of path loss and fading channels are pivotal for the design and optimization of wireless communication systems.

2.1.2 Flat Fading and Frequency-Selective Fading

Flat fading and frequency-selective fading are types of small-scale fading caused by time dispersion resulting from multipath propagation. In flat fading, the signal's bandwidth is smaller than the channel's coherence bandwidth, causing all frequency components of the signal to fade simultaneously. Consequently, the only distortion in the received signal is a time-varying gain, leading to error bursts. Techniques like interleaving and burst error-correcting codes are employed to combat these errors. On the contrary, in frequency-selective fading, the signal's bandwidth exceeds the channel's coherence bandwidth, causing differential effects on frequencies separated by an amount larger

than the coherence bandwidth. Consequently, some frequency components fade while others do not, resulting in inter-symbol interference (ISI), which must be corrected for acceptable system performance. If the symbol period is considerably greater than the root-mean-square delay spread, the channel is considered to experience flat fading, while it is deemed to experience frequency-selective fading if the symbol period is comparable to or less than the root-mean-square delay spread.

2.1.3 Fast Fading and Slow Fading

Fast fading and slow fading are two types of small-scale fading that can occur in both flat and frequency-selective fading channels due to frequency dispersion caused by Doppler spreading. Fast fading arises when the channel impulse response changes rapidly within the symbol duration, i.e., the coherence time of the channel is smaller than the symbol period, causing signal distortion that increases with increasing Doppler spread relative to the signal bandwidth. In contrast, slow fading occurs when the channel impulse response changes at a rate much slower than the signal, indicating a larger coherence time. The effects of fading can be mitigated using techniques such as interleaving and error-correcting codes in flat fading channels, and equalizers in frequency-selective fading channels. However, the complexity of these techniques escalates with the mobility and frequency-dependency of the channel.

2.1.4 Doubly Selective Channels

Doubly selective channels, also known as doubly dispersive channels or LTV channels, are influenced by both the multi-path and the Doppler effects, which induce time and frequency dispersions and selectivities in the received signal. These channels are common in outdoor environments, where non-negligible delay and Doppler shifts from strong multi-path components are present. Despite the challenges doubly selective channels present for channel estimation and equalization, recent advances in wireless communication have

demonstrated that these time and frequency selectivities can be exploited to improve communication performance. Doubly selective channels provide new degrees-of-freedom (DoFs) that can be fully exploited through careful design of the transmitted signal, harnessing the full time-frequency (TF) diversity.

2.1.5 Mathematical Representation of the Channel

In this section, we delve into the mathematical representations of wireless channels in the complex baseband domain for general LTV channels in a deterministic scenario. We assume a situation where the physical characteristics of the channel, such as the number of scatterers, the relative velocity of the scatterers, the distances between the transmitter and receiver relative to each scatterer, and the reflectivities associated with each scatterer, remain approximately unchanged during signal transmission. This assumption can be thought of as a snapshot of the real channel, with the duration of its validity depending on the specifics of the actual scenario.The relevance of this assumption is discussed further on in this section.

We focus on the equivalent complex baseband representation of the wireless channel, which is extensively used in the design and analysis of wireless communication systems. For a general LTV channel with P resolvable paths, we use h_p, f_p, and τ_p to denote the complex gain coefficient, time delay, and Doppler frequency associated with the p-th path, respectively. Accurate estimation of these parameters is crucial for efficient communication system design. Hence, the channel impulse response at time t and delay τ can be expressed as:

$$h(t,\tau) = \sum_{p=1}^{P} h_p e^{-\imath 2\pi f_p t} \delta(t-\tau_p), \tag{2.1}$$

The mathematical model above is a general model for LTV channels with resolvable paths in a deterministic scenario. It can be utilized to simulate the wireless channel and to design communication systems that operate over the wireless channel.

Suppose $s(t)$ is the complex baseband signal transmitted by the transmitter, and $r(t)$ is the received signal after passing through the wireless channel. Under the assumption of a noiseless environment, the input-output relationship between $s(t)$ and $r(t)$ is given by:

$$s(t) = \int_{-\infty}^{+\infty} s(t-\tau)h(t,\tau)d\tau = \sum_{i=p}^{P} h_p s(t-\tau_p)e^{-\imath 2\pi f_p t}. \tag{2.2}$$

2.2 Affine Fourier Transform

AFT also known as the Linear Canonical Transform (LCT) is a powerful mathematical tool that can be used to analyze signals in the time-frequency domain. It was first introduced in the 1970s by Collins and Moshinsky and Quesne [33, 34]. The AFT has since found numerous applications in signal processing, optics, acoustics, and other fields. In addition to being known as the AFT, it has also been given various other names by different researchers. These include the special affine Fourier transform (SAFT)[35], the ABCD transform [36], the generalized Fresnel transform [37], the Collins formula[33], the quadratic phase system[38, 39, 40, 41], the generalized Huygens integral[42], and the extended fractional Fourier transform[43].

The AFT is a generalization of the FT and the FRFT. Before introducing the AFT, we first review the FT and FRFT. Typically, time-frequency representations involve a plane with two orthogonal axes representing time and frequency. For a signal $x(t)$ represented along the time axis and its ordinary Fourier transform $X(f)$ represented along the frequency axis, the Fourier transform operator (F) is a counterclockwise rotation of the axis by $\pi/2$. On the other hand, the FRFT is a linear operator that rotates the signal by an angle α which is not a multiple of $\pi/2$. It represents the signal along the axis u, making an angle α with the time axis. The FRFT is known to outperform the FT in several signal processing and optical system analysis applications due to its greater flexibility [44, 45, 46]. Nonetheless, the FRFT suffers from a drawback in that it has

only one parameter, making it less versatile. To address this limitation, the FRFT can be extended to AFT, which incorporates a total of four parameters. In this section, we define the AFT, explain its physical meaning, and discuss how discrete version of the AFT can be achieved.

2.2.1 Definition of Affine Fourier Transform

Affine Fourier Transform is a four-parameter (a, b, c, d) class of linear integral transform defined as

$$S_{a,b,c,d}(u) = \begin{cases} \int_{-\infty}^{+\infty} s(t) K_{a,b,c,d}(t,u) \mathrm{d}t, & b \neq 0 \\ s(du) \frac{e^{-\imath \frac{cd}{2} u^2}}{\sqrt{a}}, & b = 0 \end{cases} \tag{2.3}$$

where (a, b, c, d) forms $\mathrm{M} = \begin{bmatrix} a & b \\ c & d \end{bmatrix}$ with unit determinant, i.e, $ad - bc = 1$ and transform kernel given by

$$K_{a,b,c,d}(t,u) = \frac{1}{\sqrt{2\pi|b|}} \mathrm{e}^{-\imath(\frac{a}{2b}u^2 + \frac{1}{b}ut + \frac{d}{2b}t^2)}. \tag{2.4}$$

The inverse transform can be expressed as an AFT having the parameters $\mathrm{M}^{-1} = \begin{bmatrix} d & -b \\ -c & a \end{bmatrix}$

$$s(t) = \int_{-\infty}^{+\infty} S_{a,b,c,d}(u) K^*_{a,b,c,d}(t,u) \mathrm{d}u. \tag{2.5}$$

The AFT generalizes several known mathematical transforms, such as Fourier transform (0,1/2π,-2π,0), Laplace transform (0,j(1/2π),j2π,0), θ-order fractional Fourier transform (cosθ, (1/2π)sinθ,-2π sin θ,cos θ), Fresnel transform and the scaling operations. The extra degree of freedom of AFT provides flexibility and has been employed in many applications, including filter design, time-frequency analysis, phase retrievals, and multiplexing in communication.

The effect of AFT can be interpreted by the Wigner distribution function (WDF)[47],

which is a is a quadratic time-frequency distribution[48, 49]. If $W_s(u,v)$ and $W_{S_{a,b,c,d}}(u,v)$ are the WDF of $s(t)$ and $S_{a,b,c,d}(u)$, respectively, then

$$W_{S_{a,b,c,d}}(u,v) = W_s(du - bv, -cu + av) \tag{2.6}$$

that is,

$$W_{S_{a,b,c,d}}(au + bv, cu + dv) = W_s(u,v), \tag{2.7}$$

where

$$W_s(u,v) \stackrel{\text{def.}}{=} \frac{1}{2\pi}\int_{-\infty}^{+\infty} s(u+\tau/2)s^*(u-\tau/2)e^{-\imath v\tau}\mathrm{d}\tau. \tag{2.8}$$

In other words, the AFT can be understood as a transformation that rotates the time-frequency distribution of a function, without changing its total area. Thus, applying the AFT to a function results in a twisted Wigner distribution function, while maintaining its original area. It also has a close relation with the ambiguity function (AF)[47]. If $AF_s(\eta,\tau)$ and $AF_{S_{a,b,c,d}}(\eta,\tau)$ are the AF of $s(t)$ and $S_{a,b,c,d}(u)$ respectively, then

$$AF_{S_{a,b,c,d}}(\eta,\tau) = AF_s(a\eta - c\tau, -b\eta + d\tau) \tag{2.9}$$

where

$$AF_s(\eta,\tau) \stackrel{\text{def.}}{=} \frac{1}{2\pi}\int_{-\infty}^{+\infty} s(t+\tau/2)s^*(t-\tau/2)e^{-\imath t\eta}\mathrm{d}t. \tag{2.10}$$

Similar to the case of WTF, applying the AFT on a function causes a twisting of its AFT.

2.2.2 Discrete Version of Affine Fourier Transform

The discrete transform serves a dual purpose of computing the continuous transform for spectral analysis and processing discrete data signals. Depending on the application, the input for the discrete transform can either be a sampled continuous function or a pure discrete sequence. In the former case, the input is obtained by sampling the continuous

function, while in the latter case, a pure discrete sequence is used as the input.

As a result, two types of DAFT can be obtained, which are essentially identical but with different parameterizations [50]. These parameterizations arise due to the different ways of representing the input signal for the two applications of the discrete transform. While the computation of the continuous transform requires a sampled continuous function as the input, the processing of discrete data signals uses a pure discrete sequence as the input. Despite the differences in input representation, the DAFT is a versatile tool that can be used for a variety of signal processing tasks.To derive the DAFT, input function $s(t)$ and $S_{a,b,c,d}(u)$ are sampled by the interval Δt and Δu as

$$s_n = s(n\Delta t), S_m = S_{a,b,c,d}(m\Delta u), \tag{2.11}$$

where $n = 0, ..., N-1$ and $m = 0, ..., M-1$. From (2.11), we can convert (2.3) as

$$S_m = \frac{1}{\sqrt{2\pi|b|}} \cdot \Delta t \cdot \mathrm{e}^{-\imath(\frac{a}{2b}m^2\Delta u^2)} \sum_{n=0}^{N-1} e^{-\imath(\frac{1}{b}mn\Delta u\Delta t + \frac{d}{2b}n^2\Delta t^2)} s_n. \tag{2.12}$$

This equation can be written in the form of transformation matrix

$$S_m = \sum_{n=0}^{N-1} F_{a,b,c,d}(m,n) s_n, \tag{2.13}$$

where $F_{a,b,c,d}(m,n) = \frac{1}{\sqrt{2\pi|b|}} \cdot \Delta t \cdot \mathrm{e}^{-\imath(\frac{a}{2b}m^2\Delta u^2 + \frac{1}{b}mn\Delta u\Delta t + \frac{d}{2b}n^2\Delta t^2)}$.

In order for (2.13) to be reversible, the following condition should hold [50]

$$\Delta t\Delta u = \frac{2\pi|b|}{M}. \tag{2.14}$$

Thus, the DAFT of the first type can be written as follows:

$$S_m = \frac{1}{\sqrt{M}} \mathrm{e}^{-\imath\frac{a}{2b}m^2\Delta u^2} \sum_{n=0}^{N-1} e^{-\imath(\frac{2\pi}{M}mn + \frac{d}{2b}n^2\Delta t^2)} s_n, \quad b > 0 \tag{2.15}$$

$$S_m = \frac{1}{\sqrt{M}} \mathrm{e}^{-\imath \frac{a}{2b} m^2 \Delta u^2} \sum_{n=0}^{N-1} e^{-\imath(-\frac{2\pi}{M} mn + \frac{d}{2b} n^2 \Delta t^2)} s_n, \quad b < 0. \tag{2.16}$$

The second type of DAFT [50] can be obtained by defining $c_1 = \frac{d}{4\pi b}\Delta t^2$ and $c_2 = \frac{a}{4\pi b}\Delta u^2$. With this definition, S_m in (2.13) becomes $S_m = \sum_{n=0}^{N-1} F_{c_1,c_2}(n,m) s_n$, where $F_{c_1,c_2}(n,m)$ is given by

$$F_{c_1,c_2}(n,m) \triangleq \frac{1}{\sqrt{M}} \mathrm{e}^{-\imath 2\pi (c_2 m^2 + \frac{sgn(b)}{M} mn + c_1 n^2)}. \tag{2.17}$$

The constraint in (2.14) can then be written as $c_1 c_2 = \frac{ad}{4M^2}$. Since a and d can take any real value as long as b and c are adjusted to satisfy $ad - bc = 1$, c_1 and c_2 have no constraints and can take any real value.Further simplification follows from fixing $sgn(b) = 1$, i.e., the DAFT is defined as

$$S_m = \frac{1}{\sqrt{M}} \mathrm{e}^{-\imath 2\pi c_2 m^2} \sum_{n=0}^{N-1} e^{-\imath 2\pi (\frac{1}{M} mn + c_1 n^2)} s_n, \tag{2.18}$$

where $M \geq N$ and its inverse transform is the following

$$s_n = \frac{1}{\sqrt{M}} \mathrm{e}^{\imath 2\pi c_1 n^2} \sum_{m=0}^{M-1} e^{\imath 2\pi (\frac{1}{M} mn + c_2 m^2)} S_m. \tag{2.19}$$

Moreover, we should take into account that sampling in one domain imposes periodicity in another domain. Considering (2.18) and (2.19), the following periodicity can be seen

$$S_{m+kM} = e^{-\imath 2\pi c_2 (k^2 M^2 + 2kMm)} S_m, \tag{2.20}$$

$$s_{n+kN} = e^{\imath 2\pi c_1 (k^2 N^2 + 2kNn)} s_n. \tag{2.21}$$

By setting $M = N$, the DAFT can be used to establish a multi-carrier signal that has two key properties. Firstly, the inter-carrier orthogonality ensures that the signal is composed of distinct, non-overlapping frequency components. Secondly, the signal can be generated or received using a transmitter or receiver, respectively, whose main component is an

IDFT or DFT module. With $M = N$, the inverse transform is the same as the forward transform with parameters $-c_1$ and $-c_2$ and conjugating the Fourier transform term. In matrix representation, arranging samples s_n and S_m in the period $[0, N)$ in vectors

$$\mathbf{s} = (s_0, s_1, ..., s_{N-1}), \tag{2.22}$$

$$\mathbf{S} = (S_0, S_1, ..., S_{N-1}), \tag{2.23}$$

the DAFT can be represented as $\mathbf{S} = \mathbf{A}\mathbf{s}$ with $\mathbf{A} = \mathbf{\Lambda}_{c_2}\mathbf{F}\mathbf{\Lambda}_{c_1}$, $\mathbf{F}$ being the DFT matrix with entries $e^{-\imath 2\pi mn/N}/\sqrt{N}$ and

$$\mathbf{\Lambda}_c = \text{diag}(e^{-\imath 2\pi c n^2}, n = 0, 1, \ldots, N-1). \tag{2.24}$$

The inverse of the matrix $\mathbf{A}$ is given by $\mathbf{A}^{-1} = \mathbf{A}^H = \mathbf{\Lambda}_{c_1}^H \mathbf{F}^H \mathbf{\Lambda}_{c_2}^H$. We can now show that $\{F_{c_1,c_2}(n,m)\}_{m=0\cdots M-1}$ with $sgn(b) = 1$ and $M = N$ forms an orthonormal basis of $\mathbb{C}^N$, i.e,

$$\sum_{n=0}^{N-1} F_{c_1,c_2}(n, m_1) F^*_{c_1,c_2}(n, m_2) = \frac{1}{N} e^{-\imath 2\pi c_2 (m_1^2 - m_2^2)} \times \sum_{n=0}^{N-1} e^{-\imath \frac{2\pi}{N}(m_1 - m_2)n} = \delta(m_1 - m_2). \tag{2.25}$$

2.3 Conclusion

In conclusion, this chapter has provided an overview of the two main topics that form the background for the rest of the manuscript: wireless channels and the AFT and its discrete version. We have discussed the characteristics and models of wireless channels, which are crucial for the design and evaluation of wireless communication systems. We have also introduced the AFT and its discrete version, which are the foundation of the AFDM technique used in the rest of the manuscript. By understanding these concepts, readers will be better equipped to understand the subsequent chapters and the research

presented in this manuscript.

Chapter 3

AFDM

In this chapter, we will delve into the principles of AFDM modulation. AFDM inherits the benefits of the DAFT by multiplexing information symbols in the DAFT domain, leading to a robust modulation technique for wireless communication systems. This chapter will provide detailed descriptions of the transmitter and receiver sides of AFDM, followed by an analysis of the input-output relation. Additionally, we will discuss the crucial aspect of parameter setting in AFDM, which plays a significant role in determining the performance of the communication system. The aim of this chapter is to provide a comprehensive understanding of the fundamental concepts of AFDM, laying the groundwork for its implementation and evaluation in practical communication systems.

3.1 Principle of AFDM

In this section, we will explore the principle of AFDM modulation in further detail. AFDM is a robust modulation technique that offers significant advantages over traditional OFDM in wireless communication systems. For notational clarity, we will use the symbol N to denote the number of chirp subcarriers in AFDM. Similarly, we will use the subcarrier spacing Δf and frame duration $T = N\Delta t$, which are well-known definitions in OFDM transmissions. This section will provide a comprehensive description of the transmitter

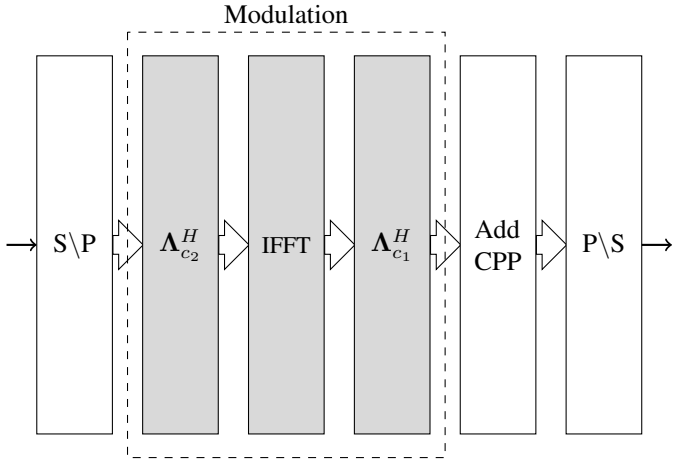

Figure 3.1: AFDM transmitter block-diagram

and receiver sides of AFDM, outlining the key components that enable the efficient multiplexing of information symbols in the DAFT domain.

3.1.1 AFDM Modulation

Let us consider the transmitter diagram of the AFDM modulation as shown in Fig. 3.1. AFDM uses a vector of information symbols $\mathbf{x} \in \mathbb{A}^{N\times 1}$ in the discrete affine Fourier domain for transmission. Here, $\mathbb{A} \subset \mathbb{Z}[j]$ represents the alphabet, and $\mathbb{Z}[j]$ denotes the number field whose elements have the form $z_r + z_i j$, where z_r and z_i are integers. QAM symbols are considered in the remainder of the transmission. As indicated by Fig. 3.1, the transmitted symbol $s[n]$ in the time domain is obtained via the DAFT of $x[n]$. i.e.,

$$s[n] = \sum_{m=0}^{N-1} x[m]\phi_n(m), \quad n = 0, \cdots, N-1, \tag{3.1}$$

where $\phi_n(m) = \frac{1}{\sqrt{N}} \cdot e^{\imath 2\pi(c_1 n^2 + c_2 m^2 + nm/N)}$.

Similar to OFDM, a prefix is necessary in the proposed AFDM scheme to mitigate multipath propagation and create the illusion of a periodic channel. However, due to the different signal periodicity as expalined in (2.21), an AFDM modulation uses a *chirp-periodic* prefix (CPP) instead of an OFDM CP. The CPP is inserted at the beginning of

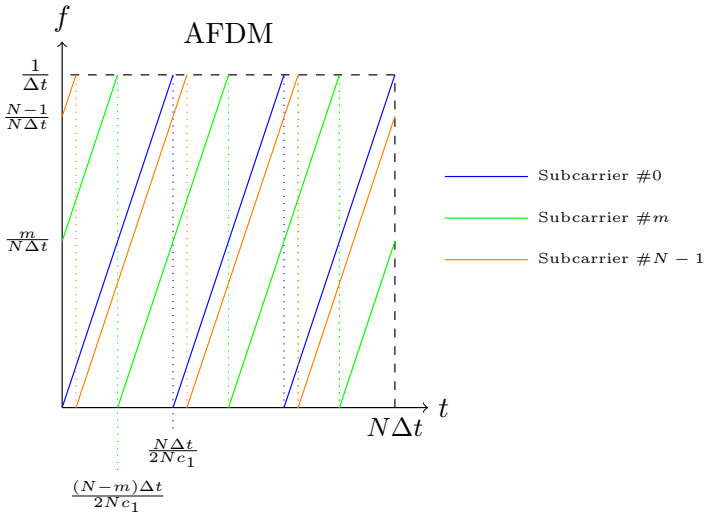

Figure 3.2: Time-frequency representation of AFDM subcarriers

the frame and is L_{cp} samples long, where L_{cp} is any integer greater than or equal to the maximum delay spread of the channel in samples. To achieve periodicity, the prefix is defined as:

$$s[n] = s[N+n]e^{-\imath 2\pi c_1(N^2+2Nn)}, \quad n = -L_{\text{cp}}, \cdots, -1. \tag{3.2}$$

Note that if $2Nc_1$ is an integer value and N is even, the CPP becomes equivalent to a CP. In this case, the prefix is simply an L_{cp}-length copy of the last L_{cp} samples of the frame. The CPP plays a crucial role in the AFDM modulation as it enables the receiver to extract the transmitted symbols from the received signal.

The TF domain representation of AFDM modulation is depicted in Fig. 3.2, showing the AFDM symbols in the TF domain. As illustrated in the figure, the values of the TF domain symbols are dependent on the corresponding DAFT domain symbols. It is worth noting that each DAFT domain symbol spreads over the entire TF plane before transmission, which implies that the DAFT domain symbol undergoes channel fluctuations across the whole TF domain, thus providing the potential to achieve full channel diversity. More details on achieving full channel diversity will be discussed in Chapter 4.

After the Digital-to-Analog conversion, the continuous signal needs to be articulated in a way that reflects the time-frequency representation, as shown in Fig. 3.2. Accordingly, the instantaneous frequency of the $m-$th chirp subcarrier can be written as

$$f_m(t) \triangleq \mathrm{mod}(2c_1'(t)_T + \frac{1}{T}m, \frac{1}{\Delta t}) = 2c_1'(t)_T + \frac{1}{T}m + \alpha_m((t)_T), \tag{3.3}$$

where $c_1' = \frac{c_1}{\Delta t^2}$ and $\alpha_m((t)_T)$ in $0 \leq t < T$ as shown in Fig. 3.3 represents the effect of discontinuities in the instantaneous frequency of the $m-$th chirp subcarrier due to the spectrum folding and writes as

$$\alpha_m(t) = -\lfloor \Delta t(2c_1't + \frac{1}{T}m) \rfloor \frac{1}{\Delta t} = \begin{cases} 0, & 0 \leq t < t_{m,1} \\ -\frac{1}{\Delta t}, & t_{m,1} \leq t < t_{m,2} \\ \vdots & \\ -\frac{C}{\Delta t}, & t_{m,C} \leq t < T \end{cases} \tag{3.4}$$

where $C \triangleq 2Nc_1$ and

$$t_{m,q} = \begin{cases} 0, & q = 0 \\ \frac{(N-m)}{2Nc_1}\Delta t + \frac{q-1}{2c_1}\Delta t, & 1 \leq q \leq C \end{cases}. \tag{3.5}$$

To represent $s(t)$, we need to derive the instantaneous phase $\Phi_m(t)$ from the instantaneous frequency $f_m(t)$. Given the discontinuities in $f_m(t)$, the phase should be defined piece-wise

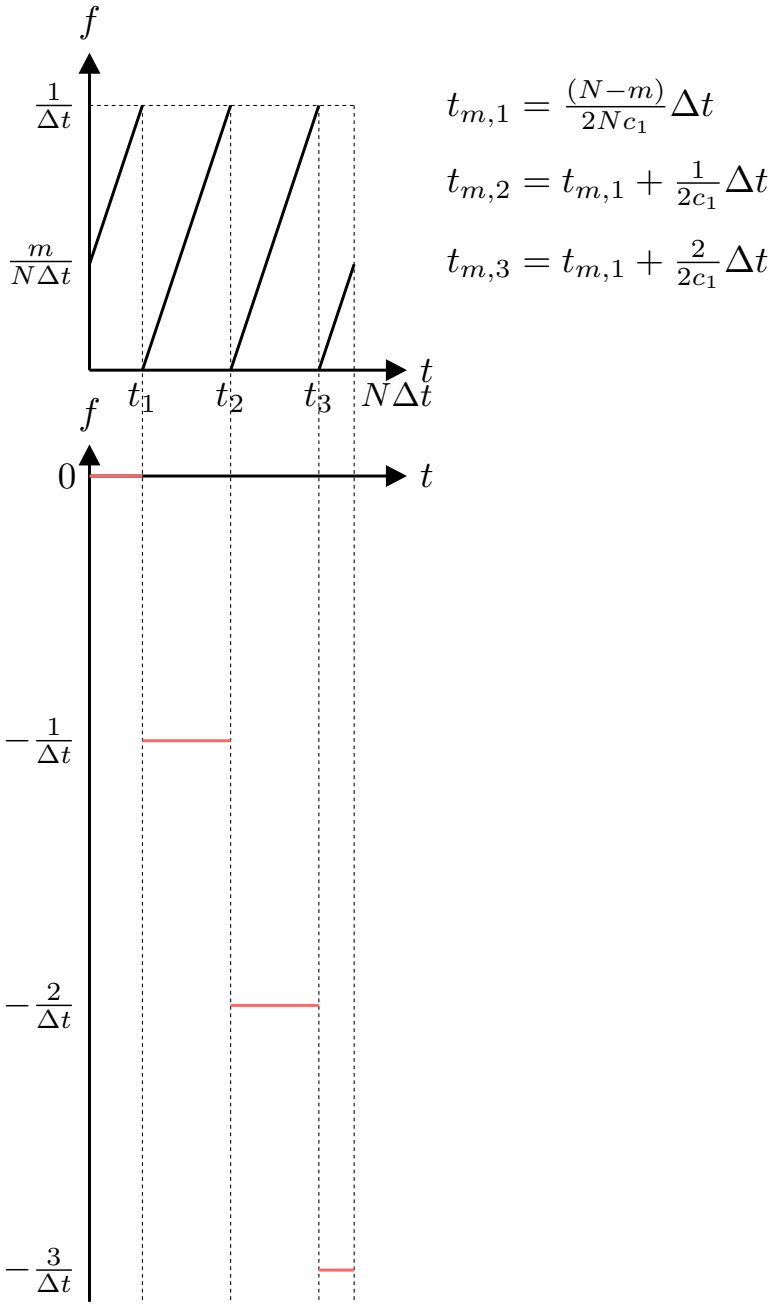

Figure 3.3: Time-frequency representation of m-th AFDM chirp (on top) and $\alpha_m((t)_T)$ (on bottom)

using the intervals $\{[t_{m,q}, t_{m,q+1})\}_{q=0,\cdots,C}$ as

$$\begin{aligned}\Phi_m(t) &= c_1' t^2 + \frac{m}{T}t + \begin{cases} \int_0^t \alpha_m(s)ds + \varphi_{m,0},, & 0 \le t < t_{m,1} \\ \vdots & \\ \int_{t_{m,q}}^t \alpha_m(s)ds + \varphi_{m,q}, & t_{m,q} \le t < t_{m,q+1} \\ \vdots & \\ \int_{t_{m,C}}^t \alpha_m(s)ds + \varphi_{m,C}, & t_{m,C} \le t < T \end{cases} \\ &= c_1' t^2 + \frac{m}{T}t + \begin{cases} 0, & 0 \le t < t_{m,1} \\ \vdots & \\ \frac{q}{2c_1}(q - \frac{m}{N}) - \frac{q}{\Delta t}t + \varphi_{m,q}, & t_{m,q} \le t < t_{m,q+1} \\ \vdots & \\ \frac{C}{2c_1}(C - \frac{m}{N}) - \frac{C}{\Delta t}t + \varphi_{m,C}, & t_{m,C} \le t < T \end{cases}, \end{aligned} \tag{3.6}$$

where $\varphi_{m,q}$ will be given in (3.9). Consequently, the continuous time signal for $q = 0, \cdots, C$ is defined as

$$\begin{aligned} s(t) &= \frac{1}{\sqrt{T}} \sum_{m=0}^{N-1} x[m] e^{\imath 2\pi (c_2 m^2 + \Phi_m(t))} \\ &= \frac{1}{\sqrt{T}} \sum_{m=0}^{N-1} x[m] e^{\imath 2\pi (c_2 m^2 + c_1' t^2 + \frac{m}{T}t + \frac{q}{2c_1}(q - \frac{m}{N}) - \frac{q}{\Delta t}t + \varphi_{m,q})}, t_{m,q} \le t < t_{m,q+1} \end{aligned} \tag{3.7}$$

This new formulation essentially recreates the time-frequency representation of the original discrete signal within the continuous time domain. To establish the value of $\varphi_{m,q}$, the sampling of $s(t)$, expressed as $s(n\Delta t)$, should yield $s[n]$ as outlined in equation (3.1), i.e., $\sqrt{\Delta t} s(n\Delta t) = s[n]$. The $s(n\Delta t)$ for $q = 0, \cdots, C$, can consequently be written as

$$\sqrt{\Delta t} s(n\Delta t) = \frac{1}{\sqrt{N}} \sum_{m=0}^{N-1} x[m] e^{\imath 2\pi (c_2 m^2 + c_1' (n\Delta t)^2 + \frac{m}{T} n\Delta t + \frac{q}{2c_1}(q - \frac{m}{N}) - qn + \varphi_{m,q})}$$

$$\lfloor \frac{t_{m,q}}{\Delta t} \rfloor + 1 \leq n \leq \lfloor \frac{t_{m,q+1}}{\Delta t} \rfloor, \quad (3.8)$$

As $\sqrt{\Delta t}s(n\Delta t)$ needs to equate to $s[n]$, $\varphi_{m,q} + \int_{t_{m,q}}^{n\Delta t} \alpha_m(s)ds$ is required to be an integer so that $e^{\varphi_{m,q}+\int_{t_{m,q}}^{n\Delta t} \alpha_m(s)ds} = 1$. This condition is satisfied when the following equation holds

$$\begin{aligned} \varphi_{m,q} &= \lfloor \int_{t_{m,q}}^{n\Delta t} \alpha_m(s)ds) \rfloor - \int_{t_{m,q}}^{n\Delta t} \alpha_m(s)ds) \\ &= \lfloor \frac{q}{2c_1}(q - \frac{m}{N}) - qn \rfloor - \frac{q}{2c_1}(q - \frac{m}{N}) - qn \\ &= \lfloor \frac{q}{2c_1}(q - \frac{m}{N}) \rfloor - \frac{q}{2c_1}(q - \frac{m}{N}) \end{aligned} \quad (3.9)$$

Substituting (3.9) in (3.10) gives

$$\begin{aligned} \sqrt{\Delta t}s(n\Delta t) &= \frac{1}{\sqrt{N}} \sum_{m=0}^{N-1} x[m] e^{\imath 2\pi (c_2 m^2 + c_1'(n\Delta t)^2 + \frac{m}{T} n\Delta t + \lfloor \frac{q}{2c_1}(q - \frac{m}{N}) \rfloor - qn)} \\ &= \frac{1}{\sqrt{N}} \sum_{m=0}^{N-1} x[m] e^{\imath 2\pi (c_2 m^2 + c_1 n^2 + \frac{m}{N} n)} = s[n] \quad \lfloor \frac{t_{m,q}}{\Delta t} \rfloor + 1 \leq n \leq \lfloor \frac{t_{m,q+1}}{\Delta t} \rfloor, \end{aligned} \quad (3.10)$$

which confirms $\sqrt{\Delta t}s(n\Delta t) = s[n]$

3.1.2 AFDM Demodulation

At the receiver side, the goal is to retrieve the information symbols transmitted by the transmitter. The received signal $r[n]$ in the time domain is the distorted version of the transmitted signal $s[n]$, which is affected by channel impairments such as attenuation, noise, and multipath propagation. The relationship between $s[n]$ and $r[n]$ will be discussed in detail in the upcoming subsection.

After discarding the CPP as shown in Fig. 3.4, the received signal $r[n]$ is processed by the AFDM demodulator to obtain the DAFT domain output symbols. The demodulator implements the DAFT, which transforms $r[n]$ from the time domain to the DAFT domain as written in (3.11). In the DAFT domain, the received signal is represented as a

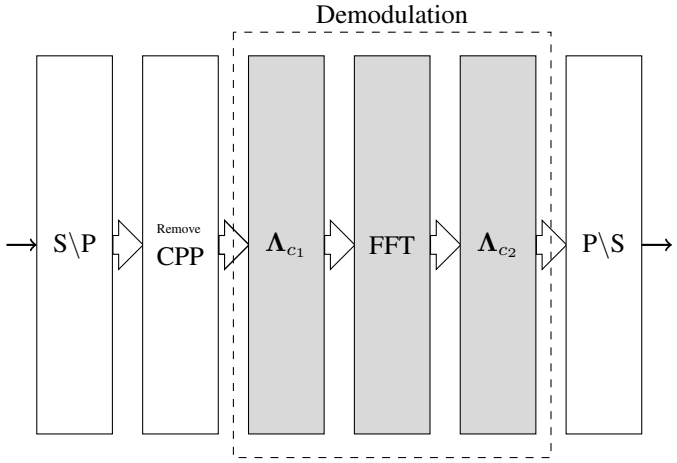

Figure 3.4: AFDM receiver block-diagram

vector of complex numbers that correspond to the information symbols transmitted by the transmitter. These output symbols are then decoded to recover the transmitted information.

$$y[m] = \sum_{n=0}^{N-1} r[n]\phi_n^*(m). \tag{3.11}$$

3.1.3 Channel Model

As discussed earlier, we consider a doubly selective channel given in (2.1). To obtain a discrete channel model, we consider sampling of the channel model. With the given time-frequency resources, the sample resolution along the delay and Doppler domains are $\frac{1}{N\Delta f}$ and $\frac{1}{T}$, respectively. Let us define the delay and Doppler shift indices associated with the p-th path by l_p and k_p, respectively, such that

$$\tau_p = \frac{l_p + \iota_p}{N\Delta f}, \quad f_p = \frac{k_p + \kappa_p}{T}, \tag{3.12}$$

where k_p denotes the integer part of the Doppler shift for the p-th path, and κ_p represents the corresponding fractional Doppler shift. Similarly, l_p denotes the integer part of the

delay for the p-th path, and ι_p represents the corresponding fractional delay. It is worth noting that the terms $\frac{-1}{2} < \iota_p \leq \frac{1}{2}$ and $\frac{-1}{2} < \kappa_p \leq \frac{1}{2}$ are the shifts from the nearest integer delay and Doppler shift indices, respectively. Regarding the Doppler shift, we have $k_p + \kappa_p \in [-k_{\max}, k_{\max}]$. Here, $k_{\max}$ is the maximum Doppler shift index, which can be expressed as $k_{\max} = \lceil T f_{\max} \rceil$, where $f_{\max}$ is the maximum Doppler shift value. As for delays, the interval is defined as $l_p + \iota_p \in [0, l_{\max}]$, where $l_{\max}$ represents the maximum delay index, which can be expressed as $l_{\max} = \lceil N \Delta f \tau_{\max} \rceil$, and $\tau_{\max}$ is the maximum delay value.

3.2 Input-Output relation

With the introduction of modulation, channel modeling, and demodulation in AFDM, we can now examine the input-output relation of the system. Taking into account the channel model described in (2.1), the continues time domain received signal $r(t)$ can be expressed as

$$r(t) = \int s_{\mathrm{CPP}}(t-\tau) h(t,\tau) \mathrm{d}\tau + w(t) = \sum_{p=0}^{P-1} s_{\mathrm{CPP}}(t-\tau_p) h(t,\tau_p) + w(t) \tag{3.13}$$

where

$$s_{\mathrm{CPP}}(t) = \begin{cases} s(t), & 0 \leq t \leq T \\ s(t+T) e^{-\imath 2\pi c_1'(T^2+2Tt)}, & -L_{\mathrm{cp}} \Delta t \leq t < 0. \end{cases} \tag{3.14}$$

where $w(t) \sim \mathcal{CN}(0, N_0)$ is an additive Gaussian noise. Since we need to do the modulation with the received signal samples, first we need to sample the received signal $r(t)$ at every $\Delta t = \frac{T}{N}$ seconds which writes as

$$r(n\Delta t) = \sum_{p=0}^{P-1} s_{\mathrm{CPP}}(n\Delta t - \tau_p) h(n\Delta t, \tau_p) + w(n\Delta t) \tag{3.15}$$

For the ease of presentation, we ignore the noise term in the corresponding equations in the following derivations. Subsequently, by substituting the continues modulated signal derived in (3.10) into (3.15), we obtain the resulting expression that relates the information symbols and received signal as

$$\begin{aligned}\sqrt{\Delta t}r(n\Delta t) &= \frac{1}{\sqrt{N}}\sum_{p=1}^{P}\sum_{m=0}^{N-1} h_p e^{-\imath\frac{2\pi}{T}f_p n\Delta t} x[m] e^{\imath 2\pi(c_2 m^2 + c_1'(n\Delta t-\tau_p)_T^2 + \frac{m}{T}(n\Delta t-\tau_p)_T)} \\ &\qquad \times e^{\imath 2\pi(\sum_{q=0}^{C}(\lfloor\frac{q(q-m/N)}{2c_1}\rfloor - q\frac{(n\Delta t-\tau_p)_T}{\Delta t})I_{\boldsymbol{\mathcal{T}}_{m,q}}((n\Delta t-\tau_p)_T)}\gamma_{\mathrm{CPP}}(n\Delta t-\tau_p) \\ &= \frac{1}{\sqrt{N}}\sum_{p=1}^{P}\sum_{m=0}^{N-1} h_p x[m] \underbrace{\gamma_{\mathrm{CPP}}(n\Delta t-\tau_p)e^{\imath 2\pi c_1'(n\Delta t-\tau_p)_N^2}}_{a_{\mathrm{cpp_p}}} e^{\imath 2\pi(c_2 m^2 + \frac{m}{T}(n\Delta t-\tau_p)_T - \frac{1}{T}f_p n\Delta t)} \\ &\qquad \times e^{\imath 2\pi(\sum_{q=0}^{C}(\lfloor\frac{q(q-m/N)}{2c_1}\rfloor - q\frac{(n\Delta t-\tau_p)_T}{\Delta t})I_{\boldsymbol{\mathcal{T}}_{m,q}}((n\Delta t-\tau_p)_T)}, \end{aligned} \tag{3.16}$$

where

$$\gamma_{\mathrm{CPP}}(t) = \begin{cases} 1 & t \geq 0 \\ e^{-\imath 2\pi c_1'(T^2+2Tt)} & t < 0 \end{cases}. \tag{3.17}$$

and

$$I_{\boldsymbol{\mathcal{T}}_{m,q}}(t) = \begin{cases} 1 & t \in \boldsymbol{\mathcal{T}}_{m,q} \triangleq [t_{m,q}, t_{m,q+1}), \\ 0 & t \notin \boldsymbol{\mathcal{T}}_{m,q}. \end{cases} \tag{3.18}$$

With the the following simplification

$$\begin{aligned} a_{\mathrm{cpp_p}} = \gamma_{\mathrm{CPP}}(n\Delta t-\tau_p)e^{\imath 2\pi c_1'(n\Delta t-\tau_p)_T^2} &= \begin{cases} e^{\imath 2\pi c_1(n\Delta t-\tau_p)^2} & t \geq \tau_p \\ e^{-\imath 2\pi c_1'(T^2+2T(n\Delta t-\tau_p)-(n\Delta t-\tau_p+T)^2)} & t < \tau_p \end{cases} \\ &= e^{\imath 2\pi c_1'(n\Delta t-\tau_p)^2} \end{aligned} \tag{3.19}$$

(3.16) writes as

$$\sqrt{\Delta t}r(n\Delta t) = \frac{1}{\sqrt{N}}\sum_{p=1}^{P}\sum_{m=0}^{N-1} h_p x[m] e^{\imath 2\pi(c_1(n-(l_p+\iota_p))^2 + c_2 m^2 + (n-(l_p+\iota_p))m/N - \frac{k_p+\kappa_p}{N}n)}$$

$$\times e^{\imath 2\pi(\sum_{q=0}^{C}(\lfloor\frac{q(q-m/N)}{2c_1}\rfloor - q(n-(l_p+\iota_p))_N))I_{\boldsymbol{\mathcal{L}}_{m,q}}((n-(l_p+\iota_p))_N)}$$

$$= \frac{1}{\sqrt{N}}\sum_{p=1}^{P}\sum_{m=0}^{N-1} h_p x[m] e^{\imath 2\pi(c_1(n-(l_p+\iota_p))^2 + c_2 m^2 + (n-(l_p+\iota_p))m/N - \frac{k_p+\kappa_p}{N}n)} e^{\imath 2\pi(\sum_{q=0}^{C} q\iota_p I_{\boldsymbol{\mathcal{L}}_{m,q}}((n-(l_p+\iota_p))_N))}$$

$$= r[n], \tag{3.20}$$

where $\boldsymbol{\mathcal{L}}_{m,q}$ is the discrete version of $\boldsymbol{\mathcal{T}}_{m,q}$ and writes as

$$I_{\boldsymbol{\mathcal{L}}_{m,q}}(n) = \begin{cases} 1 & n \in \boldsymbol{\mathcal{L}}_{m,q} \triangleq \{n_{m,q}+1, \cdots n_{m,q+1}\}, \\ 0 & t \notin \boldsymbol{\mathcal{L}}_{m,q}. \end{cases} \tag{3.21}$$

where $n_{m,q} \triangleq \lfloor \frac{t_{m,q}}{\Delta t} \rfloor$. By substituting (3.20) into (3.11), we obtain the input-output relation as follows

$$\begin{aligned} y[m] &= \frac{1}{N}\sum_{n=0}^{N-1}\sum_{p=1}^{P}\sum_{m'=0}^{N-1} h_p x[m'] e^{\imath 2\pi(c_1(n-(l_p+\iota_p))^2 + c_2 m'^2 + (n-(l_p+\iota_p))m'/N - \frac{k_p+\kappa_p}{N}n)} \\ &\quad \times e^{\imath 2\pi\iota_p(\sum_{q=0}^{C} q I_{\boldsymbol{\mathcal{L}}_{m,q}}((n-(l_p+\iota_p))_N))} e^{-\imath 2\pi(c_1 n^2 + c_2 m^2 + nm/N)} + \tilde{w}[m] \\ &= \frac{1}{N}\sum_{n=0}^{N-1}\sum_{p=1}^{P}\sum_{m'=0}^{N-1} h_p x[m'] e^{\imath 2\pi(c_1(l_p+\iota_p)^2 + c_2(m'^2-m^2)} e^{\imath 2\pi/N(m'-(m+l_p^{\mathrm{eq}})n} \\ &\quad \times e^{-\imath 2\pi/N(l_p+\iota_p)m'} e^{\imath 2\pi\iota_p(\sum_{q=0}^{C} q I_{\boldsymbol{\mathcal{L}}_{m,q}}((n-(l_p+\iota_p))_N))} + \tilde{w}[m] \\ &= \frac{1}{N} e^{-\imath 2\pi c_2 m^2} \sum_{p=1}^{P} h_p e^{\imath 2\pi c_1 (l_p+\iota_p)^2} \sum_{m'=0}^{N-1} x[m'] e^{\imath 2\pi(c_2 m'^2 - (l_p+\iota_p)m'/N)} \\ &\quad \times \underbrace{\sum_{n=0}^{N-1} e^{\imath\frac{2\pi}{N}(m'-(m+l_p^{\mathrm{eq}}))n} e^{\imath 2\pi\iota_p(\sum_{q=0}^{C} q I_{\boldsymbol{\mathcal{L}}_{m,q}}((n-(l_p+\iota_p))_N))}}_{\mathcal{F}_p(m,m')} + \tilde{w}[m], \end{aligned} \tag{3.22}$$

where $\tilde{w}[m]$ represents the demodulated noise, which possesses the same statistical properties as $w[n]$ and $l_p^{\mathrm{eq}} \triangleq ((k_p+\kappa_p) + 2Nc_1 l_p)_N$ is defined as the equivalent delay. According to the value of l_p^{eq} and fractional delay ι_p, $\mathcal{F}_{p,q}(m,m')$ can be simplified. Assuming the $2Nc_1 \in \mathcal{N}$ as mentioned earlier, this simplification depends on fractional

dealy ι_p and fractional Doppler shift κ_p and $\mathcal{F}_{p,q}(m,m')$ can be written as

$$\mathcal{F}_p(m,m') = \begin{cases} \begin{cases} N\delta(m'-(m+l_p^{\text{eq}})_N) & \kappa_p = 0 \\ \frac{e^{\imath 2\pi(m'-m-l_p^{\text{eq}})}-1}{e^{\imath\frac{2\pi}{N}(m'-m-l_p^{\text{eq}})}-1} & \kappa_p \neq 0 \end{cases} & \iota_p = 0 \\ \sum_{q=0}^{C} e^{\imath 2\pi q\iota_p} \sum_{(n-(l_p+\iota_p))_N \in \boldsymbol{\mathcal{L}}_{m,q}} e^{\imath\frac{2\pi}{N}(m'-(m+l_p^{\text{eq}}))n} & \iota_p \neq 0 \end{cases}. \tag{3.23}$$

for the case when $\iota_p = \kappa_p = 0$, the input-output relation (3.22) can be expressed as

$$y[m] = \frac{1}{N} e^{-\imath 2\pi c_2 m^2} \sum_{p=1}^{P} h_p e^{\imath 2\pi c_1 l_p^2} x[(m+l_p^{\text{eq}})_N] e^{\imath 2\pi(c_2((m+l_p^{\text{eq}})_N)^2 - l_p(m+l_p^{\text{eq}})/N)} + \tilde{w}[m], \tag{3.24}$$

indicating that each output symbol is a linear combination of at most P input symbols, depending on the specific values of l_p^{eq}. However, for the case $\iota_p = 0$ and $\kappa_p \neq 0$, we have

$$y[m] = \frac{1}{N} e^{-\imath 2\pi c_2 m^2} \sum_{p=1}^{P} h_p e^{\imath 2\pi c_1 l_p^2} \sum_{m'=0}^{N-1} x[m'] e^{\imath 2\pi(c_2 m'^2 - l_p m'/N)} \frac{e^{\imath 2\pi(m'-m-l_p^{\text{eq}})}-1}{e^{\imath\frac{2\pi}{N}(m'-m-l_p^{\text{eq}})}-1} + \tilde{w}[m], \tag{3.25}$$

which implies that each output symbol is a linear combination of all input symbols. Although $\mathcal{F}_p(m,m')$ is nonzero for all m', it exhibits a peak at $m' = (m+l_p^{\text{eq}})_N$. As m' moves away from the peak, $\mathcal{F}_p(m,m')$ decreases. This behavior signifies that the influence of input symbols on the output symbol is more significant when their indices are in close proximity. Understanding the behavior of $\mathcal{F}_p(m,m')$ provides insights into the interdependence of input and output symbols in the AFDM modulation scheme.To show this, we have

$$\left|\frac{1}{N}\mathcal{F}_p(p,q)\right| = \left|\frac{\sin(N\theta)}{N\sin(\theta)}\right|, \tag{3.26}$$

where $\theta \triangleq \frac{\pi}{N}(m'-(m+l_p^{\text{eq}})_N)$. Using the inequality $|\sin(N\theta)| \leq |N\sin(\theta)|$, which is tight for small values of θ (when both sides are close to 1), we can show

$$\left|\frac{\sin(N\theta)}{N\sin(\theta)}\right| = \left|\frac{\sin((N-1)\theta)\cos(\theta)+\sin(\theta)\cos((N-1)\theta)}{N\sin(\theta)}\right| \leq \frac{N-1}{N}|\cos(\theta)| + \frac{1}{N}, \tag{3.27}$$

where it has a peak at the smallest value of θ when m' is the nearest integer number to $(m + l_p^{\text{eq}})_N$, i.e. $m' = \text{round}((m + l_p^{\text{eq}})_N) = m'^p_{\text{peak}}$. As $|\theta|$ increases due to m' moving away from the peak, the upper bound of $\mathcal{F}_p(m, m')$ gradually decreases. This decrease can be approximated by a slope of $\frac{\pi}{N}(m' - (m + l_p^{\text{eq}})_N)$. Notably, since N is typically large in AFDM, the function decreases rapidly as $|\theta|$ increases.

Based on the previous analysis, it is evident that we can focus on a limited number of significant values of $\mathcal{F}_p(p, q)$, with a range of $2k_\nu + 1$ values around the peak located at m'^p_{peak}. Here, k_ν represents a positive integer, significantly smaller than N. By leveraging this approximation, we can now express the received signal $y[m]$ in (3.25) as follows:

$$y[m] = \frac{1}{N}\sum_{p=1}^{P}\sum_{m'=(m'^p_{\text{peak}}-k_\nu)_N}^{(m'^p_{\text{peak}}+k_\nu)_N} h_p x[m'] e^{\imath 2\pi(c_1 l_p^2 - c_2(m^2-m'^2) - l_p m'/N)} \times \frac{e^{\imath 2\pi(m'-m-l_p^{\text{eq}})}-1}{e^{\imath\frac{2\pi}{N}(m'-m-l_p^{\text{eq}})}-1} + \tilde{w}[m], \tag{3.28}$$

3.3 Matrix Form Representation

In the previous subsections, we thoroughly examined the AFDM concept and its mathematical derivations. However, for the sake of convenience and a more concise representation, it is often useful to utilize an equivalent matrix form to describe the associated processing. In this subsection, we will first introduce the matrix form representation of the AFDM scheme for integer delays. Following that, we will extend our discussion to cover the general case, which includes fractional delays. To ensure coherence and clarity, we will maintain the same notations as in the previous subsection.

As previously mentioned, the DAFT matrix $\mathbf{A} = \mathbf{\Lambda}c_2\mathbf{F}\mathbf{\Lambda}c_1$ is utilized for modulation in the matrix form. Therefore, considering the information symbol vector $\mathbf{x}$, the transmitted symbol vector $\mathbf{s}$ in the time domain can be expressed as follows

$$\mathbf{s} = \mathbf{A}^H\mathbf{x} = \mathbf{\Lambda}_{c_1}^H\mathbf{F}^H\mathbf{\Lambda}_{c_2}^H\mathbf{x}. \tag{3.29}$$

For the integer delay case, in relation to the time-domain transmitted symbol vector $\mathbf{s}$, the time-domain channel matrix $\mathbf{H}_{\text{time}}$ considering the CPP can be represented as

$$\mathbf{H}_{\text{time}} = \sum_{p=1}^{P} h_p \mathbf{\Gamma}_{\text{CPP}_p} \mathbf{\Delta}_{f_p} \mathbf{\Pi}^{l_p}, \tag{3.30}$$

where $\mathbf{\Pi}$ is the forward cyclic-shift matrix, i.e,

$$\mathbf{\Pi} = \begin{bmatrix} 0 & \cdots & 0 & 1 \\ 1 & \cdots & 0 & 0 \\ \vdots & \ddots & \ddots & \vdots \\ 0 & \cdots & 1 & 0 \end{bmatrix}_{N \times N}, \tag{3.31}$$

$\mathbf{\Delta}_{f_p}$ and $\mathbf{\Gamma}_{\text{CPP}_p}$ are the $N \times N$ diagonal matrices as

$$\mathbf{\Delta}_{f_p} = \text{diag}(e^{-\imath 2\pi f_p n}, n = 0, 1, \ldots, N-1) \tag{3.32}$$

$$\mathbf{\Gamma}_{\text{CPP}_p} = \text{diag}(\begin{cases} 1 & n \geq l_p \\ e^{-\imath 2\pi c_1 (N^2 + 2N(n-l_p))} & n < l_p \end{cases}, n = 0, \ldots, N-1). \tag{3.33}$$

From (3.33) we can see that whenever $2Nc_1$ is an integer and N is even, $\mathbf{\Gamma}_{\text{CPP}_p} = \mathbf{I}$. Based on (3.30), the time domain received symbol vector $\mathbf{r}$ is given by

$$\mathbf{r} = \mathbf{H}_{\text{time}} \mathbf{s} + \mathbf{w}, \tag{3.34}$$

$\mathbf{w} \sim \mathcal{CN}(\mathbf{0}, N_0 \mathbf{I})$ is the noise vector. The AFDM demodulator, which retrieves the DAFT domain output symbol vector from $\mathbf{r}$, can be expressed in matrix form using the DAFT matrix $\mathbf{A}$ as

$$\mathbf{y} = \mathbf{A}\mathbf{r} = \mathbf{\Lambda}_{c_2} \mathbf{F} \mathbf{\Lambda}_{c_1} \mathbf{r}. \tag{3.35}$$

By incorporating (3.29), (3.34), and (3.35), we can express the input-output relationship

of the AFDM scheme in matrix form as follows

$$\mathbf{y} = \mathbf{A}\mathbf{r} = \mathbf{A}\mathbf{H}_{\text{time}}\mathbf{s} + \mathbf{A}\mathbf{w} = \mathbf{A}\mathbf{H}_{\text{time}}\mathbf{A}^H\mathbf{x} + \widetilde{\mathbf{w}} = \mathbf{H}_{\text{eff}}\mathbf{x} + \widetilde{\mathbf{w}}, \tag{3.36}$$

where $\mathbf{H}_{\text{eff}} \triangleq \mathbf{A}\mathbf{H}_{\text{time}}\mathbf{A}^H$ is effective channel matrix showing the input-output relaltion. Furthermore, the noise vector $\widetilde{\mathbf{w}}$ is obtained as $\widetilde{\mathbf{w}} = \mathbf{A}\mathbf{w}$, where $\mathbf{w}$ and $\widetilde{\mathbf{w}}$ have the same statistical properties due to the unitary nature of $\mathbf{A}$.

In order to see the input-output relation from the matrix $\mathbf{H}_{\text{eff}}$, it can be written as

$$\mathbf{H}_{\text{eff}} = \sum_{p=1}^{P} h_p \mathbf{H}_p = \sum_{p=1}^{P} h_p \mathbf{A}\boldsymbol{\Gamma}_{\text{CPP}_p}\boldsymbol{\Delta}_{f_p}\boldsymbol{\Pi}^{l_p}\mathbf{A}^H \tag{3.37}$$

where $h_p\mathbf{H}_p$ is effective channel matrix related to path p. It can be seen from (3.25) that the $H_p[m, m']$ can be written as

$$H_p[m, m'] = \frac{1}{N} e^{\imath 2\pi(c_1 l_p^2 - c_2(m^2 - m'^2) - l_p m'/N)} \frac{e^{\imath 2\pi(m' - m - l_p^{\text{eq}})} - 1}{e^{\imath \frac{2\pi}{N}(m' - m - l_p^{\text{eq}})} - 1}. \tag{3.38}$$

As discussed earlier, when $l_p^{\text{eq}} \in \mathcal{N}$ (integer delay and integer Doppler), each row and column of $\mathbf{H}_p$ contains only a single non-zero entry, as illustrated in Fig. 3.5. This characteristic can be expressed mathematically as

$$H_p[m, m'] = \begin{cases} e^{\imath 2\pi(c_1 l_p^2 - c_2(m^2 - m'^2) - l_p m'/N)} & m' = (m + l_p^{\text{eq}})_N \\ 0 & \text{otherwise} \end{cases}. \tag{3.39}$$

Furthermore, when we have fractional Doppler we demonstrated that while each output symbol for each path is a linear combination of all input symbols, there are only a few significant values to consider. Specifically, there are $2k_\nu + 1$ significant values for each

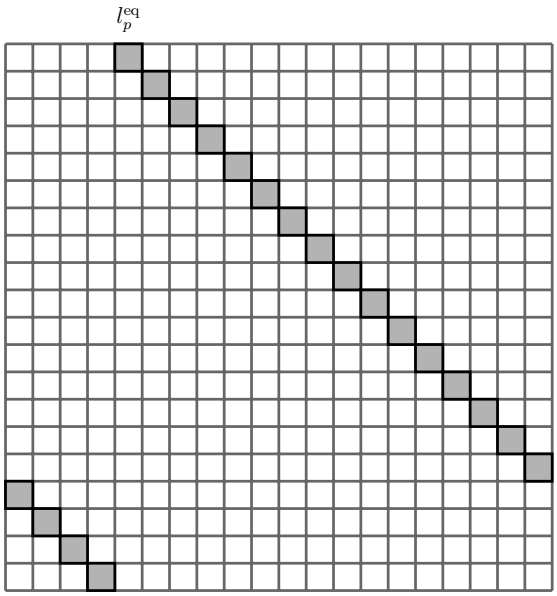

Figure 3.5: Structure of $\mathbf{H}_p$ for integer Doppler shifts

path, resulting in the channel matrix $\mathbf{H}_p$ shown in Fig. 3.6 and expressed as

$$H_p[m,m'] = \begin{cases} \frac{1}{N} e^{\imath 2\pi(c_1 l_p^2 - c_2(m^2-m'^2) - l_p m'/N)} \frac{e^{\imath 2\pi(m'-m-l_p^{\mathrm{eq}})}-1}{e^{\imath \frac{2\pi}{N}(m'-m-l_p^{\mathrm{eq}})}-1} & (m'^p_{\mathrm{peak}} - k_\nu)_N \leq m' \leq (m'^p_{\mathrm{peak}} + k_\nu)_N \\ 0 & \text{otherwise} \end{cases}. \tag{3.40}$$

By incorporating the fractional delay into consideration, the matrix $\mathbf{H}_{\mathrm{time}}$ in (3.30) cannot be represented with the permutation matrix, necessitating the use of an over-sampled version of the modulated signal. Despite this, as the input-output relation for the fractional delay is already formulated in (3.23), $\mathbf{H}_{\mathrm{eff}} = \sum_{p=1}^{P} h_p \mathbf{H}_p$ can be effectively obtained. Utilizing $\mathbf{H}_{\mathrm{eff}}$ enables the derivation of $\mathbf{H}_{\mathrm{time}}$ which inherently includes the

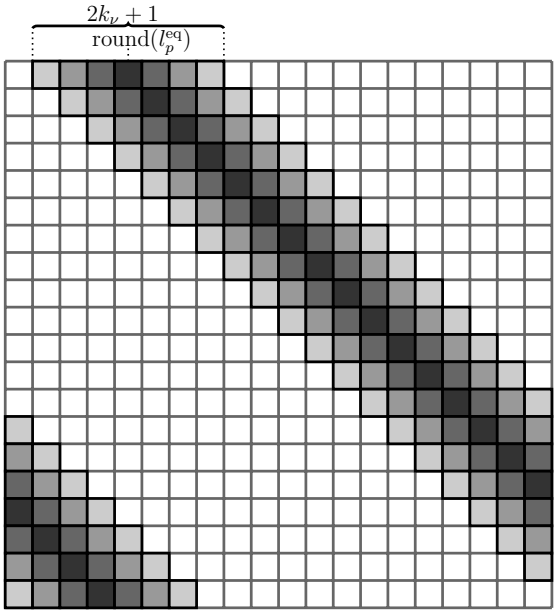

Figure 3.6: Structure of $\mathbf{H}_p$ for fractional Doppler shifts

effect of the fractional delay. In this scenario, $H_p[m, m']$ can be expressed as follows

$$H_p[m,m'] = \frac{1}{N} e^{\imath 2\pi (c_1(l_p+\iota_p)^2 - c_2(m^2-m'^2) - (l_p+\iota_p)m'/N)} \sum_{q=0}^{C} e^{\imath 2\pi q \iota_p} \times \sum_{(n-(l_p+\iota_p))_N \in \boldsymbol{\mathcal{L}}_{m,q}} e^{\imath \frac{2\pi}{N}(m'-(m+l_p^{\text{eq}}))n} 0 \leq m' \leq N-1, \tag{3.41}$$

and as we have $\mathbf{H}_{\text{eff}} = \mathbf{A}\mathbf{H}_{\text{time}}\mathbf{A}^H$, $\mathbf{H}_{\text{time}}$ can be calculated as

$$\mathbf{H}_{\text{time}} = \mathbf{A}^H \mathbf{H}_{\text{eff}} \mathbf{A} \tag{3.42}$$

3.4 Parameters Setting

The input-output relation of the AFDM scheme, as discussed in previous sections, is influenced by the values of l_p^{eq} for each path $p = 1, ..., P$. In this section, the fractional delay is not taken into account. This practical assumption is based on the insight that the resolution of the sampling time $1/N\Delta f$ is sufficiently precise to approximate the path

delays to the nearest sampling points in typical wide-band systems. It can be observed that $l_p^{\text{eq}} = ((k_p + \kappa_p) + 2Nc_1 l_p)_N$ is determined by the delay-Doppler information of path p and the AFDM parameter c_1. The value of l_p^{eq} plays a crucial role in the system's behavior and can be tuned based on specific criteria such as diversity analysis or channel estimation overhead which will be discussed in the next chapters.

For instance, if $2Nc_1$ is an integer, the condition we previously discussed depends solely on the Doppler shift. In this manuscript, as mentioned earlier, we adopt a setting where c_1 is chosen as $c_1 = \frac{C}{2N}$, where C is an integer. This choice results in a system where the structure of $\mathbf{H}_p$ is primarily influenced by the Doppler shift, whether it is fractional or not.

In addition to considering the individual path characteristics, it is essential to analyze the overall structure of the effective channel matrix $\mathbf{H}_{\text{eff}}$, which incorporates the contributions of all paths. One crucial aspect in the structure of $\mathbf{H}_{\text{eff}}$ is the value of $m'^p\text{peak}$, which indicates how the paths are positioned within $\mathbf{H}_{\text{eff}}$. The location of the paths within $\mathbf{H}_{\text{eff}}$ influences the interplay between different paths and impacts the overall system performance.

Fig. 3.7 illustrates two figures representing a 3-path channel, showcasing the potential variations in its structure based on different values of c_1. The structure of the effective channel matrix $\mathbf{H}_{\text{eff}}$ can exhibit distinct characteristics depending on the chosen value of c_1. By analyzing these figures, we can observe how the paths are distributed within $\mathbf{H}_{\text{eff}}$ and gain insights into the interdependencies among the paths. The variations in structure highlight the importance of selecting an appropriate value for c_1 to achieve desired system performance.

Understanding the different structural possibilities of the effective channel matrix further emphasizes the flexibility and adaptability of the AFDM scheme. By tailoring the value of c_1, we can effectively control the behavior of the channel and optimize the system to meet specific requirements. In the upcoming chapters, we will conduct a

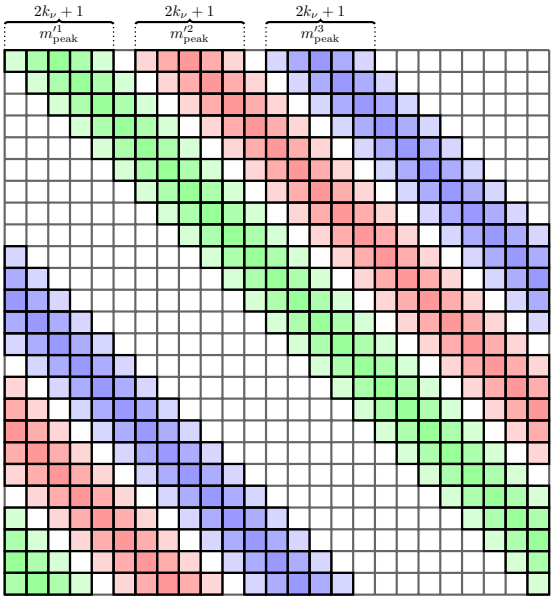

(a)

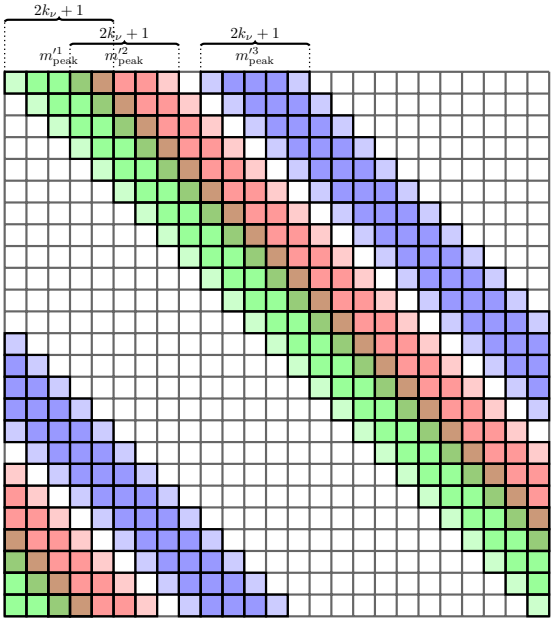

(b)

Figure 3.7: Structure of $\mathbf{H}_{\text{eff}}$ for the same channel with different c_1 values

detailed analysis of the channel structures introduced earlier and explore their effects on the performance of the AFDM system. Our aim is to gain comprehensive insights into the behavior of AFDM in various scenarios and understand the impact of tuning on important aspects such as diversity analysis and channel estimation overhead.

3.5 Conclusion

In this chapter, we have thoroughly explored the principle of AFDM and its key components. We have covered the AFDM modulation process, which involves mapping information symbols from the DAFT domain to the time domain using the IDAFT. Additionally, we have discussed the AFDM demodulation process, highlighting the use of the DAFT matrix to extract the DAFT domain output symbols from the received symbols. The channel model in AFDM, taking into account the effects of Doppler shift and delay, has also been analyzed. Furthermore, we have presented the matrix representation of the AFDM scheme, which offers a concise and convenient framework for analyzing and understanding the signal processing involved.

To provide a comprehensive understanding of AFDM, we have discussed the input-output relation in both mathematical equations and matrix forms. By examining the effective channel matrix, we have gained insights into the relationships between input and output symbols for different paths. Additionally, we have emphasized the significance of parameter setting, particularly the selection of c_1, which has a significant impact on the structure of the effective channel matrix and subsequently affects important aspects such as diversity analysis and channel estimation overhead.

Chapter 4

AFDM for full diversity on LTV channels

In this chapter, we delve into the capability of AFDM to harness the full diversity order of the channel. Our exploration starts by highlighting the fine-tuning of AFDM parameters, ensuring the system can identify all paths with different delays and Doppler shifts. This tuning facilitates the distinct separation of each path, enabling a full delay-Doppler representation of the channel. Building upon this foundation, we then offer an analytical proof that, with these selected parameters, AFDM achieves the full diversity order of the LTV channels. Reinforcing our claims, we conclude with simulation results that confirm AFDM as a full diversity scheme for LTV channels.

4.1 AFDM parameters Setting for full diversity

As mentioned earlier, the performance of DAFT-based modulation schemes relies heavily on the selection of parameters c_1 and c_2. For instance, OCDM uses $c_1 = c_2 = \frac{1}{2N}$, whereas in DAFT-OFDM $c_2 = 0$ and c_1 are adapted to the delay-Doppler channel profile to minimize ICI. However, these existing schemes fail to achieve the optimal diversity order in LTV channels. In this section, we focus on the parameter setting for full diversity in

AFDM.

In full-diversity AFDM, we aim to find suitable values for c_1 and c_2 that ensure the DAFT domain impulse response represents the full delay-Doppler profile of the channel. This enables AFDM to achieve the optimal diversity order in LTV channels, as demonstrated in Section 4.2. To achieve this, it is crucial to ensure that the non-zero entries in each row of the channel matrices $\mathbf{H}_i$ for each path i do not overlap with the non-zero entries in the same row of other channel matrices $\mathbf{H}_j$ where $j \neq i$. By observing the expressions for $\mathbf{H}_i$ in both the integer and fractional Doppler shift cases (as given in (3.40)), we can see that the positioning of each path depends on its specific delay-Doppler information and the AFDM parameters as

$$-k_{\max} - k_\nu + 2Nc_1 l_p \leq \text{round}((l_p^{\text{eq}})_N) \leq k_{\max} + k_\nu + 2Nc_1 l_p. \tag{4.1}$$

In order to achieve full diversity, the locations $\text{round}((l_i^{\text{eq}})_N)$ and $\text{round}((l_j^{\text{eq}})_N)$ for each path should fall within the appropriate range, ensuring that the non-zero entries are distinct and do not overlap. Therefore, in order to prevent overlap between the positions of the non-zero entries in $\mathbf{H}_i$ and $\mathbf{H}_j$, it is necessary to ensure that there is no intersection between the ranges of $\text{round}((l_i^{\text{eq}})_N)$ and $\text{round}((l_j^{\text{eq}})_N)$. This condition as written in (4.2) guarantees that the non-zero entries in each row of the channel matrices are distinct and do not overlap.

$$\begin{aligned} &\{-k_{\max} - k_\nu + 2Nc_1 l_i, ..., k_{\max} + k_\nu + 2Nc_1 l_i\} \cap \\ &\{-k_{\max} - k_\nu + 2Nc_1 l_j, ..., k_{\max} + k_\nu + 2Nc_1 l_j\} = \emptyset. \end{aligned} \tag{4.2}$$

For paths with different delays, assuming $l_i < l_j$, satisfying (4.2) is equivalent to satisfying the following constraint

$$2Nc_1 > \frac{2(k_{\max} + k_\nu)}{l_j - l_i} \tag{4.3}$$

If there is sparsity in the time-domain impulse response of the channel, c_1 is set to

$$c_1 = \frac{2(k_{\max} + \xi_\nu) + 1}{2N \min_{i,j}(l_j - l_i)}, \tag{4.4}$$

for some $\xi_\nu \leq k_\nu$ whose value is discussed later on. In the case of no delay sparsity, then the minimum value of $l_j - l_i$ is one, then (4.4) simplify to

$$c_1 = \frac{2k'_{\max} + 1}{2N}, \tag{4.5}$$

where $k'_{\max} = k_{\max} + \xi_\nu$. Through ξ_ν, there is flexibility in setting c_1 and reducing pilot overhead (see Section 5.2) at the expense of $|\mathbf{H}_{\text{eff}}|$ no longer being strictly circulant. Moreover, the only remaining condition for the DAFT-domain impulse response to constitute a full delay-Doppler representation of the channel is to ensure that the non-zero entries of any two matrices $\mathbf{H}_{i_{\min}}$ and $\mathbf{H}_{i_{\max}}$ corresponding to paths $i_{\min}$ and $i_{\max}$ with delays $l_{i_{\min}} \triangleq \min_{i=1\cdots P} l_i$ and $l_{i_{\max}} \triangleq \max_{i=1\cdots P} l_i$, respectively, do not overlap due to the modular operation in (3.40). This overlapping never occurs if $2k'_{\max}l_{\max} + 2k'_{\max} + l_{\max} < N$. Since wireless channels are usually underspread (i.e., $l_{\max} \ll N$ and $k_{\max} \ll N$), this condition is satisfied even for moderate values of N.

With this parameter setting, channel paths with different delay values or different Doppler frequency shifts become separated in the DAFT domain, resulting in $\mathbf{H}_{\text{eff}}$ having the structure shown in Fig. 4.1. Thus, we get a delay-Doppler representation of the channel in the DAFT domain since the delay-Doppler profile can be determined from the positions of the non-zero entries in any row of $\mathbf{H}_{\text{eff}}$. This feature can be obtained by neither DAFT-OFDM (since by construction the effective channel matrix is made as close to diagonal as possible to reduce ICI), nor OCDM (since setting $c_1 = \frac{1}{2N}$, there may exist two paths $i \neq j$ such that the non-zero entries of $\mathbf{H}_i$ and $\mathbf{H}_j$ coincide under some delay-Doppler profiles of the channel). In the next section, we show that this unique feature of AFDM translates into being diversity order optimal in LTV channels.

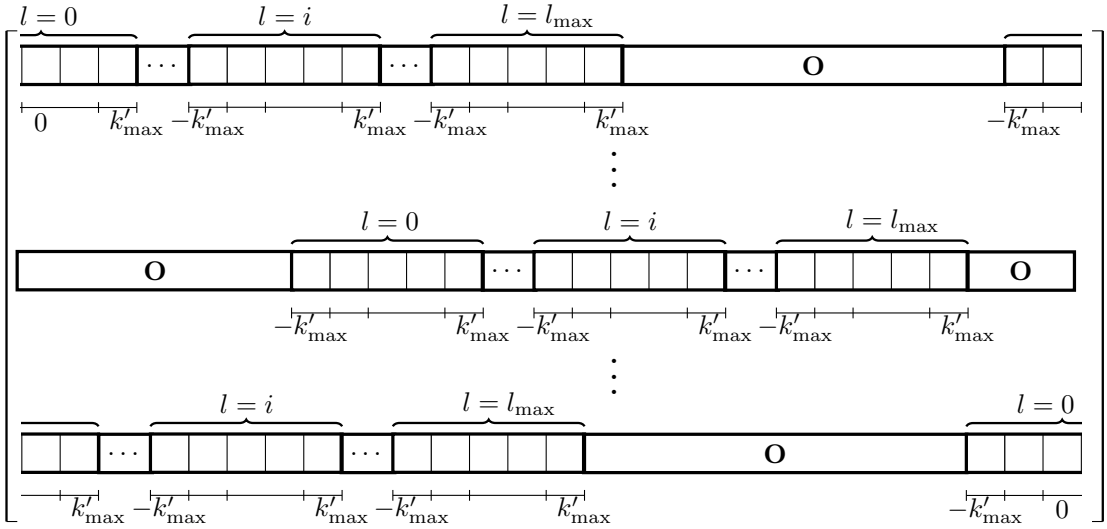

Figure 4.1: Structure of $\mathbf{H}_{\text{eff}}$ in AFDM

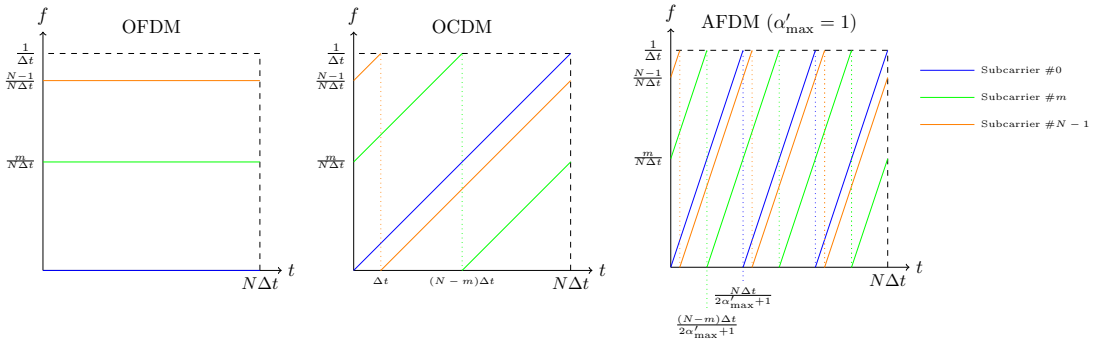

Figure 4.2: Time-frequency representation of OFDM, OCDM, and AFDM subcarriers

Also, this parameter setting results in the subcarriers $\phi_n(m) = \frac{1}{\sqrt{N}} \cdot e^{\imath 2\pi(c_1 n^2 + c_2 m^2 + nm/N)}$ having a time-frequency content that is distinct from all so-far existing waveforms. This time-frequency content is illustrated in Fig. 4.2 and is compared to that of OCDM and OFDM.

4.2 Diversity Analysis

In this section, our focus is on examining the diversity order of AFDM. The diversity order provides a qualitative measure of a waveform's performance by capturing the slope of its bit error rate (BER) performance curve in the high SNR regime. To establish a more precise definition, we refer to (4.16), which relies on the PEP. To simplify the analysis, we specifically present the diversity analysis in the context of integer Doppler shifts. However, it is important to note that Theorem 4.2.1 remains applicable to the case of fractional Doppler shifts as well. In order to proceed, we can rewrite (6.5) as

$$\mathbf{y} = \sum_{i=1}^{P} h_i \mathbf{H}_i \mathbf{x} + \widetilde{\mathbf{w}} = \mathbf{\Phi}(\mathbf{x})\mathbf{h} + \widetilde{\mathbf{w}}, \tag{4.6}$$

where $\mathbf{h} = [h_1, h_2, \ldots, h_P]$ denotes a $P \times 1$ vector, and $\mathbf{\Phi}(\mathbf{x})$ represents the concatenated matrix with dimensions $N \times P$

$$\mathbf{\Phi}(\mathbf{x}) = [\mathbf{H}_1\mathbf{x} \mid \ldots \mid \mathbf{H}_P\mathbf{x}]. \tag{4.7}$$

Our next step involves expressing the PEP. Initially, we normalize the elements of $\mathbf{x}$ to ensure that the average energy of $\mathbf{x}$ is equal to one. This normalization results in a SNR of $\frac{1}{N_0}$. Assuming perfect channel state information and ML detection at the receiver,the conditional PEP between $\mathbf{x}_m$ and $\mathbf{x}_n$, which corresponds to transmitting symbol $\mathbf{x}_m$ and making a decision in favor of $\mathbf{x}_n$ at the receiver, is given by

$$P(\mathbf{x}_m \to \mathbf{x}_n | \mathbf{h}, \mathbf{x}_m) = Q\left(\sqrt{\frac{\|\mathbf{\Phi}(\mathbf{x}_m - \mathbf{x}_n)\mathbf{h}\|^2}{2N_0}}\right). \tag{4.8}$$

By averaging over different channel realizations, the PEP can be expressed

$$P(\mathbf{x}_m \to \mathbf{x}_n) = \mathbb{E}_{\mathbf{h}}\left[Q\left(\sqrt{\frac{\|\mathbf{\Phi}(\boldsymbol{\delta}^{(m,n)})\mathbf{h}\|^2}{2N_0}}\right)\right], \tag{4.9}$$

where $\boldsymbol{\delta}^{(m,n)} = \mathbf{x}_m - \mathbf{x}_n$. To further analyze the term $|\mathbf{\Phi}(\boldsymbol{\delta}^{(m,n)})\mathbf{h}|^2$, we expand it as

$$\|\mathbf{\Phi}(\boldsymbol{\delta}^{(m,n)})\mathbf{h}\|^2 = \mathbf{h}^H \mathbf{\Phi}(\boldsymbol{\delta}^{(m,n)})^H \mathbf{\Phi}(\boldsymbol{\delta}^{(m,n)})\mathbf{h}. \tag{4.10}$$

The matrix $\mathbf{\Phi}(\boldsymbol{\delta}^{(m,n)})^H \mathbf{\Phi}(\boldsymbol{\delta}^{(m,n)})$ is Hermitian and can be diagonalized using a unitary transformation. Therefore, it can be written as

$$\mathbf{\Phi}(\boldsymbol{\delta}^{(m,n)})^H \mathbf{\Phi}(\boldsymbol{\delta}^{(m,n)}) = \mathbf{U}\mathbf{\Lambda}\mathbf{U}^H, \tag{4.11}$$

where $\mathbf{U}$ is a unitary matrix and $\mathbf{\Lambda} = \text{diag}(\lambda_1^2, \ldots, \lambda_P^2)$, with λ_i being the i-th singular value of $\mathbf{\Phi}(\boldsymbol{\delta}^{(m,n)})$. By substituting (4.11) into (4.10) and introducing the notation $\tilde{\mathbf{h}} = \mathbf{U}^H\mathbf{h}$, we can simplify Equation (4.10)

$$\|\mathbf{\Phi}(\boldsymbol{\delta}^{(m,n)})\mathbf{h}\|^2 = \tilde{\mathbf{h}}^H \mathbf{\Lambda} \tilde{\mathbf{h}} = \sum_{l=1}^{r} \lambda_l^2 |\tilde{h}[l]|^2, \tag{4.12}$$

where r represents the rank of the matrix $\mathbf{\Phi}(\boldsymbol{\delta}^{(m,n)})$.Now, PEP writes as

$$P(\mathbf{x}_m \to \mathbf{x}_n) = \mathbb{E}_{\mathbf{h}} \left[Q\left(\sqrt{\frac{\sum_{l=1}^{r} \lambda_l^2 |\tilde{h}[l]|^2}{2N_0}} \right) \right]. \tag{4.13}$$

with the assumption that the h_i values are independently and identically distributed (iid) with a distribution $\mathcal{CN}(0, 1/P)$, $\tilde{\mathbf{h}}$ has the same distribution as $\mathbf{h}$ due to the unitary property of $\mathbf{U}$. Using the upper bound derived in [30], we can establish an upper bound for the PEP as

$$P(\mathbf{x}_m \to \mathbf{x}_n) \leq \prod_{l=1}^{r} \frac{1}{1 + \dfrac{\lambda_l^2}{4PN_0}}. \tag{4.14}$$

At high SNR, (4.14) becomes

$$P(\mathbf{x}_m \to \mathbf{x}_n) \leq \frac{1}{\frac{1}{{N_0}^r} \displaystyle\prod_{l=1}^{r} \frac{\lambda_l^2}{4P}}. \tag{4.15}$$

We can see from (4.15) that the exponent of the SNR term, $\frac{1}{N_0}$, is r, which is equal to the rank of the matrix $\mathbf{\Phi}(\boldsymbol{\delta}^{(m,n)})$. The overall BER is dominated by the PEP with the minimum value of r, for all $m, n, m \neq n$. Hence, the diversity order of AFDM is given by

$$\rho = \min_{m,n \ m \neq n} \operatorname{rank}(\mathbf{\Phi}(\boldsymbol{\delta}^{(m,n)})). \tag{4.16}$$

First, we show that for DAFT-based multi-carrier schemes, a necessary (but not sufficient) condition to achieve the optimal diversity order, i.e., $\rho = P$, is

$$\forall i, j \in [1, \cdots, P], \quad \operatorname{round}((l_i^{\mathrm{eq}})_N) \neq \operatorname{round}((l_j^{\mathrm{eq}})_N). \tag{4.17}$$

The above condition can hold for AFDM, but not for OCDM and DAFT-OFDM. For that sake, we assume that there exist channel paths i and j such that the locations of their corresponding non-zero elements in the channel matrix are the same, i.e., $\operatorname{round}((l_i^{\mathrm{eq}})_N) = \operatorname{round}((l_j^{\mathrm{eq}})_N)$. We then show that the optimal diversity order cannot be achieved under this assumption. Indeed, for the optimal diversity order, the matrix in (4.18) writes as

$$\begin{bmatrix} H_i[1, q_0]\delta[q_0] & H_j[1, q_0]\delta[q_0] \\ H_i[2, (q_0+1)_N]\delta[(q_0+1)_N] & H_j[2, (q_0+1)_N]\delta[(q_0+1)_N] \\ \vdots & \vdots \\ H_i[N, (q_0+N-1)_N]\delta[(q_0+N-1)_N] & H_j[N, (q_0+N-1)_N]\delta[(q_0+N-1)_N] \end{bmatrix}, \tag{4.18}$$

where $q_0 = \operatorname{round}((l_i^{\mathrm{eq}})_N) = \operatorname{round}((l_j^{\mathrm{eq}})_N)$, composed of the columns i and j of $\mathbf{\Phi}(\boldsymbol{\delta})$ should be of rank 2 for all possible values of $\boldsymbol{\delta}$. However, when $\boldsymbol{\delta}$ is such that it has a single non-zero element, the two columns of the matrix in (4.18) are dependent, hence the rank of this matrix cannot be 2. Consequently, the rank of $\mathbf{\Phi}(\boldsymbol{\delta})$ cannot be P and the condition in (4.17) is thus necessary for the optimal diversity order. The second condition involves tuning the value of c_2 in order to make the matrix $\mathbf{\Phi}(\boldsymbol{\delta})$ full rank. This requirement ensures that the matrix $\mathbf{\Phi}(\boldsymbol{\delta})$ has linearly independent columns. By

satisfying these conditions, we can establish the following theorem, which guarantees that AFDM achieves the optimal diversity order.

Theorem 4.2.1. *For a linear time-varying channel with a maximum delay $l_{\max}$ and maximum normalized Doppler shift $k_{\max}$, AFDM with c_1 satisfying (4.5) and c_2 being an arbitrary irrational number or a rational number sufficiently smaller than $\frac{1}{2N}$ achieves the optimal diversity order ($\rho = P$) if*

$$2k_{\max} + l_{\max} + 2k_{\max}l_{\max} < N. \tag{4.19}$$

Proof. To prove Theorem 4.2.1, we show that when (4.5) and (4.19) hold, there exist values of c_2 such that the rank of $\mathbf{\Phi}(\boldsymbol{\delta})$ is equal to P i.e., such that the P columns of $\mathbf{\Phi}(\boldsymbol{\delta})$ are linearly independent. Therefore, considering the $\mathbf{\Phi}(\boldsymbol{\delta})$ for a P-path channel

$$\begin{aligned}\mathbf{\Phi}(\boldsymbol{\delta}) &= [\mathbf{H}_1\boldsymbol{\delta} \mid \ldots \mid \mathbf{H}_P\boldsymbol{\delta}] \\ &= \begin{bmatrix} H_{\text{eff}}[0,q_1]\delta[q_1] & \cdots & H_{\text{eff}}[0,q_P]\delta[q_P] \\ H_{\text{eff}}[1,(q_1+1)_N]\delta[(q_1+1)_N] & \cdots & H_{\text{eff}}[1,(q_P+1)_N]\delta_{(q_P+1)_N} \\ \vdots & \ddots & \vdots \\ H_{\text{eff}}[N-1,(q_1+N-1)_N]\delta[(q_1+N-1)_N] & \cdots & H_{\text{eff}}[N-1,(q_P+N-1)_N]\delta[(q_P+N-1)_N] \end{bmatrix},\end{aligned} \tag{4.20}$$

where $q_i = \text{round}((l_i^{\text{eq}})_N)$, we should show that

$$\beta_1\mathbf{H}_1\boldsymbol{\delta} + \beta_2\mathbf{H}_2\boldsymbol{\delta} + \cdots + \beta_P\mathbf{H}_P\boldsymbol{\delta} = \mathbf{0} \rightarrow \beta_1 = \beta_2 = \cdots = \beta_P = 0 \tag{4.21}$$

which will be done with proof by contradiction. Assume that there is at least one $\beta_i \neq 0$ and still we have $\beta_1\mathbf{H}_1\boldsymbol{\delta}+\beta_2\mathbf{H}_2\boldsymbol{\delta}+\cdots+\beta_P\mathbf{H}_P\boldsymbol{\delta} = \mathbf{0}$. Without loss of generality we assume $\beta_1 \neq 0$. By dividing both sides of the vector equality in (4.21) by β_1 and considering the first entry of the resulting vector, we have

$$\delta[q_1] = -\frac{H_{\text{eff}}[0,q_2]}{H_{\text{eff}}[0,q_1]}\frac{\beta_2}{\beta_1}\delta[q_2] - \cdots - \frac{H_{\text{eff}}[0,q_P]}{H_{\text{eff}}[0,q_1]}\frac{\beta_P}{\beta_1}\delta[q_P]. \tag{4.22}$$

In addition, by taking to account the $\mathbf{H}_{\text{eff}}$ expression, we have

$$\frac{H_{\text{eff}}[0,q_i]}{H_{\text{eff}}[0,q_j]} = e^{\imath 2\pi c_2(q_i^2-q_j^2)} e^{\imath \frac{2\pi}{N}(Nc_1(l_i^2-l_j^2)-q_i l_i+q_j l_j)}. \tag{4.23}$$

Now we can rewrite (4.22) using (4.23)

$$\delta[q_1] = e^{-\imath 2\pi c_2 q_1^2} e^{\imath \frac{2\pi}{N}(Nc_1(-l_1^2+q_1 l_1))} \left[\sum_{i=2}^{P} e^{\imath 2\pi c_2 q_i^2} e^{\imath \frac{2\pi}{N}(Nc_1 l_i^2 - q_i l_i)} \beta_i' \delta[q_i]\right] \tag{4.24}$$

where $\beta_i' = \frac{-\beta_i}{\beta_1}$. Note that $\boldsymbol{\delta} \in \mathbb{Z}[j]^{N\times 1}$, therefore since $\delta[q_1] \in \mathbb{Z}[j]$ then the right hand side of (4.24) should be in $\mathbb{Z}[j]$ to have the equality. On the other hand by choosing an irrational number for c_2, $e^{\imath 2\pi c_2 q_i^2}$ will be an irrational number and since (4.24) should hold for different values of δ, the effect of c_2 should be removed from this equation. We can remove the terms containing c_2 by choosing

$$\beta_i' = e^{\imath 2\pi c_2 q_1^2} e^{-\imath 2\pi c_2 q_i^2} \mu_i, i = 2, \cdots, P \tag{4.25}$$

where μ_is do not contain c_2 in their phases. Now in order to have (4.24) equality, at least another β_i should be non-zero. Again without loss of generality, assume the non-zero one is β_2. Dividing both sides of the vector equality in (4.21) with β_2 and considering the second entry of the resulting vector we get

$$\begin{aligned}\delta[(q_2+1)_N] = {} & e^{-\imath 2\pi c_2 (q_2+1)_N^2} e^{\imath \frac{2\pi}{N}(Nc_1(-l_2^2+(q_2+1)_N l_2))} \\ & \times \left[\sum_{i=1, i\neq 2}^{P} e^{\imath 2\pi c_2 (q_i+1)_N^2} e^{\imath \frac{2\pi}{N}(Nc_1 l_i^2 - (q_i+1)_N l_i)} \beta_i'' \delta[(q_i+1)_N]\right],\end{aligned} \tag{4.26}$$

where $\beta_i'' = \frac{-\beta_i}{\beta_2}$. With the same explanation, β_i''s are

$$\beta_i'' = e^{\imath 2\pi c_2 (q_2+1)_N^2} e^{-\imath 2\pi c_2 (q_i+1)_N^2} \mu_i', i = 1, \cdots, P, i \neq 2. \tag{4.27}$$

Putting (4.25) and (4.27) together shows

$$\beta_2' = \frac{1}{\beta_1''} \tag{4.28}$$

which leads to

$$e^{\imath 2\pi c_2\left(q_2^2-(q_2+1)_N^2+q_1^2-(q_1+1)_N^2\right)}\mu_2\mu_1' = 1. \tag{4.29}$$

On one hand since $q_1 \neq q_2$, $q_2^2-(q_2+1)_N^2+q_1^2-(q_1+1)_N^2$ cannot be zero and on the other hand we know that μ_i and μ_i' do not contain c_2 in their phases, therefore c_2 effect in the phase cannot be removed and the left hand side of the equation (4.29) is an irrational number while the right one is integer. Our first assumption is thus wrong and $\beta_1 = \cdots = \beta_P = 0$ which means the P columns of $\mathbf{\Phi}(\boldsymbol{\delta})$ are linearly independent, i.e., the rank of $\mathbf{\Phi}(\boldsymbol{\delta})$ is P, and AFDM achieves full diversity. □

4.3 Simulation Results

In this section, we provide simulation results to assess the performance of AFDM. In all simulations, the complex gains h_i are generated as independent complex Gaussian random variables with zero mean and $1/P$ variance. The carrier frequency is 4 GHz. BER values are obtained using 10^6 different channel realizations.

Fig. 4.3a shows the simulated BER performance of AFDM for different channels with $N = 16$ and BPSK using the ML detection. We consider three different channels with different numbers of paths, namely a 2-path, a 3-path , and a 4-path channel. The maximum delay spread (in terms of integer taps) is set to be 2 ($l_{\max} = 1$), 3 ($l_{\max} = 2$) and 4 ($l_{\max} = 3$), respectively. The duration between two successive delay taps is approximately 41.6 μs. The maximum Doppler shift is considered $k_{\max} = 1$, which corresponds to a maximum speed of 405 km/h. We observe that for each channel, AFDM achieves the optimal diversity order of the channel. Note that the plots of $s_1(SNR)^{-2}$, $s_2(SNR)^{-3}$ and $s_3(SNR)^{-4}$ are only used to identify the slope of the curves and do not

Table 4.1: Excess complexity of OTFS and AFDM transmitters over OFDM transmitter.

Waveform	Complex Multiplication
OTFS	$(N/2)\log_2 N$
AFDM	$2N$

represent an upper bound.

Before proceeding further, we recall that in OTFS the time–frequency signal plane is sampled at intervals T_{OTFS} (seconds) and Δf_{OTFS} (Hz), respectively to obtain a grid as

$$\begin{aligned}\Lambda_{\mathrm{OTFS}} = \{&(nT_{\mathrm{OTFS}}, m\Delta f_{\mathrm{OTFS}}) \\ &, n = 0, \cdots, N_{\mathrm{OTFS}} - 1, m = 0, \cdots, M_{\mathrm{OTFS}} - 1\},\end{aligned} \tag{4.30}$$

and modulated time–frequency samples $X[n, m], n = 0, ..., N_{\mathrm{OTFS}} - 1, m = 0, ..., M_{\mathrm{OTFS}} - 1$ are transmitted over an OTFS frame with duration $T_{f\_\mathrm{OTFS}} = N_{\mathrm{OTFS}} T_{\mathrm{OTFS}}$ and occupy a bandwidth $B_{\mathrm{OTFS}} = M_{\mathrm{OTFS}}\Delta f_{\mathrm{OTFS}}$. In order to compare the performance of AFDM against OTFS, we assume $N = M_{\mathrm{OTFS}} N_{\mathrm{OTFS}}$ so that the AFDM and OTFS frames occupy the same time-frequency resources. We also compare the computational complexity of OTFS with AFDM. In the symplectic finite Fourier transform (SFFT) implementation of OTFS [51], the transmitter includes, in addition to OFDM modulation, an $\mathbf{F}^H_{M_{\mathrm{OTFS}}} \otimes \mathbf{F}_{N_{\mathrm{OTFS}}}$ step whose complexity is equivalent to $M_{\mathrm{OTFS}} N_{\mathrm{OTFS}}$-sized ($N$-sized) FFT, i.e., $(N/2)\log_2 N$ complex multiplications. For AFDM, there are two additional phase rotations, which require 2 additional complex multiplications per symbol compared to the transmitter of an OFDM system, which means the additional complexity is $2N$ complex multiplications. Table 4.1 summarizes this complexity comparison[1].

Fig. 4.3b shows the BER performance of AFDM, OFDM, OCDM, and OTFS. For the DAFT-based schemes, we generate the frames with $N = 16$. OTFS frame is generated with $N_{\mathrm{OTFS}} = 4$ and $M_{\mathrm{OTFS}} = 4$. The maximum delay spread is set to be $l_{\max} = 2$ and

[1]We compare AFDM only with SFFT-based OTFS, since the DZT-based OTFS [52] has limitations in terms of spectral shaping and compatibility with OFDM transceivers.

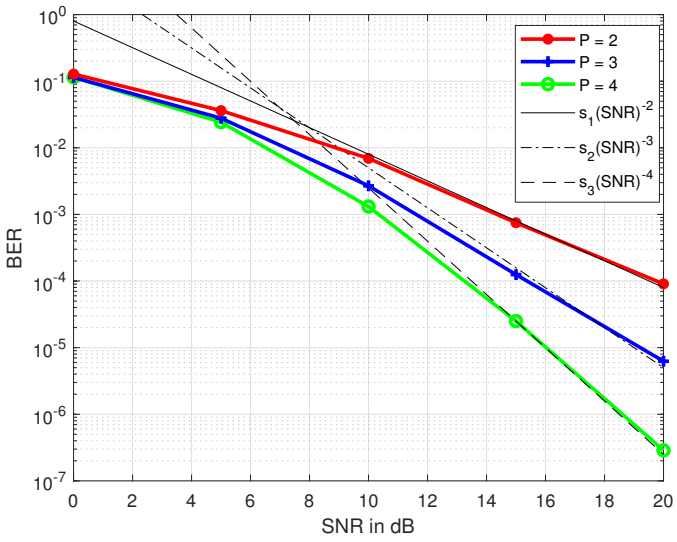

(a) BER performance of AFDM with different number of paths for $N = 16$.

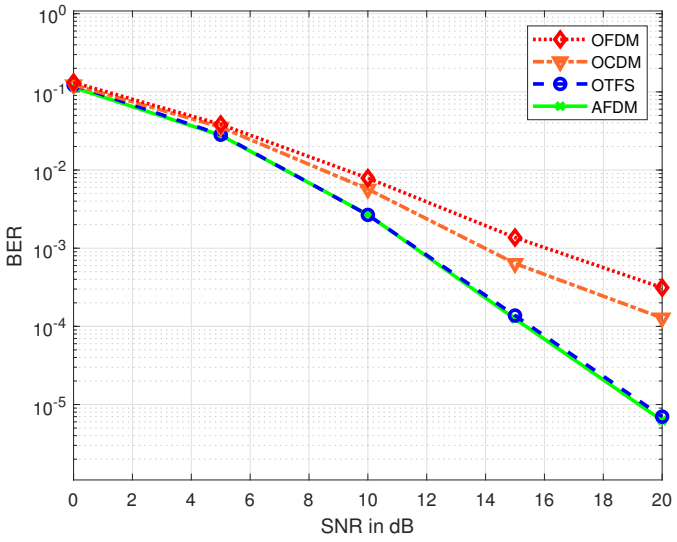

(b) BER performance of OFDM, OCDM, OTFS and AFDM in a three-path channel for $N = 16$, $N_{\text{OTFS}} = 4$ and $M_{\text{OTFS}} = 4$.

Figure 4.3: BER performance using BPSK in LTV channels using ML detection

the maximum Doppler shift is $k_{\max} = 1$. The delay shifts are fixed and Jakes Doppler spectrum is considered for each channel realization, i.e, the Doppler shifts are varying and the Doppler shift of each path is generated using $k_i = k_{\max} cos(\theta_i)$, where θ_i is uniformly distributed over $[-\pi, \pi]$. Expectedly, OFDM has the worse performance as it cannot separate the paths. The performance of OCDM depends on the delay-Doppler profile of the channel. OCDM performs poorly and has the same diversity (one) as OFDM, due to the possible destructive addition of the two overlapping paths. The reason why OCDM has better performance than OFDM is related to its better path separation capabilities than OFDM. The proposed AFDM achieves the optimal diversity order, mainly due to path separation by tuning c_1 and setting c_2 to be an arbitrary irrational number or a rational number sufficiently smaller than $\frac{1}{2N}$. We also observe that AFDM has the same BER performance as OTFS. The reason AFDM and OTFS have (almost) the same BER performance is because AFDM and OTFS both achieve a full delay Doppler representation of the channel, i.e., of the paths of the effective channel (in the DAFT domain for AFDM, in the delay-Doppler domain for OTFS) each corresponds to one delay tap-Doppler bin pair of the wireless propagation channel and each has the same path gain under both AFDM and OTFS (strict equality holds at least in the case of integer valued Doppler shifts). As mentioned earlier, this feature enables AFDM to achieve the optimal diversity order of the LTV channels. While OTFS does not strictly speaking achieve the diversity order of the LTV channel, the number of codeword pairs with PEP that decays with slope 1 with respect to the SNR is too small to have an effect on the overall PEP in the intermediate SNR regime [23] .

In the previous figures, small N values are assumed along with ML detection to show the diversity order of AFDM. In the following figures, we consider a more practical configuration with QPSK, $N = 256$ for the DAFT-based schemes and $N_{\text{OTFS}} = 16$, $M_{\text{OTFS}} = 16$ for the OTFS. We consider a 3-path channel. The maximum Doppler shift is $k_{\max} = 2$, which corresponds to a speed of 540 km/h, and the Doppler shift of each

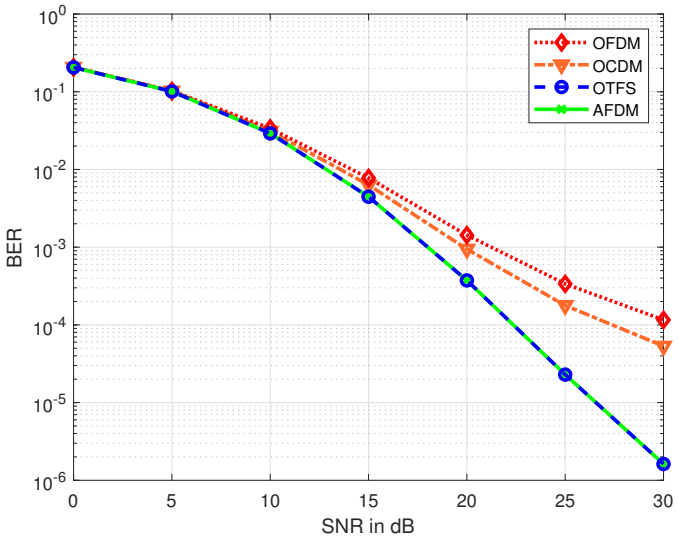

Figure 4.4: BER performance of OFDM, OCDM, OTFS and AFDM using MMSE detection.

path is generated using Jakes Doppler spectrum. The maximum delay spread is set to be $l_{\max} = 2$. Fig. 5.7a shows the BER performance of the DAFT-based schemes and OTFS. All results are obtained with LMMSE detection at the receiver. We observe that AFDM outperforms OFDM and OCDM, while having identical performance with OTFS. However, when channel estimation is taken into account, the pilot overhead of OTFS is twice that of AFDM due to the 2D structure of its underlying transform as it is shown in detail in the next chapter.

4.4 Conclusion

Throughout this chapter, we delved deeply into the capabilities of AFDM in relation to the full diversity order of LTV channels. Our journey began by adjusting the parameters of AFDM to ensure it identifies every path, regardless of the differences in their delays or Doppler shifts. This crucial adjustment laid the groundwork for achieving a full delay-Doppler representation of the channel. From there, we transitioned to an analytical phase, providing the proof that, with these settings, AFDM achieves the full diversity

of the LTV channels. We underscored the significance of these parameters in ensuring optimal performance. To round off our discussion, we presented simulation results as the final touch, underscoring AFDM's practical efficiency in leveraging the full diversity of LTV channels.

Chapter 5

Detection and Channel Estimation

In communication systems, detection and channel estimation serve as two fundamental processes that ensure efficient data transmission. While ML detection is valuable for understanding diversity analysis, its practical implementation in real-world systems is constrained by its high complexity. On the other hand, the receiver's ability to accurately decode transmitted signals heavily relies on its understanding of the channel characteristics. This understanding is obtained through the channel estimation process. Given the varying nature of communication channels, impacted by aspects like fading and interference, a receiver's capability to capture and adjust to these changes is vital for optimal performance. For the receiver, precise channel knowledge allows for a more efficient detection process, reducing the probability of errors and enhancing overall system performance.

In this chapter,we propose two low complexity detection algorithms for AFDM taking advantage of its inherent channel sparsity. The first is a low complexity MMSE detector based on LDL factorization [53]. The second is a low complexity iterative DFE based on weighted MRC of the channel impaired input symbols received from different paths. We also propose an embedded pilot-aided channel estimation scheme for AFDM, in which both channel estimation and data detection are performed within the same AFDM frame.

5.1 Detection

In this section, we introduces two low-complexity detection methods. The foundational step of our approach is the insertion of null symbols. This allows us to approximate the truncated portion of $\mathbf{H}_{\text{eff}}$ as a band matrix, leading to a simplified system. Moreover, as illustrated in Figure 5.1, the need for a modular operation is eliminated. Note that these null symbols serve a dual purpose in enhancing the system's performance. They not only facilitate our proposed detection algorithms but also assist in embedded pilot-aided channel estimation without incurring extra overhead. Due to the structure of $\mathbf{H}_{\text{eff}}$, the number of the null guard symbols should be greater than

$$Q \triangleq (l_{\max}+1)(2(k_{\max}+\xi_\nu)+1)-1. \tag{5.1}$$

Taking into account the zero padding, the vector of DAFT domain received samples writes as

$$\mathbf{y} = \underline{\mathbf{H}}_{\text{eff}}\underline{\mathbf{x}} + \underline{\widetilde{\mathbf{w}}} \tag{5.2}$$

where $\underline{\mathbf{x}}$ and $\underline{\mathbf{H}}_{\text{eff}}$ are the truncated parts of $\mathbf{x}$ and $\mathbf{H}_{\text{eff}}$, respectively (see Figure 5.1). They can be expressed using the matrix $\mathbf{T} = [\mathbf{I}_N]_{Q-(k_{\max}+\xi_\nu):N-(k_{\max}+\xi_\nu)-1,:}$ as $\underline{\mathbf{x}} = \mathbf{T}\mathbf{x}$ and $\underline{\mathbf{H}}_{\text{eff}} = \mathbf{H}_{\text{eff}}\mathbf{T}^H$. Using LMMSE equalization for (5.2) requires $\mathcal{O}(N^3)$ flops, which can be prohibitive for large N. We thus propose two detectors with lower complexity. The first is a low-complexity LMMSE based on a band approximation of $\underline{\mathbf{H}}_{\text{eff}}$. The second is a weighted MRC-based DFE exploiting the sparse representation of the communication channel provided by AFDM.

5.1.1 Low complexity MMSE detection

To recover the data symbols $\underline{\mathbf{x}}$, the following MMSE equalization based on (5.2) is used

$$\hat{\underline{\mathbf{x}}} = \underline{\mathbf{H}}_{\text{eff}}^H(\underline{\mathbf{H}}_{\text{eff}}\underline{\mathbf{H}}_{\text{eff}}^H + N_0\mathbf{I}_N)^\dagger\mathbf{y}. \tag{5.3}$$

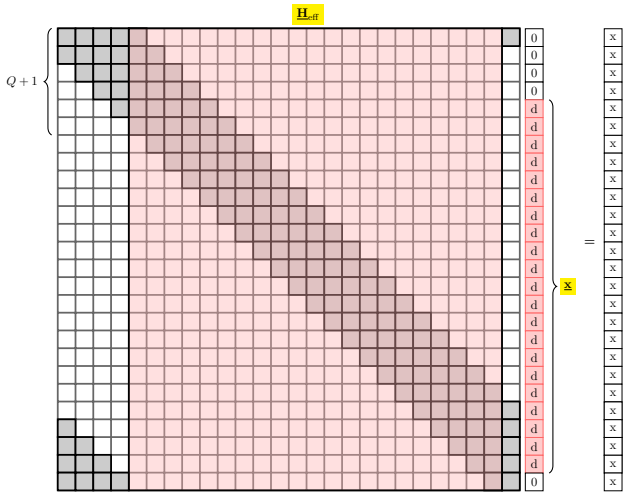

Figure 5.1: Truncated parts of $\mathbf{x}$ and $\mathbf{H}_{\text{eff}}$

Algorithm 5.1.1 Low complexity MMSE detection

Construct the matrix $\underline{\mathbf{H}}_{\text{eff}} = \mathbf{H}_{\text{eff}}\mathbf{T}^H$
Construct the band matrix $\mathbf{M} = \underline{\mathbf{H}}_{\text{eff}}\underline{\mathbf{H}}_{\text{eff}}^H + N_0\mathbf{I}_N$
Compute the LDL factorization of $\mathbf{M} = \mathbf{L}\mathbf{D}\mathbf{L}^H$ where $\mathbf{L}$ is a lower triangular matrix with Q sub diagonals and $\mathbf{D}$ is a diagonal matrix
Solve the triangular system $\mathbf{L}\mathbf{f} = \mathbf{y}$
Solve the diagonal system $\mathbf{D}\mathbf{g} = \mathbf{f}$
Solve the triangular system $\mathbf{L}^H\mathbf{d} = \mathbf{g}$
Calculate $\hat{\underline{\mathbf{x}}} = \underline{\mathbf{H}}_{\text{eff}}^H\mathbf{d}$

Although (5.3) involves matrix inversion, the matrix $\mathbf{M} = \underline{\mathbf{H}}_{\text{eff}}\underline{\mathbf{H}}_{\text{eff}}^H + N_0\mathbf{I}_N$ is a Hermitian band matrix with lower and upper bandwidth Q. Thus, $\mathbf{M}^{-1}$ can be computed using LDL factorization. Algorithm 5.1.1 can be performed to efficiently equalize the received signal.

The computational cost of the proposed detection algorithm is evaluated in terms of complex additions (CAs), complex multiplications (CMs) and complex divisions (CDs). The first step does not need any complex operation since $\underline{\mathbf{H}}_{\text{eff}}$ is truncated from $\mathbf{H}_{\text{eff}}$. In step 2, every element of $\underline{\mathbf{H}}_{\text{eff}}\underline{\mathbf{H}}_{\text{eff}}^H$ requires at most $Q+1$ CMs and Q CAs. Considering that $\underline{\mathbf{H}}_{\text{eff}}\underline{\mathbf{H}}_{\text{eff}}^H$ is Hermitian and neglecting some small terms in the complexity expression, step 2 requires $\frac{1}{2}(Q^2+3Q+2)N$ CMs and $\frac{1}{2}(Q^2+Q+2)N$ CAs. Similar to [54], step 3, the LDL factorization, requires $\frac{1}{2}(Q^2+3Q)N$ CMs, $\frac{1}{2}(Q^2+Q)N$ CAs, and QN CDs.

Steps 4 and 6 can be solved by band forward and backward substitutions [55] and each of them has QN CMs and QN CAs. Step 5 can be solved using N CDs since $\mathbf{D}$ is a diagonal matrix and the last step requires $(Q+1)N$ CMs and QN CAs. Thus, the whole algorithm requires $(Q^2+6Q+2)N$ CMs, $(Q^2+4Q+1)N$ CAs and $(Q+1)N$ CDs, which amounts to $(2Q^2+11Q+4)N$ complex operations.

5.1.2 Low-Complexity weighted MRC-based DFE detection

As shown in Figure 5.1, $\underline{\mathbf{H}}_{\text{eff}}$ has L non-zero entries per column where $L = P$ for the integer Doppler shift case and $L = (2\xi_\nu+1)P$ for fractional Doppler shift case with $L \leq Q$ in both cases. Each of these non-zero entries of a column of $\underline{\mathbf{H}}_{\text{eff}}$ provides a copy of the data symbol corresponding to the index of this column. We propose a detection scheme with which each data symbol is detected from a weighted MRC of its L channel-impaired received copies. Figure 5.2 shows an example of this detector for AFDM with $N = 8$ and a 3-path channel with $Q = 2$. The proposed detector is iterative, wherein each iteration, the estimated inter symbol interference is canceled in the branches selected for the combining. Considering the structure of $\underline{\mathbf{H}}_{\text{eff}}$, it can be seen that each received symbol $y[k]$ is given by

$$y[k] = \sum_{i=0}^{L-1} \underline{H}_{\text{eff}}[k, p_k^i] x[p_k^i] \tag{5.4}$$

where p_k^i is the column index of the i-th path coefficient in row k of matrix $\underline{\mathbf{H}}_{\text{eff}}$. Let b_k^i be the channel impaired input symbol $x[k]$ in the received samples $y[q_k^i]$ after cancelling the interference from other input symbols, where q_k^i is the row index of the i-th path coefficient in column k of matrix $\underline{\mathbf{H}}_{\text{eff}}$. In each iteration, assuming estimates of the input symbols $x[k]$ are available either from the current iteration (for $p^j_{q_k^i} < k, \quad j = 0, ..., L-1$) or previous iteration (for $p^j_{q_k^i} > k, \quad j = 0, ..., L-1$), b_k^i can be written as

$$b_k^i = y[q_k^i] - \sum_{p^j_{q_k^i} < k} \underline{H}_{\text{eff}}[q_k^i, p^j_{q_k^i}] \hat{x}[p^j_{q_k^i}]^{(n)} - \sum_{p^j_{q_k^i} > k} \underline{H}_{\text{eff}}[q_k^i, p^j_{q_k^i}] \hat{x}[p^j_{q_k^i}]^{(n-1)}. \tag{5.5}$$

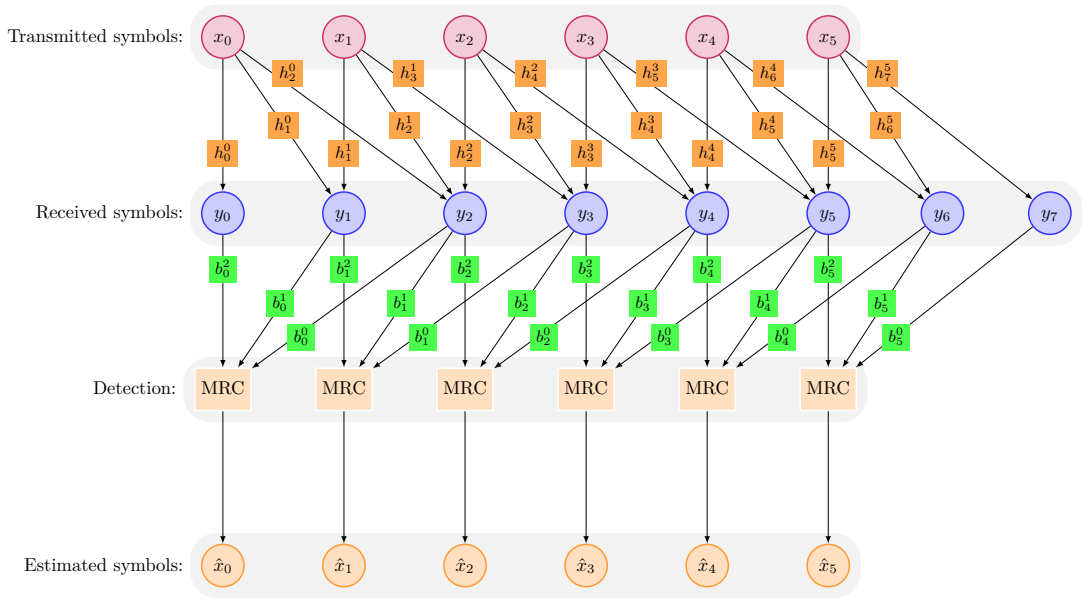

Figure 5.2: Weighted MRC operation for $N = 8$ with a 3-path channel with $Q = 2$.

Where superscript (n) denotes the n-th iteration. It can be seen that for each symbol x_k, we need to compute L scalars. This operation has the complexity order of $\mathcal{O}(L^2)$. However, When computing b_k^i for all symbols k there are some redundant operations involved that can be avoided by instead computing b_k^ias follows

$$b_k^i = \Delta y[q_k^i]^{(n)} + \underline{H}_{\text{eff}}[q_k^i, k]\hat{x}[k]^{(n-1)}. \tag{5.6}$$

Here, $\Delta y_{q_k(i)}^{(n)}$ is the residual error remaining while reconstructing the received symbols and is given by

$$\Delta y[q_k^i]^{(n)} = y[q_k^i] - \sum_{p_{q_k^i}^j < k} \underline{H}_{\text{eff}}[q_k^i, p_{q_k^i}^j]\hat{x}[p_{q_k^i}^j]^{(n)} - \sum_{p_{q_k^i}^j \geq k} \underline{H}_{\text{eff}}[q_k^i, p_{q_k^i}^j]\hat{x}[p_{q_k^i}^j]^{(n-1)}. \tag{5.7}$$

Define $g_k^{(n)}$ and d as

$$g_k^{(n)} \triangleq \sum_{i=0}^{L-1} \underline{H}_{\text{eff}}^*(q_k^i, k)b_k^i = \sum_{i=0}^{L-1} \underline{H}_{\text{eff}}^*(q_k^i, k)\Delta y[q_k^i]^{(n)} + dx[k]^{(n-1)}, \tag{5.8}$$

$$d \triangleq \sum_{i=0}^{L-1} |\underline{H}_{\text{eff}}(q_k^i, k)|^2. \tag{5.9}$$

It should be noted that since $|\mathbf{H}_{\text{eff}}|$ is a circulant matrix, the value of d is independent of k and needs to be computed only once. We now define γ as the SNR. Instead of directly using $g_k^{(n)}/d$ as the estimate of x_k (which would have amounted to using the MRC criterion), we define the symbol estimate as

$$\hat{x}[k]^{(n)} = c_k^{(n)} \tag{5.10}$$

$$c_k^{(n)} \triangleq \frac{g_k^{(n)}}{d + \gamma^{-1}} = \frac{1}{d + \gamma^{-1}} \sum_{i=0}^{L-1} \underline{H}_{\text{eff}}^*[q_k^i, k] \Delta y[q_k^i]^{(n)} + \frac{d}{d + \gamma^{-1}} \hat{x}[k]^{(n-1)}, \tag{5.11}$$

We later show in section 11 that this weighting of $g_k^{(n)}$ while computing $\hat{x}_k^{(n)}$ guarantees that the iterative detection algorithm converges to the LMMSE estimate of the symbols vector $\underline{\mathbf{x}}$. In each iteration, after estimation of each symbol $x[k]^{(n)}$, the values of $\Delta y[q_k^i]^{(n)}$ for $i = 0, \ldots, L-1$ need to be updated using

$$\Delta y[q_k^i]^{(n)} = \Delta y[q_k^i]^{(n)} - \underline{H}_{\text{eff}}^*(q_k^i, k)(x[k]^{(n)} - x[k]^{(n-1)}). \tag{5.12}$$

Once all the symbols are estimated, they are used for interference cancellation in the next iteration. The algorithm continues until the maximum number of iterations (n_{iter}) is reached or the updated input symbol vector is close enough (less than ϵ) to the previous one as summarized in Algorithm 5.1.2.

Computing the complexity of Algorithm 5.1.2 is straightforward as it has only scalar operations. Step 3 to step 8 requires $2L$ CMs, $3L + 1$ CAs and 1 CD. Therefore, its total complexity is $n_{\text{iter}}(5L + 1)(N - Q)$.

Algorithm 5.1.2 Weighted MRC-based DFE detection

Data: $\underline{\mathbf{H}}_{\text{eff}}$, d, $\mathbf{y}$, $\hat{\mathbf{x}}^{(0)} = \mathbf{0}$, $\Delta\mathbf{y}^{(0)} = \mathbf{y}$

for *n = 1 : n_{iter}* **do**
  for *k = 0 : N-Q-1* **do**
    $g_k^{(n)} = \sum_{i=0}^{L-1} \underline{H}_{\text{eff}}^*(q_k^i, k)\Delta y[q_k^i]^{(n)} + dx[k]^{(n-1)}$
    $c_k^{(n)} = \frac{g_k^{(n)}}{d+\gamma^{-1}}$
    $\hat{x}[k]^{(n)} = c_k^{(n)}$
    for *i = 0 : L-1* **do**
      $\Delta y[q_k^i]^{(n)} = \Delta y[q_k^i]^{(n)} - \underline{H}_{\text{eff}}^*(q_k^i, k)(x[k]^{(n)} - x[k]^{(n-1)})$
    end
  end
  if $||\hat{\mathbf{x}}^{(n)} - \hat{\mathbf{x}}^{(n-1)}|| < \epsilon$ **then** EXIT;
end

Convergence

In this part, we analyze the detector convergence using the properties of iterative methods for linear systems. To this end, Algorithm 5.1.2 can be expressed in the matrix form as

$$\hat{\mathbf{x}}^{(n)} = \frac{d}{\gamma^{-1}+d}\hat{\mathbf{x}}^{(n-1)} + \frac{1}{\gamma^{-1}+d}(\underline{\mathbf{H}}_{\text{eff}}^H\mathbf{y} - \mathbf{L}\hat{\mathbf{x}}^{(n)} - (\mathbf{L}^H + \mathbf{D})\hat{\mathbf{x}}^{(n-1)}), \tag{5.13}$$

where $\mathbf{D} = d\mathbf{I}$, $\mathbf{L}$ and $\mathbf{L}^H$ are the matrices containing diagonal elements, strictly lower and upper triangular parts of the Hermitian matrix $\underline{\mathbf{H}}_{\text{eff}}^H\underline{\mathbf{H}}_{\text{eff}}$, respectively. Equation (5.13) can be rewritten in the form

$$\hat{\mathbf{x}}^{(n)} = -\mathbf{S}^{-1}(\mathbf{R} - \mathbf{S})\hat{\mathbf{x}}^{(n-1)} + \mathbf{M}^{-1}\mathbf{b}, \tag{5.14}$$

where

$$\mathbf{S} = (\gamma^{-1} + d)\mathbf{I} + \mathbf{L} \tag{5.15}$$

$$\mathbf{R} = \underline{\mathbf{H}}_{\text{eff}}^H\underline{\mathbf{H}}_{\text{eff}} + \gamma^{-1}\mathbf{I} \tag{5.16}$$

$$\mathbf{b} = \underline{\mathbf{H}}_{\text{eff}}^H\mathbf{y}. \tag{5.17}$$

It is known [56, 57] that the iteration in (5.14) is convergent if the spectral radius of the matrix $-\mathbf{S}^{-1}(\mathbf{R}-\mathbf{S})$,denoted as $\rho(-\mathbf{S}^{-1}(\mathbf{R}-\mathbf{S}))$, is strictly smaller than one.

Theorem 5.1.1. *The iteration in* (5.14) *is convergent, i.e.,* $\rho(-\mathbf{S}^{-1}(\mathbf{R}-\mathbf{S})) < 1$ *if* $\mathbf{R} = \underline{\mathbf{H}}_{\text{eff}}^{H}\underline{\mathbf{H}}_{\text{eff}} + \gamma^{-1}\mathbf{I}$ *is a positive definite Hermitian matrix.*

Proof. In order to prove the convergence, we should show that $|\lambda(-\mathbf{S}^{-1}(\mathbf{R}-\mathbf{S}))| < 1$ where λ denotes any eigenvalue of $-\mathbf{S}^{-1}(\mathbf{R}-\mathbf{S})$. For the corresponding eigenvector $\mathbf{v}$ where $\mathbf{v}^{H}\mathbf{v} = \beta > 0$, we can write

$$-\mathbf{S}^{-1}(\mathbf{R}-\mathbf{S})\mathbf{v} = \lambda(-\mathbf{S}^{-1}(\mathbf{R}-\mathbf{S}))\mathbf{v}. \tag{5.18}$$

After multiplying both sides of (5.18) by $\mathbf{v}^{H}\mathbf{S}$, it writes as

$$\lambda(-\mathbf{S}^{-1}(\mathbf{R}-\mathbf{S})) = \frac{\mathbf{v}^{H}(-(\mathbf{R}-\mathbf{S}))\mathbf{v}}{\mathbf{v}^{H}\mathbf{S}\mathbf{v}}. \tag{5.19}$$

Considering (5.15) and (5.16), (5.19) becomes

$$\lambda(-\mathbf{S}^{-1}(\mathbf{R}-\mathbf{S})) = \frac{-\mathbf{v}^{H}\mathbf{L}^{H}\mathbf{v}}{(\gamma^{-1}+d)\mathbf{v}^{H}\mathbf{v} + \mathbf{v}^{H}\mathbf{L}\mathbf{v}}. \tag{5.20}$$

Since $\mathbf{R} = \underline{\mathbf{H}}_{\text{eff}}^{H}\underline{\mathbf{H}}_{\text{eff}} + \gamma^{-1}\mathbf{I}$ is positive definite Hermitian matrix, any non-zero vector including $\mathbf{v}$ satisfies

$$\mathbf{v}^{H}(\underline{\mathbf{H}}_{\text{eff}}^{H}\underline{\mathbf{H}}_{\text{eff}} + \gamma^{-1}\mathbf{I})\mathbf{v} = \mathbf{v}^{H}(\mathbf{L} + \mathbf{L}^{H}(d+\gamma^{-1})\mathbf{I})\mathbf{v} = \beta(d+\gamma^{-1}) + 2\mathcal{R}(\mathbf{v}^{H}\mathbf{L}\mathbf{v}) > 0 \tag{5.21}$$

where (5.21) can be written as

$$a = \mathcal{R}(\mathbf{v}^{H}\mathbf{L}\mathbf{v}) = \mathcal{R}(\mathbf{v}^{H}\mathbf{L}^{H}\mathbf{v}) > \frac{-\beta(d+\gamma^{-1})}{2} \tag{5.22}$$

and the imaginary part is equal to

$$b = \mathcal{I}(\mathbf{v}^H \mathbf{L} \mathbf{v}) = -\mathcal{I}(\mathbf{v}^H \mathbf{L}^H \mathbf{v}). \tag{5.23}$$

Therefore, (5.19) can be rewritten as

$$|\lambda(-\mathbf{S}^{-1}(\mathbf{R}-\mathbf{S}))| = \frac{|a - \imath b|}{|\beta(\gamma^{-1}+d) + a - \imath b|}. \tag{5.24}$$

From (5.22) and (5.24), it can be seen that $|\lambda(-\mathbf{S}^{-1}(\mathbf{R}-\mathbf{S}))| < 1$. □

Relation to the Gauss-Seidel method

LMMSE equalization is equivalent to solving the system of of linear equations $(\underline{\mathbf{H}}_{\text{eff}}^H \underline{\mathbf{H}}_{\text{eff}} + \gamma^{-1}\mathbf{I})\mathbf{x} = \underline{\mathbf{H}}_{\text{eff}}^H \mathbf{y}$. One way to solve it is using the properties of the Gauss-Seidel iterative method for solving linear equations [56]. According to this method, decomposing $\underline{\mathbf{H}}_{\text{eff}}^H \underline{\mathbf{H}}_{\text{eff}} + \gamma^{-1}\mathbf{I}$ additively in its diagonal part $(d + \gamma^{-1}\mathbf{I})$, its strict lower triangular part $\mathbf{L}$ as well as its strict upper triangular part $\mathbf{L}^H$, gives $\mathbf{x}^{(n)}$ as

$$\hat{\mathbf{x}}^{(n)} = -((\gamma^{-\mathbf{1}} + \mathbf{d})\mathbf{I} + \mathbf{L})^{-1} \mathbf{L}^H \mathbf{x}^{(n-1)} + ((\gamma^{-\mathbf{1}} + \mathbf{d})\mathbf{I} + \mathbf{L})^{-1} \underline{\mathbf{H}}_{\text{eff}}^H \mathbf{y}. \tag{5.25}$$

This means that weighted MRC-based DFE converges to the LMMSE estimate, which is confirmed by simulation results.

5.2 Channel Estimation

This section proposes a channel estimation scheme based on the transmission of an embedded pilot symbol, which is surrounded by null guard samples on each side. These guard samples separate the data symbols from the pilot symbol, allowing the channel estimation to be conducted at the receiver without interference from the data symbols. In a similar vein, data detection using the estimated channel occurs without interference

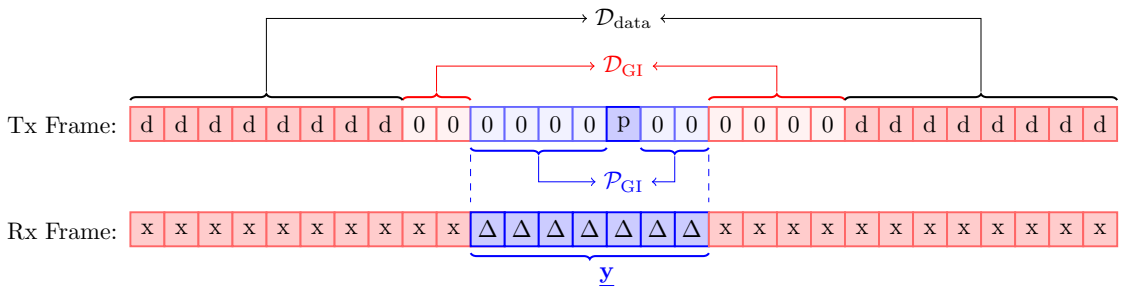

Figure 5.3: Transmitted and received AFDM frame

from the pilot symbol. In this approach, an N-long DAFT domain frame, denoted as $x[m], m = 0 \cdots N-1$ is described as follows

$$x[m] = \begin{cases} x_{\text{pilot}}, & m = m_0 \\ 0, & m \in \mathcal{P}_{\text{GI}} \cup \mathcal{D}_{\text{GI}} \\ x_m^{\text{data}}, & m \in \mathcal{D}_{\text{data}} \end{cases} \tag{5.26}$$

where x_{pilot} is the embedded pilot symbol with index m_0, x_m^{data} is the m-th data symbol, $\mathcal{P}_{\text{GI}}$ is the set of null guard indices useful for pilot based channel estimation and sensing while $\mathcal{D}_{\text{GI}}$ is the set of null guard indices that guarantee pilot-data orthogonality. Note that $\mathcal{D}_{\text{data}} = \{0, ..., N-1\} \backslash (\mathcal{P}_{\text{GI}} \cup \mathcal{D}_{\text{GI}} \cup \{m_0\})$ is the set of the indices of the data symbols. Finally, we set $\mathbb{E}[|x_{\text{pilot}}|^2] = |\mathcal{P}_{\text{GI}} \cup \mathcal{D}_{\text{GI}}| \mathbb{E}[|x_m^{\text{data}}|^2]$ because the DAFT domain null interval allows for boosting the pilot power without resulting in an increase in the average transmit power.

Considering a DAFT domain pilot symbol at position m_0 as in (5.26), it was shown in Section 3.2 that an input-output relation leads to the received samples related to the above pilot symbol being significant only in the following interval

$$m_0 - (\xi_\nu + k_{\max}) - 2Nc_1 l_{\max} \leq m \leq m_0 + (\xi_\nu + k_{\max}), \tag{5.27}$$

provided that ξ_ν is chosen large enough (for the ratio of complex exponentials in (3.11)

to be small enough in modulus when moving away from its peak) and where in the case of negative indices modulo N operation applies. We thus set the guard indices set $\mathcal{P}_{\mathrm{GI}}$ to be equal to the interval in (5.27). The set $\mathcal{D}_{\mathrm{GI}}$ is chosen to be of the same length. Moreover, to have a full delay-Doppler representation of the channel, c_1 as mentioned in Section 4.1 is set to $\frac{2(\xi_\nu + k_{\max})}{2N}$ to separate all the paths in the DAFT domain.

For channel estimation at the receiver, only the segment of the received signal corresponding to the pilot symbol, x_{pilot}, as highlighted in blue in Fig. 5.3, is utilized. This subset of symbols can be described mathematically using the following equation

$$\underline{\mathbf{y}} = \underline{\mathbf{h}}_{\mathrm{eff}}^{m_0} x_{\mathrm{pilot}} + \underline{\mathbf{w}} \tag{5.28}$$

where $\underline{\mathbf{y}}$ and $\underline{\mathbf{h}}_{\mathrm{eff}}^{m_0}$ are respectively the parts of $\mathbf{y}$ and the m_0-th column of $\mathbf{H}_{\mathrm{eff}}$. They can be expressed as $\underline{\mathbf{y}} = \{y[m] | m \in \mathcal{P}_{\mathrm{GI}} \cup \{m_0\}\}$ and $\underline{\mathbf{h}}_{\mathrm{eff}}^{m_0} = \{\mathbf{H}_{\mathrm{eff}}[m, m_0] | m \in \mathcal{P}_{\mathrm{GI}} \cup \{m_0\}\}$. The channel estimation can be done using ML estimation by minimizing the log-likelihood function

$$l(\underline{\mathbf{y}} | \boldsymbol{\theta}, \mathbf{x}) = \|\underline{\mathbf{y}} - \underline{\mathbf{h}}_{\mathrm{eff}}^{m_0} x_{\mathrm{pilot}}\|^2, \tag{5.29}$$

where $\boldsymbol{\theta} = [\boldsymbol{h}, \boldsymbol{\tau}, \boldsymbol{f}]$ ($\boldsymbol{h} = [h_0, ..., h_{P-1}]$, $\boldsymbol{l} = [\tau_0, ..., \tau_{P-1}]$ and $\boldsymbol{f} = [f_0, ..., f_{P-1}]$) is the vector containing the unknown parameters. Thus, the ML estimator is given by

$$\hat{\boldsymbol{\theta}} = \arg \min_{\boldsymbol{\theta} \in \mathbb{C}^P \times \mathbb{R}^P \times \mathbb{R}^P} \|\underline{\mathbf{y}} - \sum_{i=0}^{P-1} h_i \underline{\mathbf{h}}_i^{m_0}(\tau_i, f_i) x_{\mathrm{pilot}}\|^2, \tag{5.30}$$

where $\underline{\mathbf{h}}_i^{m_0}(\tau_i, f_i)$ is m_0-th column of $\mathbf{H}_i(\tau_i, f_i)$ and $h_i \mathbf{H}_i(\tau_i, f_i)$ is the channel matrix of $i-$th path.

The process of implementing ML estimation in a 3P-dimensional continuous domain is a daunting challenge due to the vastness of the search space. Each additional dimension exponentially increases the potential solutions, leading to an immense computational burden. This surge in calculations means that performing an exhaustive search for the

best solution within a practical timeframe, especially when immediate processing is paramount, becomes virtually impossible. Thus, a direct brute-force approach to solve this ML estimation is not viable. A possible low-complexity alternative to the equation (6.8) employs the same approach as described in [28, 58]. Given that the log-likelihood function in (6.7) is quadratic with respect to the complex gain h_i for a given τ_i, f_i, one can determine the value of h_i by resolving the following linear system of equations

$$\sum_{j=0}^{P-1} h_j(\underline{\mathbf{h}}_i^{m_0}(\tau_i, f_i))^H \underline{\mathbf{h}}_j^{m_0}(\tau_j, f_j) = \frac{1}{x_{\text{pilot}}}(\underline{\mathbf{h}}_i^{m_0}(\tau_i, f_i))^H \underline{\mathbf{y}}, i = 0, 1 \cdots P-1. \tag{5.31}$$

Expanding (6.8) and using (5.31), the minimization with respect to the $\{\tau_i, f_i\}$ reduces to maximizing the function

$$\begin{aligned} l_2(\underline{\mathbf{y}}_E|\boldsymbol{\theta}, x_{\text{pilot}}) = &\sum_{i=0}^{P-1} \frac{|(\underline{\mathbf{h}}_i^{m_0}(\tau_i, f_i))^H \underline{\mathbf{y}}|^2}{(\underline{\mathbf{h}}_i^{m_0}(\tau_i, f_i))^H \underline{\mathbf{h}}_i^{m_0}(\tau_i, f_i)} \\ &- \frac{(\sum_{j\neq i} h_j(\underline{\mathbf{h}}_i^{m_0}(\tau_i, f_i))^H \underline{\mathbf{h}}_j^{m_0}(\tau_j, f_j))\underline{\mathbf{y}}^H \underline{\mathbf{h}}_i^{m_0}(\tau_i, f_i) x_{\text{pilot}}}{(\underline{\mathbf{h}}_i^{m_0}(\tau_i, f_i))^H \underline{\mathbf{h}}_i^{m_0}(\tau_i, f_i)}. \end{aligned} \tag{5.32}$$

Considering this fact that $(\underline{\mathbf{h}}_i^{m_0}(\tau_i, f_i))^H \underline{\mathbf{h}}_i^{m_0}(\tau_i, f_i) = 1$, 5.33 simplified as

$$l_2(\underline{\mathbf{y}}_E|\boldsymbol{\theta}, x_{\text{pilot}}) = \sum_{i=0}^{P-1} |(\underline{\mathbf{h}}_i^{m_0}(\tau_i, f_i))^H \underline{\mathbf{y}}|^2 - (\sum_{j\neq i} h_j(\underline{\mathbf{h}}_i^{m_0}(\tau_i, f_i))^H \underline{\mathbf{h}}_j^{m_0}(\tau_j, f_j))\underline{\mathbf{y}}^H \underline{\mathbf{h}}_i^{m_0}(\tau_i, f_i) x_{\text{pilot}}. \tag{5.33}$$

One of the main challenges in this equation is the presence of the second term, which is linked with complex gains. These gains, not being directly observable, need to be estimated. The estimation process is further complicated by the fact that it relies on another equation, (5.31). This interdependence means that a straightforward or direct approach to maximize (5.33) becomes unattainable. Because of this complexity, the procedure to extract delay-Doppler information cannot be executed in once. Instead, it demands an iterative approach. This iterative nature can be resource-intensive, potentially leading to computational inefficiencies. In light of these challenges, researchers

Algorithm 5.2.1 Channel estimation algorithm

Find the integer delays and Doppler shifts, $(l_i, k_i)_{i=1,\dots,P}$, by finding the indices of the largest P entries of $|\underline{\mathbf{y}}|^2$

Find the fractional part, using $(\hat{l}_i, \hat{k}_i)_{i=1,\dots,P}$

$$(\hat{\iota_i}, \hat{\kappa_i})_{i=1,\dots,P} = \arg\max_{\iota_i,\kappa_i} \sum_{i=0}^{P-1} |\underline{\mathbf{h}}_i^{m_0}(\frac{\hat{l}_i + \iota_i}{N\Delta f}, \frac{\hat{k}_i + \kappa_i}{T})^H \underline{\mathbf{y}}|^2,$$

Find the complex gain using the estimated delays and Doppler shifts by solving the linear system (5.31).

and practitioners alike have sought simplifications.

A breakthrough in this regard comes from the observation related to the second term of (5.33). If one were to assume that this term is zero or negligible, it might initially seem like a substantial oversimplification. However, empirical tests have shown that such an assumption doesn't significantly deviate from the true results. This robustness stems from the inherent characteristics of AFDM, particularly its path separation property. This property ensures that, even in the face of such simplifications, the core essence and accuracy of the delay-Doppler information are retained. Equipped with this newfound understanding, it becomes possible to navigate the problem more efficiently. By relying on this assumption, a more direct approach can be adopted to estimate the delay-Doppler information of the paths without getting entangled in the original complexities of (5.33). By adopting the assumption that the second term is negligible, a more direct approach emerges for extracting delay-Doppler information. This leads us to the subsequent equation, which provides a simplified yet effective means to determine the delay-Doppler details of the paths

$$[\hat{\boldsymbol{\tau}}, \hat{\boldsymbol{f}}] = \arg \max_{[\boldsymbol{\tau},\boldsymbol{f}]\in\mathbb{R}^P\times\mathbb{R}^P} \sum_{i=0}^{P-1} |(\underline{\mathbf{h}}_i^{m_0}(\tau_i, f_i))^H \underline{\mathbf{y}}|^2. \tag{5.34}$$

To simplify, the method has two main steps as given in Algorithm 5.2.1. First, we get the delay-Doppler details from equation (6.11). Subsequently, leveraging this delay-Doppler information, the complex gains for each path are estimated by resolving the linear system of equations encapsulated in (5.31).

For specific scenarios, solving becomes notably easier. One such case is when both delay and Doppler shift are integers, i.e., $\tau_i = \frac{l_i}{N\Delta f}$ and $f_i = \frac{k_i}{T}$ where $l_i, k_i \in \mathcal{N}$. The integer nature of these values significantly streamlines the solution process, reducing complexity and enhancing computational efficiency. This allows for quicker and more accurate channel estimation. Referring to (3.39), it becomes evident that $\underline{\mathbf{h}}_i^{m_0}(\frac{l_i}{N\Delta f}, \frac{k_i}{T})$ consists of a singular non-zero element. Furthermore, when comparing multiple paths, the positions of these non-zero elements vary, ensuring that each path has its distinct signature, or in other words, no two paths have non-zero elements in the same location, i.e.,

$$(\underline{\mathbf{h}}_i^{m_0}(\frac{l_i}{N\Delta f}, \frac{k_i}{T}))^H \underline{\mathbf{h}}_j^{m_0}(\frac{l_j}{N\Delta f}, \frac{k_j}{T}) = \begin{cases} 1, & i = j \\ 0, & i \neq j \end{cases} \tag{5.35}$$

This distinction simplifies the extraction of individual path characteristics and Thus, (5.31) and (5.33) are rewritten as

$$h_i = \frac{(\underline{\mathbf{h}}_i^{m_0}(\frac{l_i}{N\Delta f}, \frac{k_i}{T}))^H \underline{\mathbf{y}}}{x_{\text{pilot}}}, \quad i = 0, 1, \cdots, P-1. \tag{5.36}$$

$$l_2(\underline{\mathbf{y}}|\boldsymbol{\theta}, x_{\text{pilot}}) = \sum_{i=0}^{P-1} |(\underline{\mathbf{h}}_i^{m_0}(\frac{l_i}{N\Delta f}, \frac{k_i}{T}))^H \underline{\mathbf{y}}|^2, \tag{5.37}$$

respectively. The delays and Doppler shifts, represented by $[l_0, ..., l_{P-1}]/N\Delta f$ and $[k_0, ..., k_{P-1}]/T$, can be deduced by identifying the values that maximize the right side of (5.37). Given the particular structure of $\underline{\mathbf{h}}_{i,E,1}(l_i, k_i)$, this maximization aligns with pinpointing the largest values in $\underline{\mathbf{y}}_E$. Further details are provided in Algorithm 5.2.2. Once the $\frac{l_i}{N\Delta f}, \frac{k_i}{T}$ pairs for all paths are identified, their complex gains can be calculated using (5.36).

Algorithm 5.2.2 Channel estimation algorithm for integer delay and Doppler shift

Get $\underline{\mathbf{y}}$

Find the indices of the largest P entries of $|\underline{\mathbf{y}}|^2$ as a vector $\mathbf{v}$

for $i = 0, ..., P-1$ **do**

Update $v[i]$ as $v[i] = (v[i] > k_{\max})(v[i] + N_Q) + (v[i] \leq k_{\max})v[i]$

Compute $\text{loc}_i = (-v[i])_N$

Compute the delay and Doppler shift

$$l_i = \lfloor \frac{(\text{loc}_i + k_{\max})_N}{1 + 2k_{\max}} \rfloor$$

$$\nu_i = \text{loc}_i - (1 + 2k_{\max})l_i$$

Update k_i as $k_i = (|k_i| > k_{\max})(k_i - N) + (|k_i| \leq k_{\max})k_i$

Find the complex gain using (5.36)

$$\hat{h}_i = \frac{1}{e^{j\frac{2\pi}{N}(Nc_1 l_i^2 - Nc_2 v(i)^2)}} . \frac{y[v[i]]}{x_{\text{pilot}}}.$$

end

5.3 Simulation Results

In this section, we aim to evaluate the proposed detection and channel estimation algorithms for AFDM through simulation results. We will compare the performance of OFDM, AFDM with $N = 256$, and OTFS with $N_{\text{OTFS}} = 16$ and $M_{\text{OTFS}} = 16$, all using QPSK symbols. These evaluations are conducted in a LTV channel characterized by $l_{\max} = 2$ and $k_{\max} = 3$. For all simulations, the complex gains h_i are generated as independent complex Gaussian random variables, having zero mean and a variance of $\frac{1}{P}$. We set the carrier frequency at 4 GHz and determine the BER values using 10^6 distinct channel realizations.

Fig. 5.4 compares the performance of AFDM and OFDM in terms of BER using different detectors. In this figure, integer and fractional Doppler shifts are considered. We observe that AFDM outperforms OFDM, owed to achieving the optimal diversity order and every information symbol being received through multiple independent non-overlapping paths. Moreover, it shows that the weighted MRC-based DFE has close

performance to exact LMMSE, which validates Theorem 5.1.1. In Fig. 5.4a, all BER curves (i.e., of the two methods and of low-complexity MMSE [27] based on banded matrix approximation) coincide because the channel matrices used in the three detection methods are all the same and are banded without approximation. In Fig. 5.4b, exact LMMSE has slightly better performance than the low-complexity methods due to the use of the banded-matrix approximation in the latter when Doppler frequency shifts are fractional.

We now assess the BER performance of AFDM when detection is performed based on the channel state information given by the proposed channel estimation scheme. The pilot symbol SNR is denoted by $\mathrm{SNR_p} = \frac{|x_{\mathrm{pilot}}|^2}{N_0}$ and the data symbols have the $\mathrm{SNR_d} = \frac{\mathbb{E}\{|x^{\mathrm{data}}|^2\}}{N_0}$. Fig. 5.5 shows the BER versus $\mathrm{SNR_d}$ for AFDM considering the ideal case of perfect channel knowledge at the receiver as well as the case where the channel is estimated using the proposed algorithm for integer Doppler case with different values of $\mathrm{SNR_p}$. As $\mathrm{SNR_p}$ increases, the BER decreases and the AFDM performance improves. Moreover, we see that for $\mathrm{SNR_p} = 35$ dB, the performance of AFDM with the proposed channel estimation is very close to the ideal case.

Fig. 5.6a shows the BER performance of AFDM for different $\mathrm{SNR_p}$ considering the fractional Doppler shift case. Similar to the integer Doppler shift case, increasing the pilot power improves the error performance. As we can see, with $\mathrm{SNR_p} = 40$ dB, AFDM with the proposed embedded channel estimation has similar performance with AFDM with perfect channel knowledge at the receiver. Note that the system has more overhead in the fractional Doppler shift case. In addition, larger $\mathrm{SNR_p}$ is needed to achieve the same performance. Note that in practice, as mentioned it is possible to assume larger values for $\mathrm{SNR_p}$ compared to $\mathrm{SNR_d}$ since the zero guard samples surrounding the pilot symbol allow for the transmit power of the latter to be boosted without violating the average transmit power constraint. Under ideal receiver-side channel knowledge, it can be seen from Fig. 5.6b that increasing ξ_ν, improves the performance of AFDM, as less

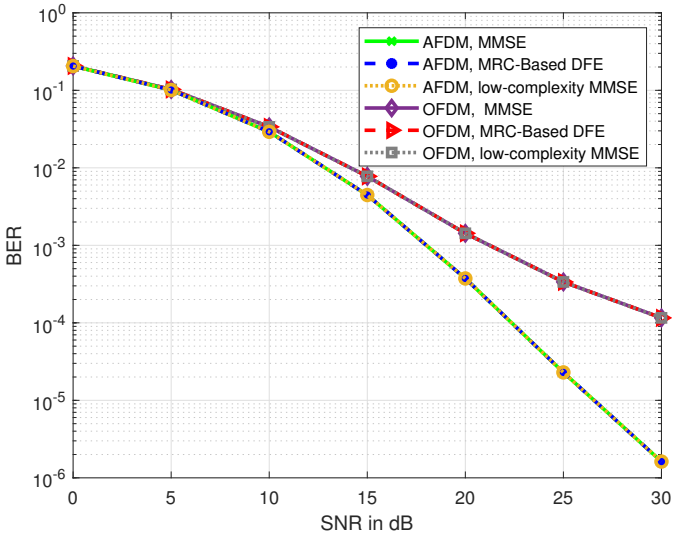

(a) Integer Doppler shifts

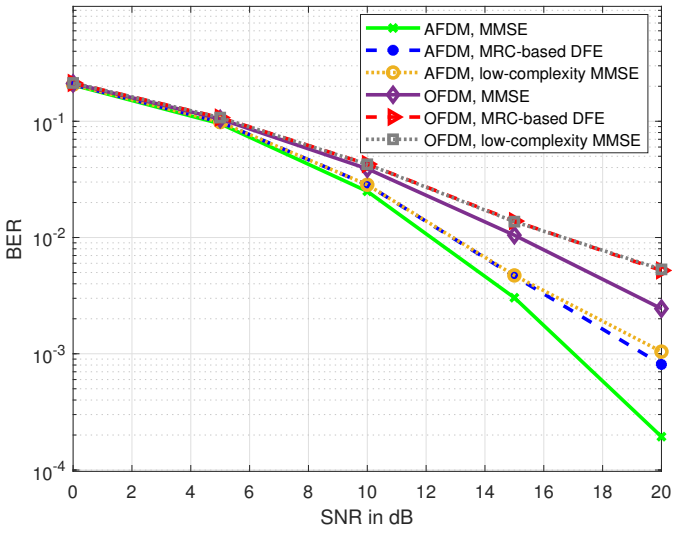

(b) Fractional Doppler shifts

Figure 5.4: BER performance comparison between AFDM and OFDM systems using different detectors for the integer and fractional Doppler shifts.

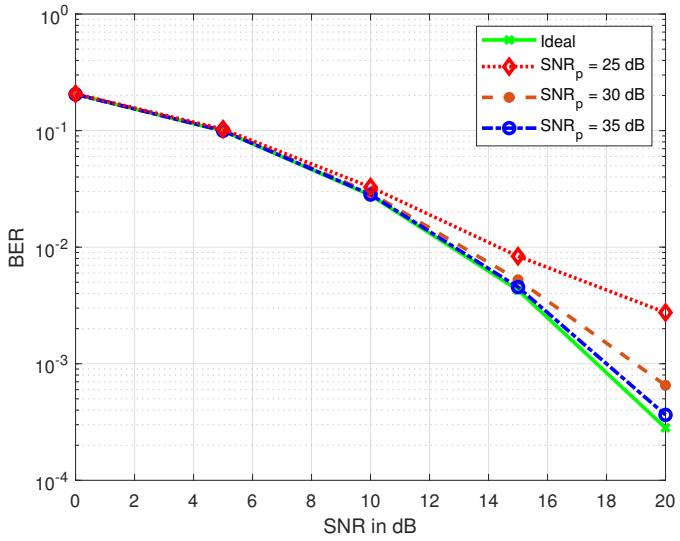

Figure 5.5: BER versus $\mathrm{SNR_d}$ for the integer Doppler case with different $\mathrm{SNR_p}$ and ideal channel.

overlapping is occurring between the matrices $\mathbf{H}_i$ belonging to different channel paths in the effective channel matrix $\mathbf{H}_{\text{eff}}$. With practical channel estimation, Fig. 5.6b shows that increasing ξ_ν also improves the channel estimation quality, since inter-path interference when channel estimation algorithm for fractional Doppler shift case is performed decreases for the same reason, i.e, less overlapping between the matrices $\mathbf{H}_i$.

Now, we aim to compare the spectral efficiency of both AFDM and OTFS, particularly when considering guard symbols. It's pertinent to note that when channel estimation is integrated, OTFS has a pilot overhead that is twice as much as that of AFDM. This is due to the 2D structure inherent in OTFS's underlying transform. Indeed, while the AFDM embedded pilot scheme presented in Section 5.2 occupies $2(l_{\max}+1)(2(k_{\max}+\xi_\nu)+1)-1$ entries out of the N entries of the AFDM symbol, its OTFS counterpart [24] requires $(4(k_{\max}+\xi_\nu)+1)\,(2l_{\max}+1)$ (for the integer Doppler shifts $\xi_\nu = 0$). This difference as shown in Fig. 5.8 translates into a significant advantage of AFDM over OTFS in terms of spectral efficiency, as shown in Fig. 5.7b. The spectral efficiency values were derived from the BER values plotted in Fig. 5.7a.

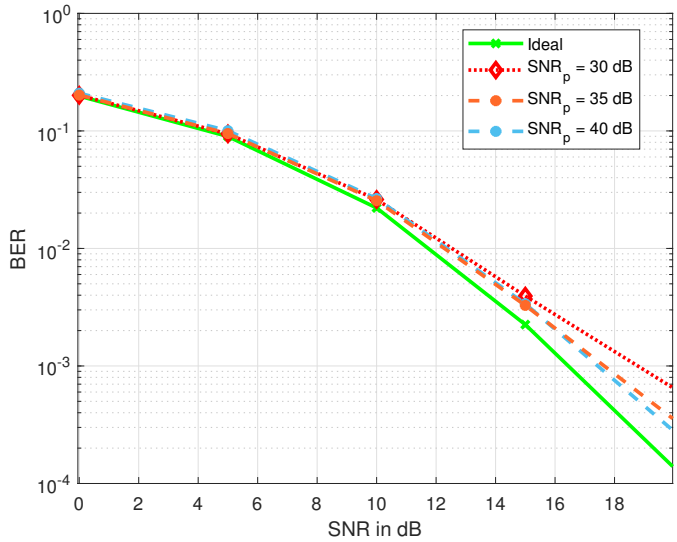

(a) BER versus $\mathrm{SNR_d}$ considering different $\mathrm{SNR_p}$ and ideal receiver-side CSI

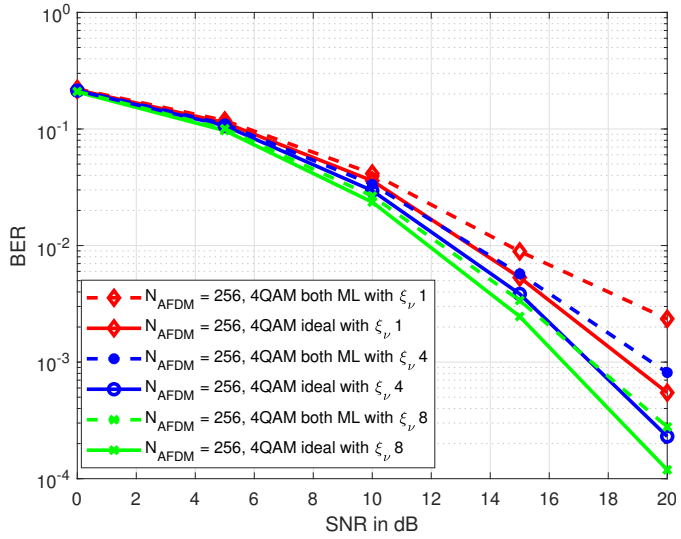

(b) BER versus SNR_d with different ξ_ν considering ideal and estimated channel with $\mathrm{SNR_p} = 40$ dB

Figure 5.6: The effect of $\mathrm{SNR_p}$ and ξ_ν on the BER performance

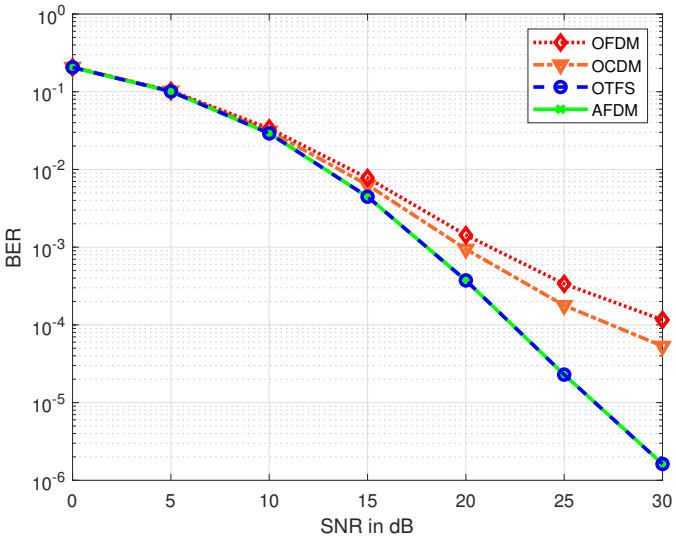

(a) BER

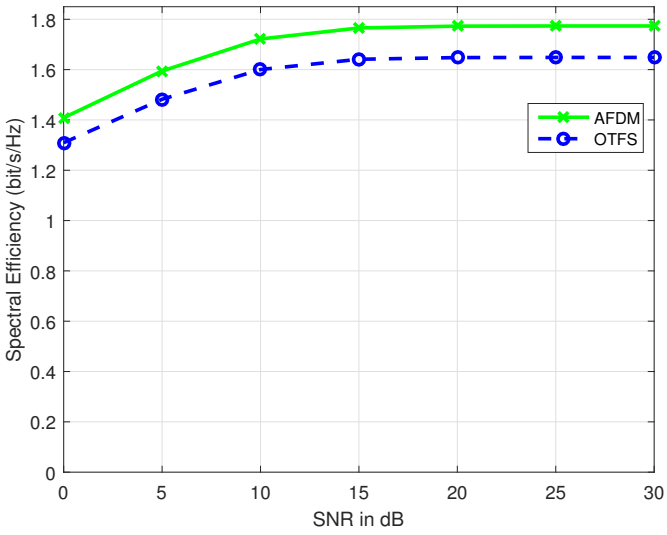

(b) Spectral efficiency

Figure 5.7: BER and spectral efficiency performance of OFDM, OCDM, OTFS and AFDM using MMSE detection.

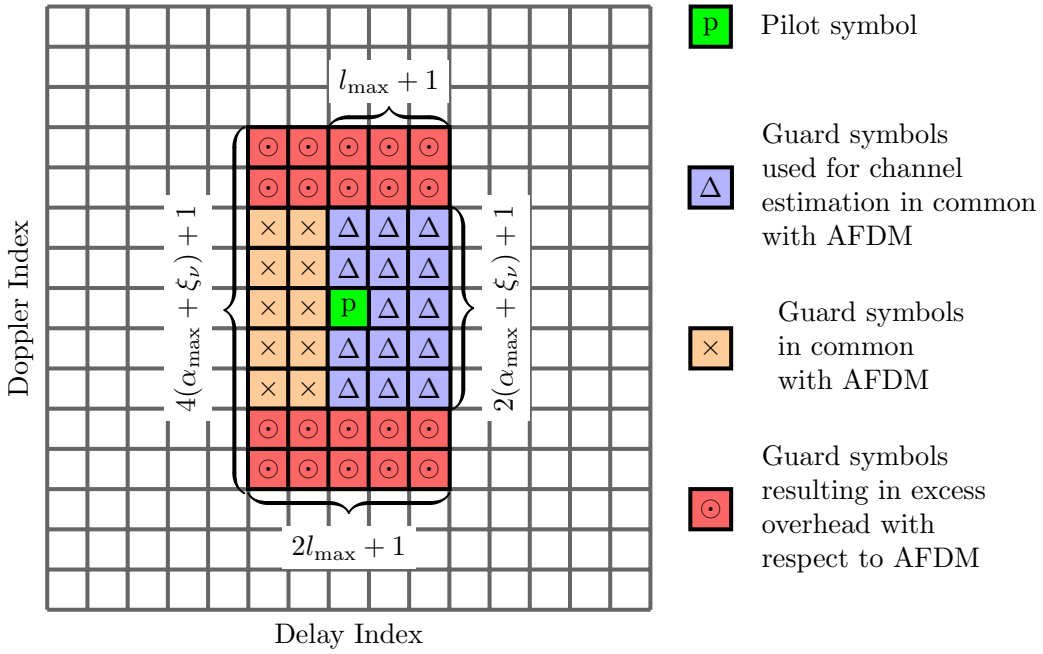

Figure 5.8: Excess pilot guard overhead in OTFS with respect to AFDM

5.4 Conclusion

Throughout this chapter, we delved into the intricate realms of detection and channel estimation, both critical processes in the communication system landscape. Recognizing the practical limitations of ML detection, we shifted our focus towards the development of alternative detection mechanisms for AFDM. This led us to propose two low-complexity detection algorithms that tap into the inherent channel sparsity of AFDM. First one was a detector based on the LDL factorization and the second one was an iterative DFE based on weighted MRC of the channel impaired input symbols received from different paths.

Moreover, we bridged the gap between channel estimation and data detection. Our innovative embedded pilot-aided channel estimation scheme illustrates this point clearly, allowing both processes to seamlessly function within a single AFDM frame. This holistic approach ensures that the receiver is armed with precise channel knowledge, optimizing

the detection process, and subsequently improving overall system performance.

As we conclude this chapter, it becomes evident that our endeavors aim to strike a balance between complexity and efficiency. By proposing algorithms that reduce computational burden and integrate channel estimation with data detection, we've paved the way for more resilient and efficient AFDM-based communication systems.

Chapter 6

Further Applications

In our journey of understanding the potentials of AFDM, it becomes essential to see how this modulation technique can be utilized beyond its primary applications. While we've delved deep into its foundational principles and typical uses, the scope of AFDM extends far beyond, touching realms at the forefront of communication technology's evolution. This chapter delves into the further applications of AFDM, spotlighting its promising role in two groundbreaking areas: Integrated sensing and communication and communication in extremely high frequency bands. While ISAC represents the convergence of communication and radar sensing for a harmonious coexistence, EHF communication faces unique challenges intrinsic to high-frequency transmissions. Throughout this chapter, we will detail how AFDM, with its distinct properties, can present solutions to these advanced domain challenges, paving the way for future explorations and applications.

6.1 Integrated Sensing and Communications

Traditionally, wireless communications and radar sensing evolved as distinct domains, each tailored to specific requirements and operating in dedicated frequency bands. However, in recent years, there's been a convergence towards an ISAC model [59, 60]. This shift is primarily driven by the promise of ISAC's inherent benefits like reduced power

usage, enhanced spectral efficiency, and minimized hardware expenses[59]. ISAC is not just a conceptual fusion; it's an efficient solution addressing the imminent coexistence challenges between communication and radar. One might note that both radar sensing and communication share inherent channel characteristics. Take, for instance, a typical downlink scenario in a mobile network where both the radar and communication antennas are situated at the base station (BS). The physical channel connecting the BS to user equipment remains consistent for both functions, even though their operational principles differ. Radar sensing leverages parameters like delay and Doppler tied to identifiable paths. This core principle aligns seamlessly with the AFDM modulation used in communications. AFDM's full Delay-Doppler representation of the channel facilitates a direct engagement between the information symbols and the DD domain channel. This channel response can likely be derived from radar estimates, bridging communication and radar sensing in a harmonized framework, thus guiding our exploration into ISAC designs founded on AFDM modulation.

Numerous research initiatives have delved into the design of a dual-functional waveform as it is crucial in ISAC systems to achieve integration gain by sharing signaling resources for sensing and communication. OFDM has been extensively studied in ISAC waveform design and signal processing methods [61]; however, it suffers from inter-carrier interference and consequent communication performance deterioration in high-mobility scenarios. OCDM [14] is an alternative scheme which has lower BER than OFDM [62], at the cost of higher computational complexity. Nevertheless, OCDM cannot achieve the optimal diversity order of LTV channels [28], resulting as well in higher hardware complexity. OTFS [19, 20] also has been investigated due to its resilience to high Doppler shifts. For example, the effectiveness of OTFS modulation for ISAC transmission has been evaluated in [58], where the authors have shown that the estimation error lower bounds for radar sensing can be achieved by using OTFS signals while maintaining a satisfactory communication performance.. Nonetheless, all aforementioned methods rely on the strong

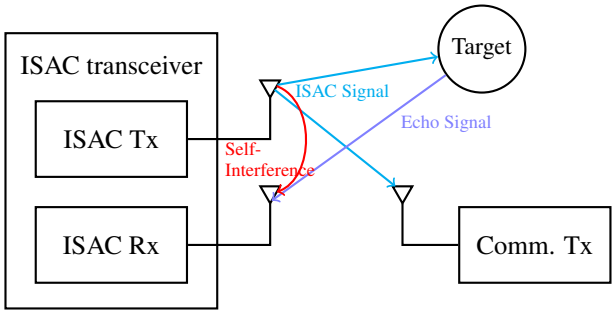

Figure 6.1: AFDM-based ISAC system model

assumption of ideal self-interference cancellation (SIC), which in turn requires costly full duplex SIC methods.

In this section, we propose a novel ISAC scheme leveraging AFDM. We show that AFDM can be used for ISAC either using the whole frame as showed in [63], or using one pilot symbol, motivated from the mentioned embedded channel estimation in which as few as one DAFT domain symbol used as a pilot can yield, when appended with a sufficient number of zero guard samples, the possibility to identify all the delay and Doppler components associated with the propagation medium. Moreover, we show that by sensing with one DAFT domain pilot rather than the whole signal, a low-complexity SIC can be implemented even when this pilot multiplexed with data and possibly other pilots.

6.1.1 System Model

The considered ISAC system is shown in Fig. 6.1 and consists of an AFDM-based ISAC transceiver and an AFDM receiver. The ISAC transceiver is equipped with a single antenna monostatic radar and uses the same AFDM waveform for both communication and sensing. The transceiver conveys messages to the receiver while estimating parameters related to the targets using the reflected signal from the targets. For simplicity, we consider a point target model, i.e., the link between a transmitter and a target can be represented by a single-path channel.

6.1.2 AFDM-based ISAC signal model

The full-guard embedded-pilot scheme in (5.26) is considered for AFDM-based ISAC. In the case of P point targets, the wireless link between the ISAC transmitter and receiver is represented by a $P+1$-tap time-frequency (doubly) selective channel

$$\widetilde{h}(t,\tau) = \sum_{i=0}^{P} \widetilde{h}_i e^{-\imath 2\pi \widetilde{f}_i t} \delta(\tau - \widetilde{\tau}_i) \tag{6.1}$$

where $i = 0$ stands for the direct path $\widetilde{h}(t,0) = \widetilde{h}_0$ between the ISAC transmitter and receiver (the direct path has zero delay and Doppler shift). From now on we assume $h_0 = 0$, a justified assumption if some effective SIC (such as the scheme of Subsection 6.1.4) is applied. $\widetilde{h}_i$, $\widetilde{f}_i$ and $\widetilde{\tau}_i$ are the complex gain, Doppler shift, and the delay associated with the i-th target, respectively. In this paper, we assume that the number of targets is already known. Moreover, we assume that the range of the delay and Doppler shift is $[0, \widetilde{\tau}_{\max}]$ and $\left[-\widetilde{f}_{\max}, \widetilde{f}_{\max}\right]$, respectively, where $\widetilde{\tau}_{\max}$ represents the maximum delay and $\widetilde{f}_{\max}$ is the Doppler shift of each target. Let c, f_c, v_i, r_i denote the speed of light, carrier frequency, corresponding velocity and range associated with the i-th target, respectively. Thus, the relative range and velocity of the i-th target are respectively

$$r_i = c \cdot \frac{\widetilde{\tau}_i}{2}, \quad v_i = c \cdot \frac{\widetilde{f}_i}{2f_c}. \tag{6.2}$$

We define the delay and Doppler indices associated with the i-th path by $\widetilde{l}_i$ and $\widetilde{k}_i$, respectively, such that

$$\widetilde{l}_i + \widetilde{\iota}_i = \widetilde{\tau}_i/\Delta t, \quad \widetilde{k}_i + \widetilde{\kappa}_i = T\widetilde{f}_i, \tag{6.3}$$

where $\widetilde{k}_i$ denotes the integer part of the normalized Doppler shift for the i-th path, and $\frac{-1}{2} < \widetilde{\kappa}_i \leq \frac{1}{2}$ represents the corresponding fractional Doppler shift. Similarly, $\widetilde{l}_i$ denotes the integer part of the delay for the i-th path, and $\frac{-1}{2} < \widetilde{\iota}_i \leq \frac{1}{2}$ represents the corresponding fractional delay. Regarding the Doppler shift, we have $\widetilde{k}_i + \widetilde{\kappa}_i \in$

$\left[-\widetilde{k}_{\max}, \widetilde{k}_{\max}\right]$. Here, $\widetilde{k}_{\max}$ is the maximum Doppler index, which can be expressed as $\widetilde{k}_{\max} = \lceil T\widetilde{f}_{\max} \rceil$. As for the delays, the range is defined as $\widetilde{l}_i + \widetilde{\iota}_i \in \left[0, \widetilde{l}_{\max}\right]$, where $\widetilde{l}_{\max}$ represents the maximum delay index, which can be expressed as $\widetilde{l}_{\max} = \lceil \widetilde{\tau}_{\max}/\Delta t \rceil$.

After parallel to serial conversion and transmission over the channel, the received signal at the ISAC receiver writes as

$$\widetilde{r}(t) = \int s_{\mathrm{CPP}}(t-\tau)\widetilde{h}(t,\tau)\mathrm{d}\tau + w(t) = \sum_{i=1}^{P} s_{\mathrm{CPP}}(t-\tau_i)\widetilde{h}(t,\tau_i) + w(t) \tag{6.4}$$

where $w(t) \sim \mathcal{CN}(0, N_0)$ is the additive white noise and s_{CPP} is given in (3.14). Discarding the CPP and using AFDM matirx input-output relation mentioned in section 3.3, the DAFT domain output symbols can be written in matrix form as

$$\widetilde{\mathbf{y}} = \mathbf{A}\widetilde{\mathbf{r}} = \sum_{i=1}^{P} h_i \widetilde{\mathbf{H}}_i(\widetilde{\tau}_i, \widetilde{f}_i)\mathbf{x} + \mathbf{A}\mathbf{w} = \widetilde{\mathbf{H}}_{\mathrm{eff}}\mathbf{x} + \widetilde{\mathbf{w}} \tag{6.5}$$

where $\mathbf{A}$ is the DAFT matrix, $\widetilde{\mathbf{H}}_{\mathrm{eff}} = \mathbf{A}\widetilde{\mathbf{H}}\mathbf{A}^{\mathrm{H}}$, $\widetilde{\mathbf{H}} = \sum_{i=1}^{P} h_i \widetilde{\mathbf{H}}_i(\widetilde{\tau}_i, \widetilde{f}_i)$ is the matrix representation of the channel and $\widetilde{h}_i\widetilde{\mathbf{H}}_i(\widetilde{\tau}_i, \widetilde{f}_i)$ is the channel matrix of each target. Since $\mathbf{A}$ is unitary, $\widetilde{\mathbf{w}} = \mathbf{A}\mathbf{w}$ and $\mathbf{w}$ have the same statistics.

6.1.3 AFDM-based Sensing

At the radar receiver, it is possible to estimate the targets range and velocity using all received DAFT domain samples $\mathbf{y}$ based on the knowledge of the transmitted samples $\mathbf{x}$ of the whole AFDM frame written in (6.5). A possible alternative is to employ for sensing only the received signal section related to the one pilot symbol, x_{pilot}, as indicated in blue in Fig. 5.3. This subset of symbols can be described mathematically using the following equation:

$$\underline{\widetilde{\mathbf{y}}} = \underline{\widetilde{\mathbf{h}}}_{\mathrm{eff}}^{m_0} x_{\mathrm{pilot}} + \underline{\mathbf{w}} \tag{6.6}$$

where $\underline{\widetilde{\mathbf{y}}}$ and $\underline{\widetilde{\mathbf{h}}}_{\mathrm{eff}}^{m_0}$ are derived in a manner consistent with (5.28).

When we take into account the entire frame, this estimation can be formulated as

$$l(\widetilde{\mathbf{y}}|\widetilde{\boldsymbol{\theta}},\mathbf{x}) = \|\widetilde{\mathbf{y}} - \widetilde{\mathbf{H}}_{\text{eff}}\mathbf{x}\|^2, \tag{6.7}$$

where $\widetilde{\boldsymbol{\theta}} = [\widetilde{\boldsymbol{h}}, \widetilde{\boldsymbol{\tau}}, \widetilde{\boldsymbol{f}}]$ ($\widetilde{\boldsymbol{h}} = [\widetilde{h}_1, ..., \widetilde{h}_P]$, $\widetilde{\boldsymbol{\tau}} = [\widetilde{\tau}_1, ..., \widetilde{\tau}_P]$ and $\widetilde{\boldsymbol{f}} = [\widetilde{f}_1, ..., \widetilde{f}_P]$) is the vector containing the unknown parameters. Thus, the ML estimator is given by

$$\hat{\widetilde{\boldsymbol{\theta}}} = \arg \min_{\widetilde{\boldsymbol{\theta}} \in \mathbb{C}^P \times \mathbb{R}^P \times \mathbb{R}^P} \|\widetilde{\mathbf{y}} - \sum_{i=1}^{P} \widetilde{h}_i \widetilde{\mathbf{H}}_i(\widetilde{\tau}_i, \widetilde{f}_i)\mathbf{x}\|^2. \tag{6.8}$$

Using the low-complexity solution detailed in section 5.2, the value of $\widetilde{h}_i$ can be obtained by solving the following linear system of equations

$$\sum_{j=0}^{P-1} \widetilde{h}_j \mathbf{x}^H \widetilde{\mathbf{H}}_i^H(\widetilde{\tau}_i, \widetilde{f}_i)\widetilde{\mathbf{H}}_j(\widetilde{\tau}_j, \widetilde{f}_j)\mathbf{x} = \mathbf{x}^H \widetilde{\mathbf{H}}_i^H(\widetilde{\tau}_i, \widetilde{f}_i)\widetilde{\mathbf{y}}, \quad i = 0, 1 \cdots P-1, \tag{6.9}$$

and the minimization with respect to $\{\widetilde{\tau}_i, \widetilde{f}_i\}$ is equivalent to maximizing the function

$$l(\widetilde{\mathbf{y}}|\widetilde{\boldsymbol{\theta}},\mathbf{x}) = \sum_{i=1}^{P} |\mathbf{x}^H \widetilde{\mathbf{H}}_i^H(\widetilde{\tau}_i, \widetilde{f}_i)\widetilde{\mathbf{y}}|^2 - (\sum_{j \neq i} h_j \mathbf{x}^H \widetilde{\mathbf{H}}_i^H(\widetilde{\tau}_i, \widetilde{f}_i)\widetilde{\mathbf{H}}_j(\widetilde{\tau}_j, \widetilde{f}_j)\mathbf{x})\widetilde{\mathbf{y}}^H \widetilde{\mathbf{H}}_i(\widetilde{\tau}_i, \widetilde{f}_i)\mathbf{x}. \tag{6.10}$$

As already explained, using the path separation property of AFDM, the following equation can be used to determine the delay-Doppler information of the targets

$$[\hat{\widetilde{\boldsymbol{\tau}}}, \hat{\widetilde{\boldsymbol{f}}}] = \arg \max_{[\widetilde{\boldsymbol{\tau}}, \widetilde{\boldsymbol{f}}] \in \mathbb{R}^P \times \mathbb{R}^P} \sum_{i=1}^{P} |\mathbf{x}^H \widetilde{\mathbf{H}}_i^H(\widetilde{\tau}_i, \widetilde{f}_i)\widetilde{\mathbf{y}}|^2 \tag{6.11}$$

As mentioned earlier, one can solve equation (6.11) by breaking it down into two stages. In the first, the estimation of the integer portions of the delay and Doppler shifts is performed, while in the second, the Doppler shift and the delay are refined utilizing a finer grid based on the estimated integer delay and Doppler shifts.

Estimating the range and velocity using a pilot related segment of the output signal

using (6.6) follows the same methodology described for channel estimation in section 5.2.Using only a subset of the time-frequency resources of ISAC signals for sensing has already been proposed (see e.g., [64], for reducing the computational complexity needed for sensing or decoupling the problems of beamforming design for sensing and for communications. In the following we show that in AFDM, doing sensing only using the pilot part has an additional benefit related to SIC. This is because a *single AFDM chirp* is sufficient for getting a full delay-Doppler representation of the channel, a feature that is unique to the AFDM waveform.

6.1.4 SIC for AFDM-based sensing

In monostatic radar, the transmitter and receiver modules are co-located in one device. At the radar receiver, the transmitted signal can be used as a reference signal. Also, the two modules share the same clock and oscillator, so there is no need for additional time and frequency synchronization. However, the direct path $\widetilde{h}(t,0)$ between the ISAC transmitter and receiver, as shown in Fig. 6.1, introduces a significant self-interference (SI) signal. This SI signal interferes with the desired signal reflected by the targets and is orders of magnitude stronger, resulting in demanding dynamic range requirements for the analog-to-digital converter (ADC) in the ISAC receiver. Consequently, this strong SI signal degrades the radar sensing performance, particularly for most practical ADCs. It is thus crucial that a SIC is applied in that receiver before the ADC stage. In this subsection we show that the need for SIC in AFDM-based ISAC can be alleviated with simple analog dechirping and filtering. This is an advantage over OFDM or OTFS-based ISAC solutions that need costly full-duplex SIC methods.

Considering the reference chirp as $R(t) = \frac{1}{\sqrt{T}} e^{\imath 2\pi(\Phi_{m_0}(t))}$ and the direct path as $\widetilde{h}(t,0) = \widetilde{h}_0$ for some $\widetilde{h}_0 \in \mathbb{C}$ (the direct path has zero delay and Doppler shift), the

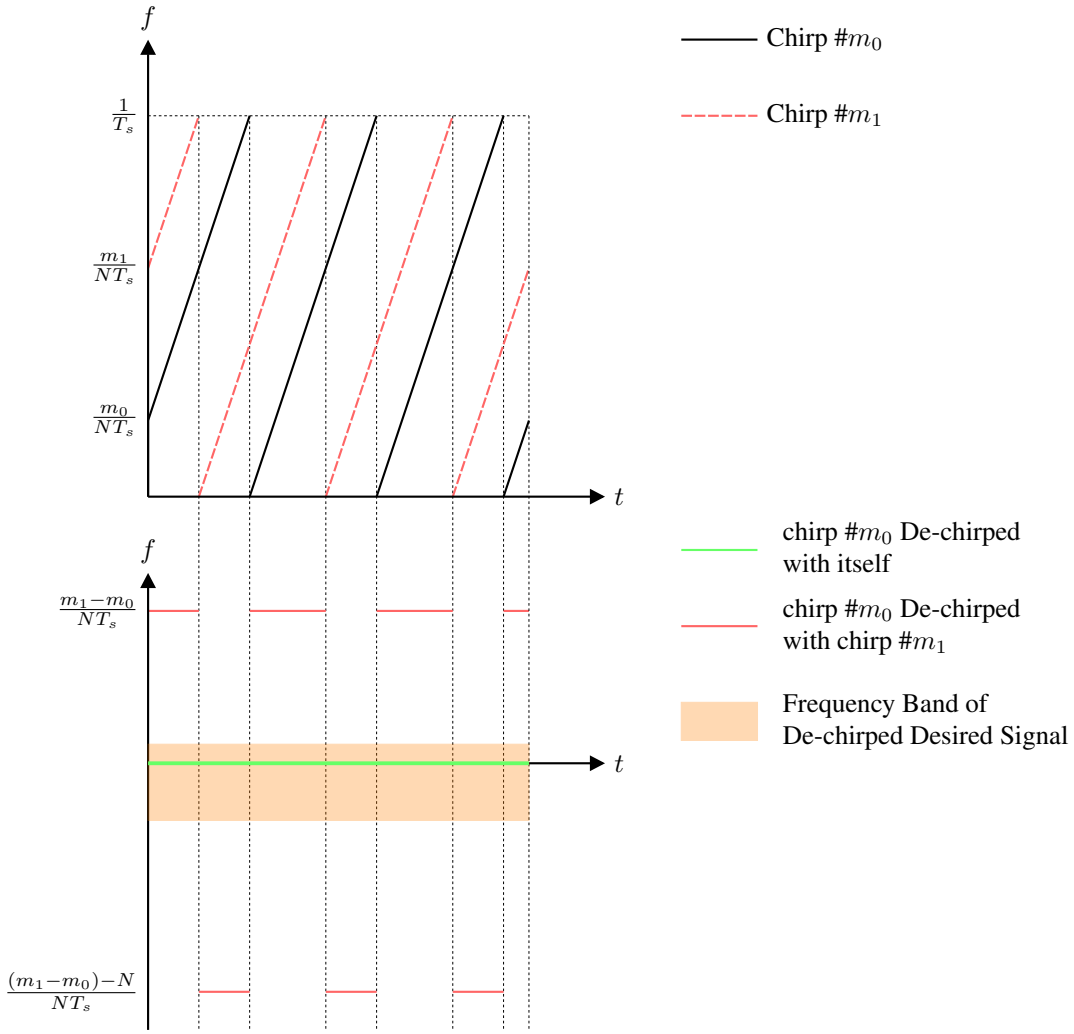

Figure 6.2: Time-frequency representation of two AFDM chirps (the pilot, m_0, and one chirp, m_1, from outside its guard interval) at the transmitter (on top) and after analog dechirping at the radar receiver (on bottom)

output of the dechirping can be written as

$$\begin{aligned} r'(t) = \widetilde{r}(t)R^*(t) &= \left(\sum_{i=0}^{P-1} s_{\mathrm{CPP}}(t-\tau_i)\widetilde{h}(t,\widetilde{\tau}_i) + w(t)\right) R^*(t) \\ &= (\underbrace{s_{\mathrm{CPP}}(t)\widetilde{h}(t,0)}_{I(t)\text{:SI signal}} + \underbrace{\sum_{i=1}^{P-1} s_{\mathrm{CPP}}(t-\widetilde{\tau}_i)\widetilde{h}(t,\widetilde{\tau}_i)}_{E(t)\text{:Echo signal}})R^*(t) + w(t)R^*(t). \end{aligned} \tag{6.12}$$

Taking into account the frame structure (5.26), considering $x'[m] = x[m]e^{\imath 2\pi c_2 m^2}$, $x'_{\mathrm{pilot}} = e^{\imath 2\pi c_2 m_0^2}x_{\mathrm{pilot}}$ and $h'_i = \frac{1}{T}\widetilde{h}_i e^{\imath 2\pi c'_1 \widetilde{\tau}_i^2}$, the dechirped SI and echo signal terms are written as

$$I(t)R^*(t) = \frac{1}{T}h_0 x'_{\mathrm{pilot}} + \frac{1}{T}h_0 \sum_{m\in\mathcal{D}_{\mathrm{data}}} x'[m]e^{\imath 2\pi(\frac{(m-m_0)}{T})t}e^{\imath 2\pi(\alpha_m(t)-\alpha_{m_0}(t))}, \tag{6.13}$$

$$\begin{aligned} E(t)R^*(t) = &\underbrace{\sum_{i=1}^{P-1} h'_i x'_{\mathrm{pilot}} e^{-\imath 2\pi\frac{\widetilde{\tau}_i m_0}{T}} e^{\imath 2\pi(-2c_1\widetilde{\tau}_i - f_i)t} e^{\imath 2\pi(\alpha_{m_0}((t-\widetilde{\tau}_i)_T)-\alpha_{m_0}(t))}}_{\text{dechirped desired signal}} \\ &+ \sum_{i=1}^{P-1} h'_i \sum_{m\in\mathcal{D}_{\mathrm{data}}} x'[m]e^{-\imath 2\pi\frac{\widetilde{\tau}_i m}{T}} e^{\imath 2\pi(-2c_1\widetilde{\tau}_i - f_i + \frac{(m-m_0)}{T})t} e^{\imath 2\pi(\alpha_m((t-\widetilde{\tau}_i)_T)-\alpha_{m_0}(t))}, \end{aligned} \tag{6.14}$$

respectively.

In (6.13), the first term, which corresponds to the pilot symbol, is a direct current (DC) component and can be eliminated with a DC blocking module. The second term, which is the part of the dechirped SI signal related to the the data symbols, appears as segments of complex exponential signals $e^{\imath 2\pi\left(\frac{(m-m_0)}{T}t+\alpha_m(t)-\alpha_{m_0}(t)\right)}$, the instantaneous frequency of which depends on m and m_0. The frequency jumps between these segments is due to the fact that the frequency of $\alpha_m(t)-\alpha_{m_0}(t)$ can take one of the different values $0, -\frac{1}{\Delta t}t$ or $\frac{1}{\Delta t}t$ depending on m and m_0. Fig. 6.2 shows the time-frequency representation of a AFDM signal with two active chirp subcarriers, where one of them being is the sensing pilot, while the other one carries data, and of the output of analog dechirping done using the pilot as the reference chirp. In (6.14), the first term is the dechirped desired

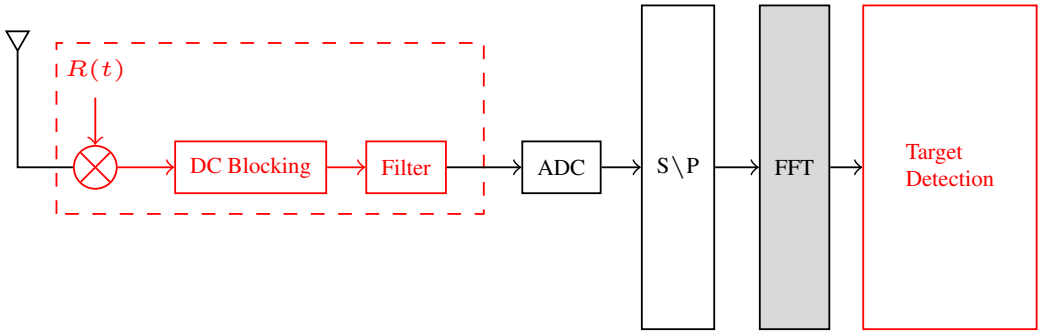

Figure 6.3: AFDM sensing receiver

signal containing the useful delay-Doppler information of the targets and can be utilized for range-velocity estimation. The spectral components of this dechirped desired signal do not overlap with those of dechirped SI signal because their instantaneous frequency is never equal for any m satisfying $m \neq m_0$ and lying outside the DAFT domain guard interval surrounding m_0. Therefore, by employing a DC blocking module and a proper filter, the self-interference can be mitigated. The resulting SI-free signal can be used for sensing purposes by analog-to-digital conversion followed by an N-point FFT module as illustrated in Fig. 6.3. Note that the discontinuities in the frequency of the terms of the dechirped desired signal due to $\alpha_{m_0}((t-\widetilde{\tau}_i)_T) - \alpha_{m_0}(t)$ in (6.14) disappear after sampling at rate $\frac{1}{\Delta t}$ [1] thanks to spectrum folding. Moreover, the second term in (6.14) is the part of the dechirped echo signal related to the data symbols. Its spectral content does not overlap with the frequency band of the dechirped desired signal which is contained in the interval of digital frequencies ranging from $-2Nc_1l_{\max} - k_{\max}$ to $k_{\max}$.

6.1.5 Simulation results

In this section, we present simulation results for evaluating the performance of the proposed ISAC scheme in terms of range and velocity estimation and we compare it with OTFS-based ISAC. Furthermore, the performance of the two proposed schemes are

[1] The sampling rate could be much smaller than $\frac{1}{\Delta t}$ because the desired dechirped signal occupies only a portion of the full bandwidth.

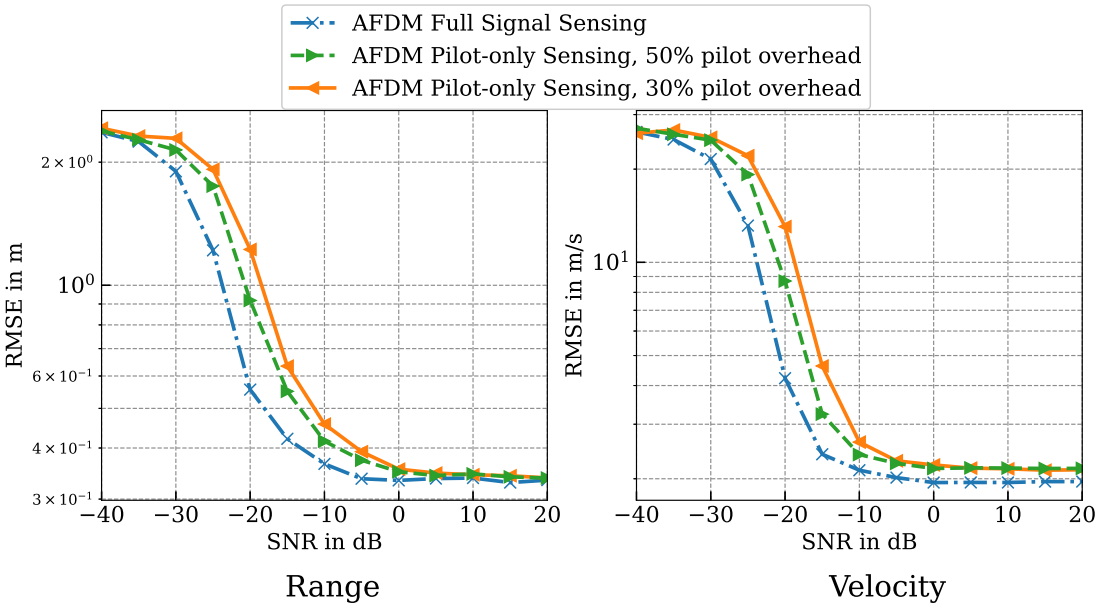

Figure 6.4: AFDM-based ISAC sensing performance using the whole frame and one pilot symbol

compared to show that sensing with one pilot symbol performs almost the same as sensing with the entire frame. The simulation setup is as follows. The size of the AFDM frame is $N = 2048$, the carrier frequency is $f_c = 79$ GHz, the bandwidth is $B = 30.72$ MHz and the frame duration is $T = 66.6$ μs. The maximum range and maximum velocity are set to $R_{\max} = 98$ m and $v_{\max} = 308$ km/h, respectively. When translated into maximum delay and Doppler shift, these values result due to (5.27) (with $\xi_\nu = 4$) in a 30% overhead. i.e, $2Q \sim 0.3N$. The signal-to-noise ratio (SNR) of target i is defined as $\mathrm{SNR}_i = \frac{\mathbb{E}\{|h_i|^2\}}{N_0}$ and is assumed to be the same for all the targets. The results are obtained by averaging over 100000 trials. Root mean square error (RMSE) is used as the performance metric to evaluate the accuracy of range and velocity estimation.

In Fig. 6.4, the RMSE performance of range and velocity estimation using AFDM with one DAFT domain pilot symbol surrounded with a DAFT domain guard interval is given for two values of the total pilot-guard overhead, namely 30% and 50% and compared to the RMSE performance when estimation is based on the whole AFDM

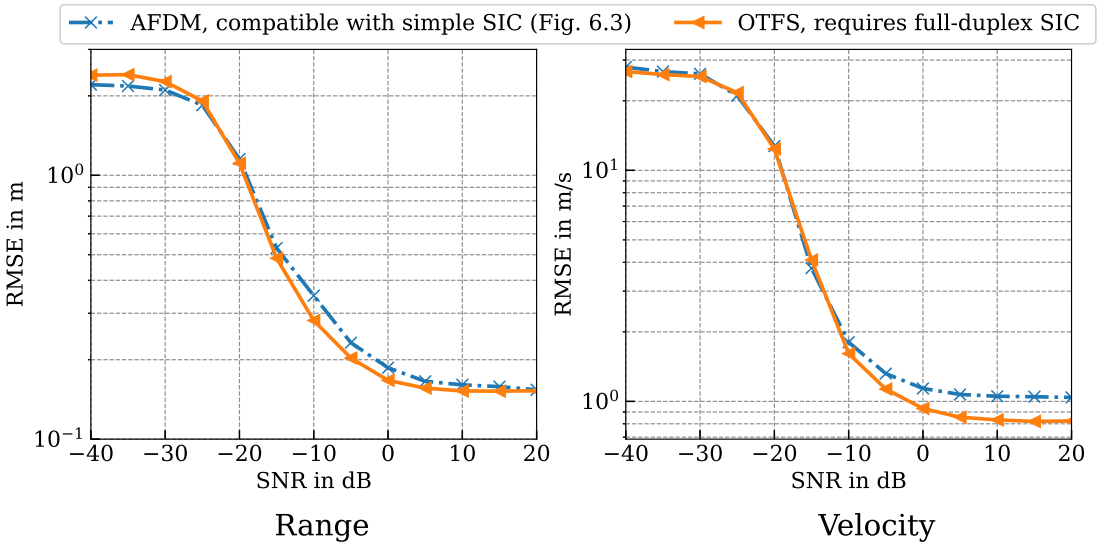

Figure 6.5: Sensing performance of AFDM-based and OTFS-based ISAC

frame. We observe that having a higher pilot dedicated for sensing improves RMSE performance, but has no effect on its saturation level, which can be thought of as the effective resolution of range and velocity estimation. This result is in accordance with the fact that one DAFT domain pilot gives the full representation of doubly selective channels and highlights the potential advantage of AFDM to greatly reduce the receiver complexity. In Fig. 6.5, we see that OTFS-based ISAC and AFDM-based ISAC have similar performance in terms of range and velocity estimation RMSE. However, achieving this performance with OTFS requires the use of complex analog SIC, while using AFDM only a simple receiver architecture is needed.

6.2 AFDM for High Frequency Bands

We now turn our attention to communication at high frequency bands without mobility. Wireless transmissions in these bands suffer from impairments such as CFO, PN and severe path loss [65, 66]. CFO and PN could destroy orthogonality among OFDM subcarriers deteriorating performance. Moreover, high-frequency wireless links may suffer

from severe PL, thus requiring waveforms with inherent coverage enhancement capabilities (not offered by OFDM or single-carrier waveforms). Other chirp-based waveforms, such as CSS [67], have been proposed for power-limited wireless links and could be relevant for many high-frequency scenarios. Indeed, CSS signals are maximally spread in time and frequency, offering a coverage gain i.e., the possibility of increasing the SNR at the receiver through spreading in time, thus doing away with inefficient SNR enhancement schemes such as symbol repetition. However, CSS achievable rates are limited due to the non-orthogonality of its multiplexed chirps.

In this chapter, In EHF bands, AFDM is shown to be maximally spread in time and frequency, thus providing a coverage gain. While maximal time-frequency spreading can be offered by other waveforms (e.g., OTFS, CSS), AFDM is distinguished by the fact that the benefits of maximal spreading are achieved while detection is (i) performed using one-tap equalization and (ii) robust to CFO and phase noise. We configure AFDM by setting c_1 to $\frac{1}{2N}$ (a value that can be obtained by plugging $k_{\max} = 0$ into (4.5)). The relevance for high-frequency scenarios of setting c_1 to different values will be addressed in future works. We next show that AFDM with this configuration can provide a coverage gain that is robust under CFO and PN and which is compatible with one-tap equalization. This remarkable property is thanks to the way AFDM with $c_1 = c_2 = \frac{1}{2N}$ becomes a waveform with both single-carrier and multi-carrier features, as shown in the following subsection. Without loss of generality, we only consider receiver side CFO and PN.

6.2.1 AFDM input-output relation under CFO and PN

In the remainder of this section, we reuse the notation $\mathbf{H}_{\text{eff}}$ originally introduced in (6.5) to make it refer to the effective DAFT domain channel matrix in presence of the considered impairments. We then introduce the new notation $\mathbf{H}_{\text{eff,free}}$ ("free" as in free from impairments) to designate the DAFT domain channel matrix when transmission undergoes no such impairments. Note that $\mathbf{H}_{\text{eff,free}}$ which is circulant for the no-mobility

scenario considered here. Let $\mathbf{P}$ be a diagonal matrix having as its main diagonal entries the multiplicative time domain complex exponentials resulting from a receiver side CFO equal (when normalized with respect to the subcarrier spacing) to ν_{CFO} and the N time domain receiver side PN samples $\{\varphi_n\}_{n=0\ldots N-1}$

$$[\mathbf{P}]_{n,n} = e^{\imath 2\pi \frac{\nu_{\text{CFO}}}{N} n} e^{\imath 2\pi \varphi_n}. \tag{6.15}$$

The effective channel matrix in presence of receiver side CFO and PN thus writes as

$$\mathbf{H}_{\text{eff}} = \mathbf{\Lambda}_{c_2}\mathbf{F}\mathbf{\Lambda}_{c_1}\mathbf{P}\mathbf{\Lambda}_{c_1}^{\text{H}}\mathbf{F}^H\mathbf{\Lambda}_{c_2}^{\text{H}}\mathbf{H}_{\text{eff,free}} = \mathbf{\Lambda}_{c_2}\mathbf{F}\mathbf{P}\mathbf{F}^H\mathbf{\Lambda}_{c_2}^{\text{H}}\mathbf{H}_{\text{eff,free}},$$

where the second equality is due to the fact that $\mathbf{\Lambda}_{c_1}$ is diagonal. Note that in the case with no impairments, $\mathbf{P} = \mathbf{I}_N$ and $\mathbf{H}_{\text{eff}} = \mathbf{H}_{\text{eff,free}}$. In the general case, the absolute value of $\mathbf{\Lambda}_{c_2}\mathbf{F}\mathbf{P}\mathbf{F}^H\mathbf{\Lambda}_{c_2}^{\text{H}}$ is circulant because $\mathbf{\Lambda}_{c_2}$ is diagonal. To get better insight into the input-output relation of AFDM as conveyed by (6.16) we first consider two scenarios in both of which the transmission undergoes only one impairment: only CFO in the first and only PN in the second.

Only-CFO scenario: It is reasonable to assume that $\nu_{\text{CFO}} < 1$ since in practice at least rough frequency synchronization is implemented. Under this assumption and $\varphi_n = 0$ for all n in (6.15), it can be shown that the absolute value of the q-th entry ($q \in \{0, \ldots, N-1\}$) of the first row of matrix $\mathbf{\Lambda}_{c_2}\mathbf{F}\mathbf{P}\mathbf{F}^H\mathbf{\Lambda}_{c_2}^{\text{H}}$ is $\left|\frac{\sin \pi(q-\nu_{\text{CFO}})}{\sin \frac{\pi}{N}(q-\nu_{\text{CFO}})}\right|$. Since this matrix is circulant in absolute value, it follows that the power of the entries of its diagonals decreases the farther they are from the main diagonal. Moreover, due to the quadratic phase of the entries of $\mathbf{\Lambda}_{c_2}$, the phase of the entries of each diagonal of the matrix $\mathbf{\Lambda}_{c_2}\mathbf{F}\mathbf{P}\mathbf{F}^H\mathbf{\Lambda}_{c_2}^{\text{H}}$ is affine in the column (or row) index with a frequency equal when normalized with respect to the subcarrier spacing to the index of the diagonal (with the main diagonal having the zero index). More precisely, the k-th entry of $\mathbf{y} = \mathbf{H}_{\text{eff}}\mathbf{x}$

($k \in \{0, \ldots, N-1\}$) is

$$y_k = \sum_{i=1}^{P} \sum_{q=0}^{N-1} h_i e^{\imath\left(\phi_{i,q} + 2\pi \frac{qk}{N}\right)} \frac{\sin \pi \left(q - \nu_{\mathrm{CFO}}\right)}{\sin \frac{\pi}{N} \left(q - \nu_{\mathrm{CFO}}\right)} x_{(k+l_i+q)_N} \,, \tag{6.16}$$

where $\phi_{i,q}$ only depends on l_i, q and N. Due to the decay profile of $\left| \frac{\sin \pi (q-\nu_{\mathrm{CFO}})}{\sin \frac{\pi}{N}(q-\nu_{\mathrm{CFO}})} \right|$ as function of q, the root mean square (RMS) of the frequency shifts q expressed in Hz i.e., $\frac{1}{NT_{\mathrm{s}}} \sqrt{\sum_{q=0}^{N-1} q^2 \frac{\sin^2 \pi (q-\nu_{\mathrm{CFO}})}{\sin^2 \frac{\pi}{N}(q-\nu_{\mathrm{CFO}})} / \sum_{q=0}^{N-1} \frac{\sin^2 \pi (q-\nu_{\mathrm{CFO}})}{\sin^2 \frac{\pi}{N}(q-\nu_{\mathrm{CFO}})}}$, where T_{s} is the sampling period, can be shown to be 1) increasing with ν_{CFO} and 2) approximately constant in N.

Only-PN scenario: Assuming the PN is modeled as a first-order auto-regressive (AR(1)) process and $\nu_{\mathrm{CFO}} = 0$ in (6.15), it can be shown as in [68, Appendix A] that the entries of the diagonals of the circulant matrix $\mathbf{F}\mathbf{P}\mathbf{F}^H$ (and hence those of the matrix $\mathbf{\Lambda}_{c_2}\mathbf{F}\mathbf{P}\mathbf{F}^H\mathbf{\Lambda}_{c_2}^{\mathrm{H}}$ which is circulant in absolute value) have mean powers averaged over the PN process realizations that decay the farther the diagonal is from the main diagonal [68]. As in the CFO scenario, the phase evolution of the entries of each diagonal of $\mathbf{\Lambda}_{c_2}\mathbf{F}\mathbf{P}\mathbf{F}^H\mathbf{\Lambda}_{c_2}^{\mathrm{H}}$ has a frequency equal when normalized with respect to the subcarrier spacing to the index of the diagonal. Also, the RMS of these frequency shifts in Hz can be shown to be increasing with the RMS of the AR(1)-PN process and approximately independent of N.

Both-CFO-and-PN scenario: Combining the two scenarios and referring to (6.16), the effect of both CFO and phase noise on the DAFT domain channel response can be verified to be cumulative and amounting to mapping each diagonal in $\mathbf{H}_{\mathrm{eff,free}}$ representing a channel path to a "spectrum" of frequency shifted and attenuated diagonals in $\mathbf{H}_{\mathrm{eff}}$, possibly partially overlapping with the spectra corresponding to other channel paths, and whose effective width increases with the CFO value and the RMS of the PN process while being approximately constant in N when normalized by it.

Result 1. *The input-output relation of AFDM in presence of CFO and AR(1)-PN is that of an equivalent* time domain *channel subject to a Doppler spread whose RMS is*

increasing with the CFO value and with the RMS of the PN process and approximately constant in N when expressed in Hz.

6.2.2 AFDM robust spreading gain

By *robustness* in presence of impairments we mean relative advantage to other waveforms in terms of relevant performance metrics e.g., BER, when channel estimation and data detection are done without knowing the values of these impairments e.g., the CFO in Hz or the time domain phase noise samples in radians. In the case of OFDM, impairment-agnostic detection amounts to ignoring ICI and using one-tap equalization based on (an estimate of) the main diagonal of the frequency domain channel matrix[2]. In the case of AFDM with $c_1 = c_2 = \frac{1}{2N}$, an impairment-agnostic receiver would do channel estimation and equalization assuming the DAFT domain channel matrix $\mathbf{H}_{\text{eff}}$ to be circulant (while it is only circulant in the absence of the impairments as can be seen from (6.16)). One possible detection method when $\mathbf{H}_{\text{eff}}$ is assumed circulant is one-tap equalization applied using an estimate of the main diagonal of the DFT factorization of this matrix. Consider a N-point AFDM frame $\mathbf{x} = \mathbf{A}_{\text{u}}\mathbf{x}_{\text{u}}$ composed of $N_{\text{u}} > 1$ ('u' for "used") data symbols represented by vector $\mathbf{x}_{\text{u}}$ and occupying contiguous positions within $\mathbf{x}$ with $N_{\text{u}} \leq N$. Here, $\mathbf{A}_{\text{u}}$ is the $N \times N_{\text{u}}$ matrix that maps the non-zero data symbols to their positions. Let

$$\mathbf{y} = \mathbf{H}_{\text{eff}}\mathbf{A}_{\text{u}}\mathbf{x}_{\text{u}} + \mathbf{w} \tag{6.17}$$

be the N-long vector of received DAFT domain samples (after AFDM demodulation). Note that $\mathbf{H}_{\text{eff}}\mathbf{A}_{\text{u}}$ is not a square matrix and hence not circulant even in the absence of impairments. The effective channel matrix associated with $\mathbf{x}_{\text{u}}$ can though be made

[2]The estimate of the main diagonal of the channel matrix of an OFDM symbol in presence of these impairments can be obtained either based on pilots embedded in the same symbol or based on pilots embedded in previous symbols. Note that common phase error (CPE) estimation and compensation is needed in the latter case but not in the former.

square (and circulant in the absence of impairments) by applying overlap-add (OLA) [69] to the entries of $\mathbf{y}$ corresponding to the $N - N_{\mathrm{u}}$ zero samples of $\mathbf{x}$. Let $\mathbf{y}_{\mathrm{u}} \triangleq \mathbf{A}_{\mathrm{OLA}}\mathbf{y}$ be the resulting vector with $\mathbf{A}_{\mathrm{OLA}}$ being the $N_{\mathrm{u}} \times N$ matrix representing the OLA operation. Then

$$\mathbf{y}_{\mathrm{u}} = \mathbf{H}_{\mathrm{eff,u}}\mathbf{x}_{\mathrm{u}} + \mathbf{A}_{\mathrm{OLA}}\mathbf{w}, \tag{6.18}$$

where

$$\mathbf{H}_{\mathrm{eff,u}} \triangleq \mathbf{A}_{\mathrm{OLA}}\mathbf{H}_{\mathrm{eff}}\mathbf{A}_{\mathrm{u}}. \tag{6.19}$$

It follows that the one-tap LMMSE estimate of $\mathbf{x}_{\mathrm{u}}$ is

$$\hat{\mathbf{x}}_{\mathrm{u}} = \mathrm{IDFT}\left\{\left(\mathrm{diag}\left(\tilde{\mathbf{H}}_{\mathrm{eff,u}}\right)^{\mathrm{H}}\mathrm{diag}\left(\tilde{\mathbf{H}}_{\mathrm{eff,u}}\right) + \mathbf{\Sigma}_{\mathbf{w}}\right)^{-1}\tilde{\mathbf{y}}_{\mathrm{u}}\right\} \tag{6.20}$$

where $\tilde{\mathbf{y}}_{\mathrm{u}} \triangleq \mathrm{DFT}\{\mathbf{y}_{\mathrm{u}}\}$, $\tilde{\mathbf{H}}_{\mathrm{eff,u}} \triangleq \mathbf{F}_{N_{\mathrm{u}}}\mathbf{H}_{\mathrm{eff,u}}\mathbf{F}_{N_{\mathrm{u}}}^{\mathrm{H}}$ and $\mathbf{\Sigma}_{\mathbf{w}}$ is the $N_{\mathrm{u}} \times N_{\mathrm{u}}$ (diagonal) covariance matrix of the noise samples vector $\mathbf{A}_{\mathrm{OLA}}\mathbf{w}$. Of course, when the transmission is subject to CFO or PN, $\mathbf{H}_{\mathrm{eff}}$ as given by (6.16) and $\mathbf{H}_{\mathrm{eff,u}}$ as given by (6.19) are not circulant. As a result, $\tilde{\mathbf{H}}_{\mathrm{eff,u}}$ is not diagonal. The main diagonal of $\tilde{\mathbf{H}}_{\mathrm{eff,u}}$ can still be estimated based on one embedded pilot symbol as in Section 5.2 but the performance of the one-tap equalizer in (6.20) based on this estimate suffers from ICI due to the off-diagonal entries of $\tilde{\mathbf{H}}_{\mathrm{eff,u}}$. However, due to the property summarized by Result 1, this degradation will be of the order of what would be undergone by an equivalent N_{u}-point (and not N-point) OFDM transmission with N_{u} active subcarriers taking place on the same wireless channel in presence of the same impairments. It will then have the higher robustness of the larger subcarrier spacing $\frac{1}{N_{\mathrm{u}}} \geq \frac{1}{N}$.

Now, refer to (3.1) and note that a constraint on the time domain transmit power such as $\mathbb{E}\left[|s_n|^2\right] \leq P_{\mathrm{tx}}$ translates into $\mathbb{E}\left[|x_m|^2\right] \leq \frac{N}{N_{\mathrm{u}}}P_{\mathrm{tx}}$. This means that increasing N at a constant N_{u} and P_{tx} provides a $\frac{N}{N_{\mathrm{u}}}$-times increase in the effective SNR associated with detecting $\hat{\mathbf{x}}_{\mathrm{u}}$ in (6.20). Combining this fact with the higher-robustness property described above shows that for small-enough values of N_{u} compared to N, this SNR

increase translates into an increase in the signal-to-interference-plus-noise ratio (SINR).

Result 2. *The one-tap equalization in* (6.20) *for a N-point AFDM signal with $N_{\mathrm{u}} \leq N$ active data symbols and a transmit power equal to P_{tx} has under CFO and AR(1)-PN the SINR performance of an equivalent N_{u}-point OFDM with a $\frac{N}{N_{\mathrm{u}}} P_{\mathrm{tx}}$ transmit power under a Doppler spread with a RMS proportional to the CFO and the PN RMS values.*

One application of this result is coverage enhancement in power-limited scenarios that are also subject to CFO and PN e.g., mmWave, sub-THz and THz communications under severe pathloss [65, 66] and/or imperfect antenna beam alignment between the wireless transmitter and receiver.

Remark 1. *In multiple-access settings, the robust spreading gain offered by AFDM does not come at the cost of reduced system spectral efficiency. Indeed, while each multiplexed spread AFDM signal occupies the frequency bandwidth and time duration of the whole multicarrier symbol, different spread AFDM signals occupy orthogonal resources in the DAFT domain. This is in contrast to coverage gain enhancement using symbol repetition for single-carrier waveforms with time-division multiple access (TDMA).*

6.2.3 Simulation Results

We compare the BER performance of AFDM and OFDM, both with $N = 256$ and using QPSK and one-tap equalization receivers, in a high-frequency scenario characterized with a low transmit power, large pathloss, severe phase noise and no CFO. Fig. 6.6 was obtained assuming a line-of-sight (LoS) channel with $P = 1$, a zero Doppler shift $f_1 = 0$, a delay l_1 that is derived from the distance d separating the transmitter from the receiver. The variance of the complex gain h_1 was computed using the THz pathloss model from [66] assuming a carrier frequency $f_{\mathrm{c}} = 0.35$ THz and 27-dBi antenna gains. The receiver side phase noise was generated using a AR(1) random process having a power spectral density with a 3-dB bandwidth $B^{\mathrm{PN}}_{3-\mathrm{dB}}$ of approximately 60 kHz. This value was obtained starting from a typical value of $B^{\mathrm{PN}}_{3-\mathrm{dB}}$ for an oscillator operating at

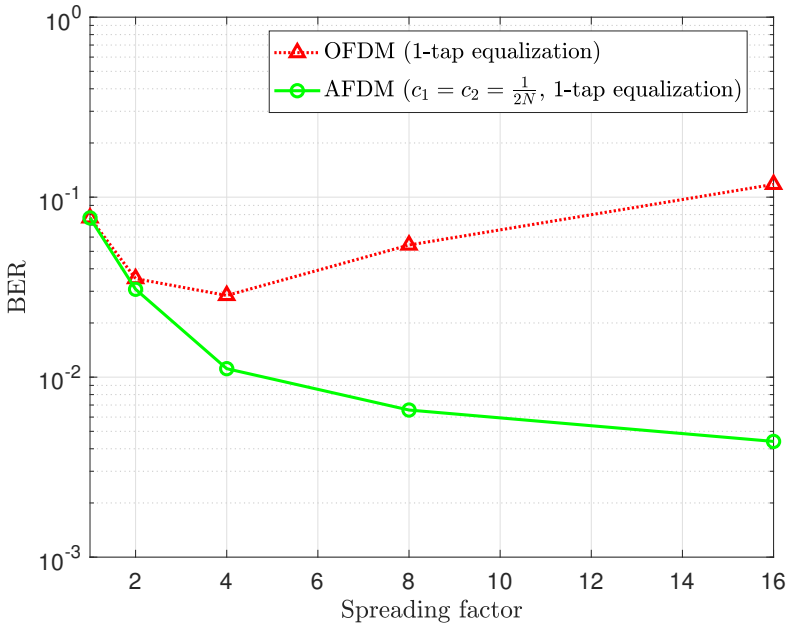

Figure 6.6: BER performance of OFDM and AFDM with using QPSK with $N_{\mathrm{u}} = 64$, $N =$ spreading factor$\times N_{\mathrm{u}}$ assuming a LoS THz channel with $d = 1$ m, $f_{\mathrm{c}} = 0.35$ THz, BW $= 0.5$ GHz, $B^{\mathrm{PN}}_{3-\mathrm{dB}} = 60$ kHz, $P_{\mathrm{tx}} = -3$ dBm and $G_{\mathrm{Tx}} = G_{\mathrm{Rx}} = 27$ dBi

2.4 GHz [70] and then scaled to account for the higher carrier frequency using the scaling laws from [70, 71]. The number of data symbols per OFDM and AFDM frame is $N_{\mathrm{u}} = 64$ and the transmit power is equal to $P_{\mathrm{tx}} = -3$ dBm for both schemes. When $N = N_u$, the SNR and the SINR associated with one-tap equalization are both low for both OFDM and AFDM resulting in a relatively large BER. Increasing N while keeping N_{u} and P_{tx} fixed increases the received SNR for both schemes. For AFDM, this translates into an increase in SINR and a decrease in BER thanks to its robust spreading/coverage gain property. As for OFDM, increasing N inversely reduces the subcarrier spacing resulting in degraded BER performance.

6.3 Conlcusion

In this chapter, we delved into a deep exploration of AFDM's potential applications, moving beyond its conventional uses and into pioneering areas of communication technology.

We first stepped into the realm of ISAC, where the merging of wireless communications and radar sensing has emerged. AFDM's inherent capabilities seamlessly align with ISAC's needs, highlighting its suitability in harmonizing communication and radar sensing. Our proposed ISAC scheme capitalized on AFDM's unique traits, such as its full Delay-Doppler representation, facilitating an integrated approach using either a whole frame or just a single pilot symbol. We showed this approach not only consolidates radar and communication systems but also leads to a simplified SIC method avoiding the need for expensive full-duplex techniques and hardware.

Transitioning from ISAC, we navigated the challenges and prospects of EHF band communications. Wireless transmissions in EHF are marred by impairments, from CFO and PN to severe path loss. AFDM, when configured optimally, stands out as a robust solution in this domain, delivering maximal time-frequency spreading benefits and ensuring resilience against CFO and phase noise. Through its unique blend of single-carrier and multi-carrier features, AFDM showcases its adaptability and efficiency in addressing high-frequency communication challenges.

In summary, this chapter has further solidified AFDM's versatility as a modulation technique, emphasizing its potential in ISAC and EHF band communications.

Chapter 7

Conclusion

In this thesis, a groundbreaking solution known as Affine Frequency Division Multiplexing (AFDM) is introduced. This innovative chirp-based multicarrier waveform hinges on the Discrete Affine Fourier Transform (DAFT). The initial chapters of the thesis thoroughly outlined the fundamental aspects and principles behind wireless channels, the AFT, and its discrete version, laying a solid groundwork for understanding the AFDM technique. The thesis delved into the comprehensive exploration of the AFDM, its modulation, and demodulation processes, channel model, and matrix representation. This extensive discussion allowed a deeper understanding of the input-output relationship and the significant role of parameter settings in AFDM, especially the selection of c_1.

Furthermore, the thesis provided crucial insights into the capabilities of AFDM in relation to the full diversity order of LTV channels. Through meticulous parameter adjustments and an analytical approach, it was demonstrated that AFDM can efficiently achieve the full diversity of the LTV channels, with simulation results underlining its practical efficiency.The discussion extended to the realms of detection and channel estimation, where innovative low-complexity detection algorithms and an embedded pilot-aided channel estimation scheme were proposed. These proposals showcased the potential to optimize the AFDM-based communication systems by integrating channel

estimation with data detection, ensuring precise channel knowledge and improved overall system performance.

In the exploration of potential applications, the thesis presented the applicability of AFDM in the emerging field of ISAC, revealing how its unique traits could harmonize communication and radar sensing. A novel ISAC scheme was proposed, offering an integrated and simplified approach in ISAC scenarios. The thesis also highlighted the robustness of AFDM in EHF band communications, where it stands out as a resilient solution against various impairments, demonstrating its adaptability and efficiency in high-frequency communication challenges.

In conclusion, this thesis has proposed AFDM and significantly enhanced the understanding and application of the AFDM scheme in wireless communications. By unveiling its potential in various scenarios and proposing innovative solutions to existing challenges, the research serves as a valuable reference for future work and developments in this domain. The rigorous exploration, analyses, and the proposed schemes and applications within this thesis affirm the versatility and efficacy of the AFDM as a promising modulation technique in modern and emerging communication systems.

Bibliography

[1] A. Fotouhi, H. Qiang, M. Ding, M. Hassan, L. G. Giordano, A. Garcia-Rodriguez, and J. Yuan, "Survey on uav cellular communications: Practical aspects, standardization advancements, regulation, and security challenges," *IEEE Communications surveys & tutorials*, vol. 21, no. 4, pp. 3417–3442, 2019.

[2] G. Meyer and S. Beiker, *Road vehicle automation*. Springer, 2019, vol. 201955.

[3] T. Hwang, C. Yang, G. Wu, S. Li, and G. Y. Li, "Ofdm and its wireless applications: A survey," *IEEE transactions on Vehicular Technology*, vol. 58, no. 4, pp. 1673–1694, 2008.

[4] T. Wang, J. G. Proakis, E. Masry, and J. R. Zeidler, "Performance degradation of OFDM systems due to Doppler spreading," *IEEE Trans. on Wirel. Commun.*, vol. 5, no. 6, pp. 1422–1432, 2006.

[5] "The industrial reorganization act: The communications industry," in *Proceedings of the Institution of Electrical Engineers*, vol. 73, no. 3, 1973, pp. 635–676.

[6] G. Gott and J. Newsome, "HF data transmission using chirp signals," in *Proceedings of the Institution of Electrical Engineers*, vol. 118, no. 9. IET, 1971, pp. 1162–1166.

[7] A. Kadri, R. K. Rao, and J. Jiang, "Low-power chirp spread spectrum signals for wireless communication within nuclear power plants," *Nuclear Technology*, vol. 166, no. 2, pp. 156–169, 2009.

[8] C. He, M. Ran, Q. Meng, and J. Huang, "Underwater acoustic communications using m-ary chirp-DPSK modulation," in *IEEE 10th international conference on signal processing proceedings*. IEEE, 2010.

[9] M. Palmese, G. Bertolotto, A. Pescetto, and A. Trucco, "Experimental validation of a chirp-based underwater acoustic communication method," in *Proceedings of Meetings on Acoustics*, vol. 4, no. 1. Acoustical Society of America, 2008.

[10] "IEEE standard for information technology - local and metropolitan area networks - specific requirements - part 15.4: Wireless medium access control (MAC) and physical layer (PHY) specifications for low-rate wireless personal area networks (WPANs): Amendment 1: Add alternate PHYs," *IEEE Std 802.15.4a-2007 (Amendment to IEEE Std 802.15.4-2006)*, pp. 1–210, 2007.

[11] M. Martone, "A multicarrier system based on the fractional Fourier transform for time-frequency-selective channels," *IEEE Trans. on Commun.*, vol. 49, no. 6, pp. 1011–1020, Jun. 2001.

[12] T. Erseghe, N. Laurenti, and V. Cellini, "A multicarrier architecture based upon the affine Fourier transform," *IEEE Trans. on Commun.*, vol. 53, no. 5, pp. 853–862, May 2005.

[13] D. Stojanović, I. Djurović, and B. R. Vojcic, "Multicarrier communications based on the affine Fourier transform in doubly-dispersive channels," *EURASIP Journal on Wireless Communications and Networking*, vol. 2010, pp. 1–10, 2010.

[14] X. Ouyang and J. Zhao, "Orthogonal chirp division multiplexing," *IEEE Trans. on Commun.*, vol. 64, no. 9, pp. 3946–3957, Sept. 2016.

[15] M. S. Omar and X. Ma, "Performance analysis of OCDM for wireless communications," *IEEE Trans. on Wirel. Commun.*, vol. 20, no. 7, pp. 4032–4043, 2021.

[16] H. G. Myung, J. Lim, and D. J. Goodman, "Single carrier fdma for uplink wireless transmission," *IEEE Vehicular Technology Magazine*, vol. 1, no. 3, pp. 30–38, 2006.

[17] G. Fettweis, M. Krondorf, and S. Bittner, "GFDM-generalized frequency division multiplexing," in *VTC Spring 2009-IEEE 69th Vehicular Technology Conference*. IEEE, 2009, pp. 1–4.

[18] N. Michailow, M. Matthé, I. S. Gaspar, A. N. Caldevilla, L. L. Mendes, A. Festag, and G. Fettweis, "Generalized frequency division multiplexing for 5th generation cellular networks," *IEEE Trans. on Commun.*, vol. 62, no. 9, pp. 3045–3061, 2014.

[19] R. Hadani, S. Rakib, M. Tsatsanis, A. Monk, A. J. Goldsmith, A. F. Molisch, and R. Calderbank, "Orthogonal time frequency space modulation," in *2017 IEEE Wireless Communications and Networking Conference (WCNC)*, 2017.

[20] R. Hadani and A. Monk, "OTFS: A new generation of modulation addressing the challenges of 5G," *arXiv preprint arXiv:1802.02623*, 2018.

[21] W. Anwar, A. Krause, A. Kumar, N. Franchi, and G. P. Fettweis, "Performance analysis of various waveforms and coding schemes in V2X communication scenarios," in *2020 IEEE Wireless Commun. & Netw. Conf. (WCNC)*. IEEE, 2020, pp. 1–8.

[22] P. Raviteja, Y. Hong, E. Viterbo, and E. Biglieri, "Effective diversity of OTFS modulation," *IEEE wireless communications letters*, vol. 9, no. 2, pp. 249–253, 2019.

[23] G. Surabhi, R. M. Augustine, and A. Chockalingam, "On the diversity of uncoded OTFS modulation in doubly-dispersive channels," *IEEE Trans. on Wireless Communications*, vol. 18, no. 6, pp. 3049–3063, 2019.

[24] P. Raviteja, K. T. Phan, and Y. Hong, "Embedded pilot-aided channel estimation for OTFS in delay–Doppler channels," *IEEE Trans. on Vehicular Technology*, vol. 68, no. 5, pp. 4906–4917, 2019.

[25] A. Bemani, N. Ksairi, and M. Kountouris, "AFDM: A full diversity next generation waveform for high mobility communications," in *2021 IEEE International Conference on Communications Workshops (ICC Workshops)*, 2021, pp. 1–6.

[26] A. Bemani, G. Cuozzo, N. Ksairi, and M. Kountouris, "Affine frequency division multiplexing for next-generation wireless networks," in *2021 17th International Symposium on Wireless Communication Systems (ISWCS)*. IEEE, 2021, pp. 1–6.

[27] A. Bemani, N. Ksairi, and M. Kountouris, "Low complexity equalization for afdm in doubly dispersive channels," in *2022 Proc. IEEE International Conference on Acoustics, Speech and Signal Processing (ICASSP)*. IEEE, 2022.

[28] ——, "Affine frequency division multiplexing for next generation wireless communications," *IEEE Transactions on Wireless Communications*, 2023.

[29] ——, "Integrated sensing and communications with affine frequency division multiplexing," *IEEE Wireless Communications Letters*, pp. 1–1, 2024.

[30] D. Tse and P. Viswanath, *Fundamentals of wireless communication*. Cambridge university press, 2005.

[31] F. Hlawatsch and G. Matz, *Wireless communications over rapidly time-varying channels*. Academic press, 2011.

[32] C. Phillips, D. Sicker, and D. Grunwald, "A survey of wireless path loss prediction and coverage mapping methods," *IEEE Communications Surveys & Tutorials*, vol. 15, no. 1, pp. 255–270, 2012.

[33] S. A. Collins, "Lens-system diffraction integral written in terms of matrix optics," *JOSA*, vol. 60, no. 9, pp. 1168–1177, 1970.

[34] M. Moshinsky and C. Quesne, "Linear canonical transformations and their unitary

representations," *Journal of Mathematical Physics*, vol. 12, no. 8, pp. 1772–1780, 1971.

[35] S. Abe and J. Sheridan, "Optical operations on wave functions as the abelian subgroups of the special affine fourier transformation," *Optics letters*, vol. 19, no. 22, pp. 1801–1803, 1994.

[36] L. M. Bernardo, "ABCD matrix formalism of fractional fourier optics," *Optical Engineering*, vol. 35, no. 3, pp. 732–740, 1996.

[37] D. James and G. Agarwal, "The generalized fresnel transform and its applications to optics," *Optics Communications*, vol. 126, pp. 207–212, 1996.

[38] M. J. Bastiaans, "The wigner distribution applied to optical signals and systems," *Optics Communications*, vol. 25, no. 1, pp. 26–30, 1978.

[39] ——, "Wigner distribution function and its application to first-order optics," *Journal of the Optical Society of America*, vol. 69, no. 12, pp. 1710–1716, 1979.

[40] ——, "Propagation laws for the second-order moments of the wigner distribution function in first-order optical systems," *Optik*, vol. 82, no. 4, pp. 173–181, 1989.

[41] ——, "Second-order moments of the wigner distribution function in first-order optical systems," *Optik*, vol. 88, no. 4, pp. 163–168, 1991.

[42] A. E. Siegman, *Lasers*, 1st ed. Mill Valley, CA: University Science Books, 1986, sec. 20.7, pp. 811-814.

[43] J. Hua, L. Liu, and G. Li, "Extended fractional fourier transforms," *Journal of the Optical Society of America A*, vol. 14, no. 12, pp. 3316–3322, 1997.

[44] H. M. Ozaktas and M. A. Kutay, "The fractional fourier transform," in *2001 European Control Conference (ECC)*, 2001, pp. 1477–1483.

[45] A. W. Lohmann, D. Mendlovic, and Z. Zalevsky, "Iv: fractional transformations in optics," in *Progress in optics*. Elsevier, 1998, vol. 38, pp. 263–342.

[46] H. M. Ozaktas and D. Mendlovic, "Fractional fourier optics," *JOSA A*, vol. 12, no. 4, pp. 743–751, 1995.

[47] S.-C. Pei and J.-J. Ding, "Relations between the fractional operations and the wigner distribution, ambiguity function," *IEEE Transactions on Signal Processing*, vol. 49, no. 8, pp. 1638–1655, 2001.

[48] E. P. Wigner, "On the quantum correction for thermodynamic equilibrium," *Physical Review*, vol. 40, no. 5, pp. 749–759, 1932.

[49] F. Hlawatsch, G. F. Boudreaux-Bartels *et al.*, "Linear and quadratic time-frequency signal representations," *IEEE signal processing magazine*, vol. 9, no. 2, pp. 21–67, 1992.

[50] S.-C. Pei and J.-J. Ding, "Closed-form discrete fractional and affine Fourier transforms," *IEEE Trans. on Sig. Proc.*, vol. 48, no. 5, pp. 1338–1353, May 2000.

[51] Z. Wei, S. Li, W. Yuan, R. Schober, and G. Caire, "Orthogonal time frequency space modulation – part i: Fundamentals and challenges ahead," 2022. [Online]. Available: https://arxiv.org/abs/2209.05011

[52] ——, "Orthogonal time frequency space modulation – part i: Fundamentals and challenges ahead," *IEEE Communications Letters*, pp. 1–1, 2022.

[53] C. F. Van Loan and G. Golub, "Matrix computations (johns hopkins studies in mathematical sciences)," 1996.

[54] L. Rugini, P. Banelli, and G. Leus, "Simple equalization of time-varying channels for OFDM," *IEEE communications letters*, vol. 9, no. 7, pp. 619–621, 2005.

[55] G. H. Gloub and C. F. Van Loan, "Matrix computations," *Johns Hopkins Universtiy Press, 3rd edtion*, 1996.

[56] Å. Björck, *Numerical methods for least squares problems.* SIAM, 1996.

[57] Y. Saad, *Iterative methods for sparse linear systems.* SIAM, 2003.

[58] L. Gaudio, M. Kobayashi, G. Caire, and G. Colavolpe, "On the effectiveness of otfs for joint radar parameter estimation and communication," *IEEE Trans. Wirel. Commun.*, vol. 19, no. 9, pp. 5951–5965, 2020.

[59] F. Liu, C. Masouros, A. P. Petropulu, H. Griffiths, and L. Hanzo, "Joint radar and communication design: Applications, state-of-the-art, and the road ahead," *IEEE Trans. on Commun.*, vol. 68, no. 6, 2020.

[60] F. Liu, C. Masouros, A. Li, H. Sun, and L. Hanzo, "Mu-mimo communications with mimo radar: From co-existence to joint transmission," *IEEE Transactions on Wireless Communications*, vol. 17, no. 4, pp. 2755–2770, 2018.

[61] A. R. Chiriyath, B. Paul, and D. W. Bliss, "Radar-communications convergence: Coexistence, cooperation, and co-design," *IEEE Transactions on Cognitive Communications and Networking*, vol. 3, no. 1, 2017.

[62] L. G. d. Oliveira, M. B. Alabd, B. Nuss, and T. Zwick, "An ocdm radar-communication system," in *2020 14th European Conference on Antennas and Propagation (EuCAP)*, 2020, pp. 1–5.

[63] Y. Ni, Z. Wang, P. Yuan, and Q. Huang, "An AFDM-based integrated sensing and communications," in *2022 International Symposium on Wireless Communication Systems (ISWCS)*, 2022, pp. 1–6.

[64] Y. Geng, "A novel waveform design for ofdm-based joint sensing and communication system," *arXiv preprint arXiv:2301.03347*, 2023.

[65] H. Huang, W. G. J. Wang, and J. He, "Phase noise and frequency offset compensation in high frequency MIMO-OFDM system," in *2015 IEEE International Conference on Communications (ICC)*, 2015, pp. 1280–1285.

[66] E. N. Papasotiriou, J. Kokkoniemi, A.-A. A. Boulogeorgos, J. Lehtomäki, A. Alexiou, and M. Juntti, "A new look to 275 to 400 GHz band: Channel model and performance evaluation," in *2018 IEEE 29th Annual International Symposium on Personal, Indoor and Mobile Radio Communications (PIMRC)*, 2018, pp. 1–5.

[67] B. Reynders and S. Pollin, "Chirp spread spectrum as a modulation technique for long range communication," in *2016 Symposium on Communications and Vehicular Technologies (SCVT)*, 2016, pp. 1–5.

[68] G. Sridharan and T. J. Lim, "Performance analysis of sc-fdma in the presence of receiver phase noise," *IEEE Transactions on Communications*, vol. 60, no. 12, pp. 3876–3885, 2012.

[69] S. Salivahanan and A. Vallavaraj, *Digital Signal Processing*. McGraw-Hill, 2001.

[70] C. M. Yuen and K. F. Tsang, "Phase noise measurement of free-running vco using spectrum analyzer," in *Proceedings. 2004 IEEE Radio and Wireless Conference (IEEE Cat. No.04TH8746)*, 2004, pp. 443–446.

[71] D. Petrovic, W. Rave, and G. Fettweis, "Effects of phase noise on ofdm systems with and without pll: Characterization and compensation," *IEEE Transactions on Communications*, vol. 55, no. 8, pp. 1607–1616, 2007.